Functional Properties and Electrochemical Performance of New Positrode Materials for Proton Ceramic Electrochemical Cells

Håkon Andersen

Thesis for the degree of
Master of Science

Department of Chemistry
Faculty of Mathematics and Natural Science UNIVERSITY OF OSLO

June 2020

2019

Functional Properties and Electrochemical Performance of New Positrode Materials for Proton Ceramic Electrochemical Cells

Håkon Andersen

http://www.duo.uio.no/

Trykk: Reprosentralen, Universitetet i Oslo

“Water will be the coal of the future.”

- Jules Verne

Preface

This thesis represents part of the required work for the degree of Master of Science (M.Sc.) at the Department of Chemistry, Faculty of Mathematics and Natural Sciences, University of Oslo. The work was carried out at the group of Electrochemistry under supervision of Professor Truls E. Norby and Dr Ragnar Strandbakke during the period from August 2018 to June 2020.

First of all, I would like to thank my main and co-supervisor Professor Truls E. Norby and Dr Ragnar Strandbakke for their guidance, motivation and encouragement through the entire process. I would also like to thank Kevin, Stian, Mikael and Tord for sharing an office with me through this time. A big thank you to my fellow students and to the whole research group for contributing to a great working environment. I would also like to thank everyone in the GoPHy MiCO project for great discussions and insight that has made this work possible.

Lastly, I would like to thank my friends and family for their unending support.

Oslo, June 2020

Håkon Andersen

Summary

Proton Ceramic Electrochemical Cells (PCECs) exhibit high efficiency at lower temperatures due to the low activation energy of proton transport. PCECs have also obtained a great interest for its fuel utilisation, which result in a higher operating cell voltage and efficiency. However, the development of efficient commercial PCECs has been held back by the lack of an efficient electrode at the oxygen steam side, also known as positrode. $BaGd_{0.8}La_{0.2}Co_2O_{6-\delta}$ (BGLC82) has shown to be a state of the art positrode, with Mixed Proton and Electronic Conductivity (MPEC).

By using BGLC82 as a backbone in developing new and efficient electrode materials, the primary object of this thesis is to study the functional properties of selected doped BGLC82 materials, with their focus as positrode materials for PCECs. BGLC82 was 10 % doped with the chosen materials zinc, titanium and zirconia ($BaGd_{0.8}La_{0.2}Co_{1.8}X_{0.2}O6_{-\delta}$ X=Zn, Ti, Zr).

The BGLC82 compositions were synthesised by solid-state reaction (SSR). BGLC82 Ti and Zn showed to obtain single phases, whereas BGLC82: Zr exhibit a secondary phase of $BaZrO_3$. To try to obtain a single phase of BGLC82: Zr sol-gel (SG) synthesis was used. BGLC82: Zr still exhibited the same secondary phase obtained for SSR, but with a lower amount. This implies that the solubility of Zr in BGLC82 was exceeded.

BGLC82 Ti and Zn were tested for proton uptake by Thermogravimetric Analysis (TGA) at 300 – 500 °C. The measurements showed that BGLC82: Ti exhibits a higher proton uptake than BGLC82, whereas BGLC82: Zn obtain lower proton uptake than BGLC82. This implies that the donor dopant stabilises the protonic defects in the BGLC82 structure, due to the basisety of the cation.

For the experimental setup, small pellets of the BGLC82 composites were placed on top of a $BaZr_{0.7}Ce_{0.2}Y_{0.1}O_{3-\delta}$ (BZCY72) at the same time and held in place by a spring load. To obtain the best contact between the electrodes and the electrolyte, the surfaces in contact were polished. Platinum was used as counter and reference electrode, placed on the opposite side of the BGLC82 composite electrodes.

The activation energy for proton transport in the electrolyte exhibited the same value for all the electrodes in OCV and bias measurements. This implies that the experimental setup works and the electrodes do not interfere with each other during measurements.

From the OCV measurements, the different BGLC82 compositions were compared to literature values for BGLC82. BGLC82: Zr made by SG exhibited close to the same performances as reported for BGLC82. The BGLC82: Ti and Zn showed polarization resistances higher than BGL82. The two polarisation resistances ($R_{p,2}$ and $R_{p,3}$) exhibited similar pH_2O and pO_2 dependencies for all the electrodes. The results indicate that the rate-limiting steps are red-ox of absorbed oxygen for $R_{p,2}$ and the exchange of oxygen on the surface for $R_{p,3}$.

From the bias measurements, BGLC82: Zn exhibited the lowest total polarization resistance of the electrodes at negative bias. For the positive bias measurements, BGLC82: Ti showed the lowest total polarization resistance of the electrodes. These measurements indicate that BGLC82: Zn is a more suited positrode for Proton Ceramic Fuel Cells (PCFC), and BGLC82: Ti is a better positrode for Proton Ceramic Electrolysers (PCE), cathode and anode, respectively. The electrodes obtained significantly different total polarization resistances from the negative and positive bias. This indicates there is a change in the Rate-Determining Step (RDS) for the electrodes at negative and positive bias.

List of Abbreviations

BGCF	$BaGdCo_{1.8}Fe_{0.2}O_{6-\delta}$
BGLC82	$BaGd_{0.8}La_{0.2}Co_2O_{6-\delta}$
BGLC82: Ti	$BaGd_{0.8}La_{0.2}Co_{1.8}Ti_{0.2}O_{6-\delta}$
BGLC82: Zn	$BaGd_{0.8}La_{0.2}Co_{1.8}Zn_{0.2}O_{6-\delta}$
BGLC82: Zr SG	$BaGd_{0.8}La_{0.2}Co_{1.8}Zr_{0.2}O_{6-\delta}$ by sol-gel metode
BGLC82: Zr SSR	$BaGd_{0.8}La_{0.2}Co_{1.8}Zr_{0.2}O_{6-\delta}$ by solid-state reaction
BPC	$BaPrCo_2O_{6-\delta}$
BPCF	$BaPrCo_{1.4}Fe_{0.6}O_{6-\delta}$
BZCY72	$BaZr_{0.7}Ce_{0.2}Y_{0.1}O_{3-\delta}$
BZY	Yttrium-doped $BaZrO^3$
CE	Counter electrode
CEC	Ceramic Electrochemical cell
ct	Charge transfer
EDS	Energy Dispersive X-Ray Spectroscopy
EIS	Electrochemical Impedance Spectrocopy
FEG	Field Emission Gun
HER	Hydogen Evolution Reaction
K-V	Kröger-Vink
MOEC	Mixed Oxygen ion and Electronic Conductor

MPEC	Mixed Proton and Electronic Conductor
mt	Mass transfer
OER	Oxygen Evolution Reaction
PCE	Proton Ceramic Electrolyt
PCEC	Proton Ceramic Electrochemical Cell
PEME	Proton Exchange Membrane Electrolyser
PEMFC	Proton Exchange Membrane Fuel cell
RD	Relative Density
RDS	Rate Deterimg Step
SDC	Samarium-doped ceria
SEM	Scanning Electron Microscopy
SOE	Solid Oxide Electrolyser
SOEC	Solid Oxide Electrochemical Cell
SG	Sol-Gel
SSR	Solid State Reactin
TGA	Thermogravimetric Analysis
TPB	Triple Phase Boundary
WE	Workin Electrode
XRD	X-ray Diffraction

Table of Contents

1 Introduction

1.1 Background and Motivation

With a growing population worldwide, energy demands are rapidly increasing. Energy from fossil fuels, which at present is the most common source of energy, renders emission of greenhouse gasses. As climate changes are affecting the worldwide population, efficient, affordable, and clean energy sources are vital to minimise these changes for generations to come.

New and efficient ways to produce clean energy utilizing solar cells and wind turbines are becoming more common than ever before, with growing demands from the customers. However, as the climate is changing, the demand and production ratio from clean energy sources are too unstable for the energy grid used today, as the sun does not always shine or the wind does not blow. A combination of both, production of energy by clean energy sources and energy storage is required to provide on-demand energy without emitting greenhouse gasses.

Lithium-ion batteries have shown an increase in capacity and efficiency during recent years as a result of moving away from fossil fuels as energy sources. However, these batteries suffer from a rapid decrease in capacity over time while being used. This is unsuitable because energy has to be stored over an extended time period, and charge-discharge cycles may occur in rapid succession depending on production and demand. Within this scenario, fuel cell and electrolyser technology are advocated to play a vital role in the future. For these types of electrochemical cells, the energy is stored as chemical energy in the form of hydrogen gas and then used to produce electricity whenever needed with the byproduct water. Unfortunately, the production of hydrogen by electrolysis is not energy efficient due to the overpotential needed to split water. Therefore, most hydrogen is produced from hydrocarbons with the emission of greenhouse gasses, as shown in Figure 1.1 [1].

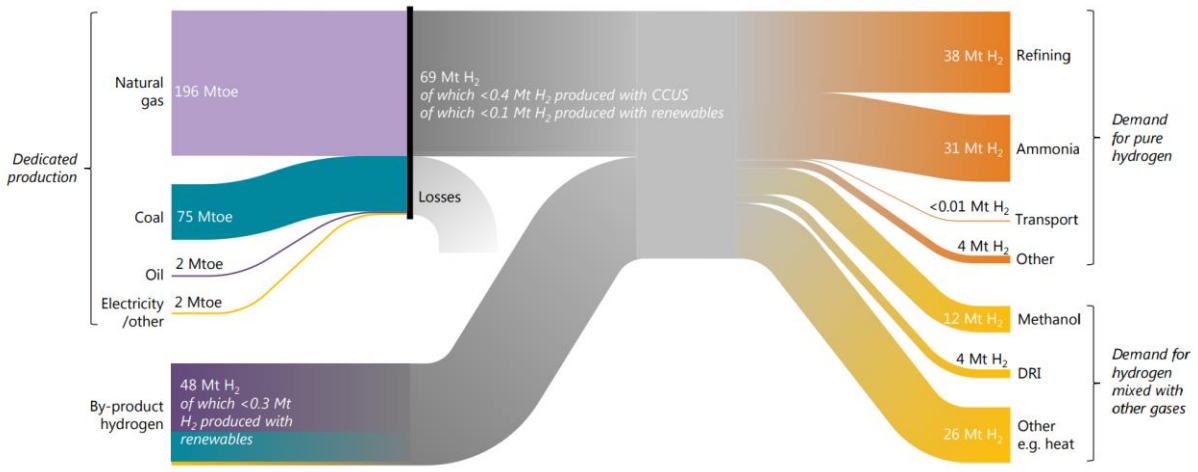

Figure 1.1 The hydrogen value chain shows that a small amount of the produced hydrogen is from renewable sources and carbon-capturing technology compared to natural gas [1].

Commercially adopted fuel cells based on water-containing polymers (PEMFC) are struggling with slow electrode kinetics regardless of the use of noble-metals, in combination with poor tolerance toward fuel impurities, due to the low operating temperature, i.e. < 100 °C [2]. Other types of electrochemical cells such as Solid Oxide Electrochemical Cells (SOECs) are operating at a higher temperature range of 700 – 1000 °C, do not require noble metals, offer fuel flexibility and have conversion efficiencies between 50 - 60 %. Furthermore, they have shown potential in both commercial application and large-scale power generators. The SOECs are operating with an oxide ion-conducting electrolyte, where the fuel side is diluted with steam, and oxygen gas is obtained on the other side of the cell, as shown in Figure 1.2. The high temperature of Solid Oxide Electrolysers (SOEs) results in the advantage of utilising the heat as a part of the energy supplied to vaporise water and thus lowering the electricity needed for the process [3]. Despite the advantage, the high temperatures required for ionic conductivity in solid materials due to slow kinetics and high activation energy lead to challenges such as material instability, lower durability, and accelerated thermal ageing resulting in a shorter lifespan and higher material cost. Hence, there is an interest in decreasing the operating temperature.

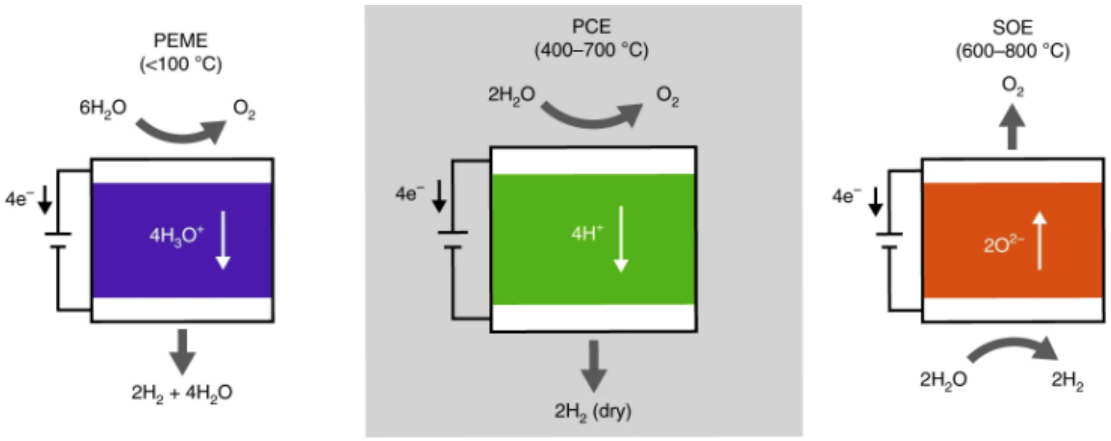

Figure 1.2 Comparison between Proton Exchange Membrane Electrolyser (PEME), SOE and Proton Ceramic Electrolyser (PCE) [4].

Regarding this, Proton Ceramic Electrochemical Cells (PCECs) have received significant attention, due to the lower activation energy for proton transport than for oxide ions, which results in lower operating temperatures required, i.e. 400 – 600 °C [5]. Due to the potential of performing with greater efficiency at lower temperatures, the PCECs are a promising alternative to SOECs. The PCECs are operating with a proton-conducting ceramic as the electrolyte, where in comparison to SOECs the fuel is not diluted during operations, as shown in Figure 1.2, resulting in higher operating cell voltage and efficiency. While the proton ceramic electrolyte development has achieved a state of the art electrolyte for these purposes, the necessity of efficient electrodes slowed the industrial application for PCECs. The low operating temperatures are resulting in reduced ionic conductivity and consequently increased polarisation resistance, especially at the oxygen/water-side electrode. These problems contribute to the low power output, where the electrode kinetics currently limit the performance of the PCEC [6].

As the electrode botheration was established, several attempts using electrodes used for SOECs in PCECs were made, which resulted in high polarization resistances. Research on SOECs has established that the best electrode materials exhibit mixed ionic and electronic conductivity in order to increase the reaction zone, i.e. the Triple Phase Boundary (TPB). SOECs prefer electrodes exhibiting mixed O^{2-}/e^{-} conductivity (MOEC). A MOEC electrode does not increase the TPB for PCECs. In order to extend the reaction area, the electrode needs to exhibit mixed protonic and electronic conductivity (MPEC). $BaGd_{0.8}La_{0.2}Co_2O_{6-\delta}$ (BGLC82) has shown to exhibit MPEC properties with p-type conductivity. BGLC82 has the lowest reported polarisation resistance currently for proton ceramic cells of 0.05 Ωcm^{-2} at 650 °C, and exhibit

activation energies down to 0.5 eV at lower temperature range (450 – 350 °C) [7]. In addition to showing Faradaic efficiency close to 100 % at 500 – 600 °C [4], BGLC can be considered as a state of the art electrode for PCECs. However, BGLC82 has shown to experience phase segregation at high water vapour pressure, as well as forming Co-oxides at the surface under normal operating conditions.

1.2 Aims and Contents

As mention above, the lack of specialised electrodes for PCECs, hinders the development of commercial PCECs. By using BGLC82 as a backbone in developing new and efficient electrode materials, the primary object of this thesis is to study the functional properties of selected doped BGLC82 materials, with their focus as electrode materials for PCECs. $BaGd_{0.8}La_{0.2}Co_{1.8}X_{0.2}O_{6-\delta}$ (X= Ti, Zn and Zr), with different cation substitutes for cobalt, will be synthesised and characterized with respect to the crystal structure, hydration, and electrode kinetics.

The crystal structure and morphology of the synthesised electrodes will be investigated through X-ray Diffraction (XRD) together with Scanning Electron Microscopy (SEM) and Energy Dispersive X-Ray Spectroscopy (EDS). The hydration properties of the electrodes will be investigated by isotherm dry/wet switches in various temperatures by means of Thermogravimetric Analysis (TGA). The electrochemical measurements will be conducted by a modified three-point electrode setup, where all the electrodes are placed on a $BaZr_{0.7}Ce_{0.2}Y_{0.1}O_3$ (BZCY72) electrolyte simultaneously, with the ability to measure on each electrode individually. The electrolyte will have a counter- and a reference electrode made of platinum and the electrochemical measurements will be realized by potentiostatic electrochemical impedance spectroscopy (EIS) under controlled atmospheres and temperatures. The EIS is used to delineate the electrode responses into ohmic and polarization contributions. The dependencies of the resistances and kinetic parameters will be investigated concerning temperature, pO_2 and pH_2O. By evaluating all the parameters of the electrodes, their performances will be compared to each other and with the literature results of pure BGLC82. Additionally, the rate-limiting step for each of the electrode will be determined.

Furthermore, the different electrodes will be measured at different potentials, which will enhance either the anodic or cathodic reaction. The measurements will yield a better understanding of the electrode kinetics and of the behaviour as an electrode for PCECs, where the cell is required to work both in fuel cell and electrolyser mode.

2 Theory

2.1 Electrochemical Cells

Electrochemical cells are systems that can use redox reactions to either, convert chemical energy to electrical energy or convert electricity to drive a chemical reaction. These types of cells are called galvanic- and electrolytic cells, respectively. The third type of electrochemical cells are equilibrium cells which are used in sensors, and will not be discussed in this thesis. When a current flows through an electrochemical cell, the potential will change from the equilibrium potential also called null voltage. This change in potential is known as overpotential (η) and is the difference between the standard electrode potential and the measured potential.

An electrochemical cell simply consists of two electrodes which are separated by an electrolyte. The electrolyte is an ion conductor, and the electrodes are electron conductors, connected to an external circuit.

2.1.1 Half-Cell Reaction

In this work, the electrode of interest is where the oxygen/steam half-cell reaction takes place. When the electrochemical cell is set at fuel cell mode, the electrode of interest is reducing oxygen, thus works as a cathode. When the cell switches to electrolyser mode, the electrode is oxidising water to produce protons and oxygen gas, thus becomes an anode. Due to the standard reduction potential being higher than for the hydrogen electrode in both of the cases, the electrode is hereafter called positrode, whereas the hydrogen electrode is then referred to as negatrode.

For a PCEC, the negatrode oxidises hydrogen gas to form protons and electrons in galvanic mode. The protons migrate through a ceramic electrolyte to the positrode, while the electrons flow through an external circuit. At the electrolyte/positrode interface, electrons and protons react with oxygen gas to form water. In electrolyser mode, the reactions are reversed, and there is a need for energy from an external source to drive the reactions.

The electrochemical reactions at each half-cell:

Hydrogen evolution reaction (HER) at the negatrode:

$$H_2(g) \rightleftharpoons 2H^+ + 2e^- \tag{2.1}$$

Oxygen evolution reaction (OER) at the positrode:

$$O_2(g) + 4H^+ + 4e^- \rightleftharpoons 2H_2O(g) \tag{2.2}$$

The total cell reaction would then be:

$$2H_2(g) + O_2(g) \rightleftharpoons 2H_2O(g) \tag{2.3}$$

2.2 Defect Chemistry

Any imperfection or deviation from the ideal periodicity in a crystalline lattice is a defect. The entropy favours the formation of defects at temperatures above 0 K to reduce Gibbs's energy. There are primarily two main categories of defects: electronic defects and structural defects. Electronic defects are electrons and holes which to some extend can move freely in the crystal. These defects are either formed by internal excitation or related to structural defects in terms of compensation. The structural defects are defects which are in fixed sites in the structure, which either is formed intrinsically by internal reactions within the material, or extrinsically through interaction with other phases.

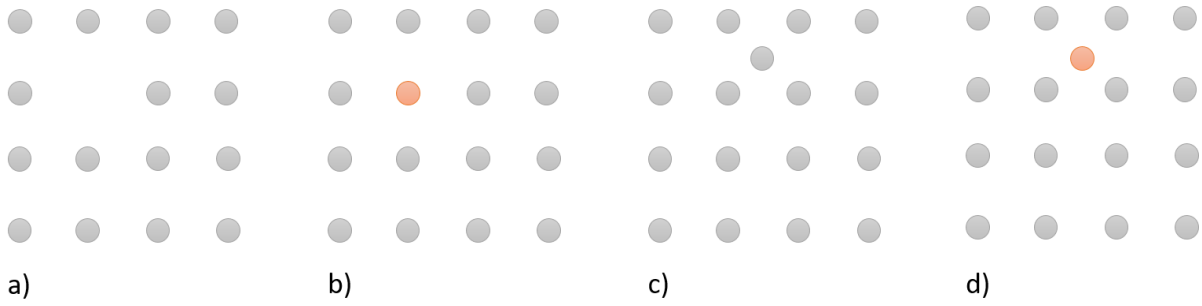

Figure 2.1 Structural defects that can be present are a) vacancies, b) substitutional foreign atom, c) interstitial host atom and d) interstitial foreign atom.

All types of defects that are mention above and shown in Figure 2.1 can be present simultaneously, but often there will be some of the defects that dominate. Defect concentrations and the dominating defect depend on the thermodynamic of defect equilibria. To understand defect equilibria at different conditions, it is necessary to have a standard in formulating chemical equations for defect reactions, which is expressed by using the Kröger-Vink notation for point defects.

2.2.1 Kröger-Vink Notation

The Kröger-Vink notation (K-V) was proposed as a notation for point defects by Kröger and Vink in 1956. This notation describes any structural element in a crystal, in terms of what their chemical content is and what kind of structural position it occupies in the unit cell. The general notation is A_s^c, where A refers to the element (H, O, Zn, Fe, etc.) or a vacancy (v). The subscript s refers to a site in the crystal lattice, which is given by the element symbols or i for an interstitial site. The superscript c refers to the effective charge for the defect. The notation for effective charges are superscript •, / and x, for positive, negative and neutral defects, respectively. The effective charge is defined as the difference between the actual charge of the species minus the actual charge that the reference structure would have had on the same site. For example $v_O^{\bullet\bullet}$, O_O^x or N_O'. Electrons and holes are written as e' or n and $h^\bullet$ or p, respectively. Defect reactions are written in the same manner as ordinary chemical reactions and are balanced by conservation of mass, charge, and ratios of sites [8].

2.2.2 Defects in Oxides

Thermodynamics determines the defects in oxides and favours a small concentration of defects. Oxides in equilibrium with the surroundings are generally nonstoichiometric [9]. For oxides under experimental conditions, the activity of a cation is imperceptibly compared to the activity of the oxygen. Hence, the non-stoichiometry for oxides is, in general, determined by the oxygen exchange between the oxide and the atmosphere. These materials have either an excess or a deficiency of oxygen compared to their stoichiometry. This property is controllable by varying the temperature and oxygen partial pressure of the system.

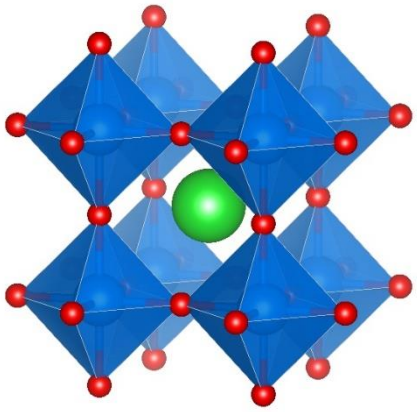

Figure 2.2 The unit cell of $BaZrO_3$ [10].

Figure 2.2 shows the crystal structure of $BaZrO_3$, which has shown properties of proton conductivity. The formation of protonic defects occurs primarily due to the presence of oxygen vacancies. These vacancies can be formed intrinsically by Schottky disorder or oxygen deficiency, and charge compensated by metal vacancies (v''_{Ba} and v'''_{Zr}) or electrons. Commonly, $BaZrO_3$ is doped with a lower valent cation for Zr^{4+} to increase the stability of protonic defects, which is known as acceptor doping. Y^{3+} is usually used as the dopant for $BaZrO_3$, which gives chemical formula $BaZr_{1-x}Y_xO_{3-\delta}$ (BZY). This dopant gives effectively negative sites (Y'_{Zr}), which may be charge compensated by oxygen vacancies.

$$2BaCO_3\ (s) + Y_2O_3\ (s) \overset{ZrO_2}{\longleftrightarrow} 2Ba^x_{Ba} + 2Y'_{Zr} + v^{\bullet\bullet}_O + 5O^x_O + 2CO_2\ (g) \tag{2.4}$$

Under dry conditions, the acceptors and oxygen vacancies are the dominating defects, while electronic defects are minority defects. Even though electronic defects are minority defects, BZY can exhibit a small concentration, which contributes to n- and p-type conductivities. These defects may occur to charge compensate the deviation from the stoichiometry of the material due to pressures, temperatures or doping.

Under high oxygen partial pressures, the oxygen gas reduces and forms electron holes within the structure, which may lead to p-type conductivity [11]:

$$\frac{1}{2}O_2\ (g) + v^{\bullet\bullet}_O = 2h^{\bullet} + O^x_O \tag{2.5}$$

Opposite under low oxygen partial pressures, oxygen vacancies are formed and compensated by electrons:

$$O_O^x = v_O^{\bullet\bullet} + 2e' + \frac{1}{2}O_2\,(g) \tag{2.6}$$

From reaction 2.5 and 2.6 the equilibrium constant for oxidation (K'_o) and reduction (K'_r), respectively, can be determined:

$$K'_o = \frac{a_{h^\bullet}^2\, a_{O_O^x}}{a_{v_O^{\bullet\bullet}}\, a_{O_2}^{1/2}} = \frac{p^2\,[O_O^x]}{[v_O^{\bullet\bullet}]}\left(\frac{pO_2}{pO_2^0}\right)^{-\frac{1}{2}} = p^2\,[v_O^{\bullet\bullet}]^{-1}\,pO_2^{-1/2} \tag{2.7}$$

$$K'_r = \frac{a_{v_O^{\bullet\bullet}}\, a_{e'}^2\, a_{O_2}^{1/2}}{a_{O_O^x}} = \frac{[v_O^{\bullet\bullet}]\,n^2}{[O_O^x]}\left(\frac{pO_2}{pO_2^0}\right)^{\frac{1}{2}} = [v_O^{\bullet\bullet}]\,n^2\,pO_2^{1/2} \tag{2.8}$$

The standard pressure, pO_2^0, is pO_2^0 = 1, and the defect concentration $[O_O^x]$ is assumed to be $[O_O^x]$ = 1 due to the domination of O_O^x over other defects. Equation (2.7) and (2.8) show that the concentration of electrons, holes, and oxygen vacancies is dependent on the oxygen partial pressure. The equilibrium constants can be related to the standard Gibbs energy (ΔG°) of the reaction:

$$K'_i = e^{\left(-\frac{\Delta G_i^o}{RT}\right)} = e^{\left(\frac{\Delta S_i^o}{R}\right)} e^{\left(-\frac{\Delta H_i^o}{RT}\right)} \tag{2.9}$$

Furthermore, oxides often gain protonic defects when exposed to water-rich atmospheres. The protonic defects occur by hydration, by the following defect reaction:

$$H_2O\,(g) + v_O^{\bullet\bullet} + O_O^x \rightleftharpoons 2OH_O^\bullet \tag{2.10}$$

With the corresponding equilibrium constant:

$$K'_{hyd} = [OH_O^\bullet]^2[v_O^{\bullet\bullet}]^{-1}pH_2O^{-1} \tag{2.11}$$

To calculate the dependency of each defect concentration, the electroneutrality conditions for the oxide need to be established. The electroneutrality is written such that the concentration of the effective negative and positive species are equal to each other. The total electroneutrality for BZY becomes [12]:

$$n + [Y'_{Zr}] = 2[v_O^{\bullet\bullet}] + [OH_O^{\bullet}] + p \tag{2.12}$$

Except for the doping concentration in BZY, the defect concentration are affected by specific partial pressures. The dopant is therefor a constant compensating defect for the opposite charge defects, which will stabilise the concentration of the compensating defect.

When BZY is exposed to a water-rich atmosphere with changing oxygen partial pressures, the electroneutrality can be rewritten to obtain boundary conditions at different pO_2 conditions. For low pO_2 conditions, the dominating defects are electrons and oxygen vacancies. The other defects can then be seen as minority defects, and the boundary condition becomes $n = 2[v_O^{\bullet\bullet}]$, due to the concentration of the minor defects $n \gg [Y'_{Zr}]$ and $[v_O^{\bullet\bullet}] \gg [OH_O^{\bullet}] + p$. Hence, the boundary condition for intermediate and high pO_2 becomes $[Y'_{Zr}] = 2[v_O^{\bullet\bullet}]$ and $p = 2[v_O^{\bullet\bullet}]$, respectively.

The pO_2 dependency for each defect can then be determined by Equation 2.7, 2.8 and 2.11, which is shown in the following table.

Table 2.1 pO_2 dependency at different electroneutrality conditions for acceptor doped $BaZrO_3$.

Boundary condition	**pO_2 dependency for [defects]**			
	p	n	$v_O^{\bullet\bullet}$	$OH_O^{\bullet}$
$\mathbf{n = 2[v_O^{\bullet\bullet}]}$	$pO_2^{1/6}$	$pO_2^{-1/6}$	$pO_2^{-1/6}$	$pO_2^{-1/12}$
$\mathbf{[Y'_{Zr}] = 2[v_O^{\bullet\bullet}]}$	$pO_2^{1/4}$	$pO_2^{-1/4}$	pO_2^{0}	pO_2^{0}
$\mathbf{[Y'_{Zr}] = p}$	pO_2^{0}	pO_2^{0}	$pO_2^{-1/2}$	$pO_2^{-1/4}$

Furthermore, the water vapour dependency for the oxide is obtained by the same method as the pO_2 dependency. Hence, the pH_2O changes from low to high with the pO_2 held constant. The boundary conditions for low and high pH_2O are $[Y'_{Zr}] = 2[v_O^{\bullet\bullet}]$ and $[Y'_{Zr}] = [OH_O^{\bullet}]$, respectively. The dependency can then be determined with equation 2.7, 2.8 and 2.11, and are presented in the following table.

Table 2.2 pH_2O dependencies at different electroneutrality conditions for acceptor doped $BaZrO_3$.

Boundary condition	pH_2O dependency for [defects]			
	p	n	$v_O^{\bullet\bullet}$	$OH_O^{\bullet}$
$[Y'_{Zr}] = 2[v_O^{\bullet\bullet}]$	pH_2O^0	pH_2O^0	pH_2O^0	$pH_2O^{1/2}$
$[Y'_{Zr}] = [OH_O^{\bullet}]$	$pH_2O^{-1/2}$	$pH_2O^{1/2}$	pH_2O^{-1}	pH_2O^0

The respective dependencies can then be illustrated in a Brouwer diagram, where the log of the defects concentrations is plotted against the log of the corresponding atmospheric dependency. The pO_2 and pH_2O Brouwer diagram are present in Figure 2.3 and Figure 2.4, respectively.

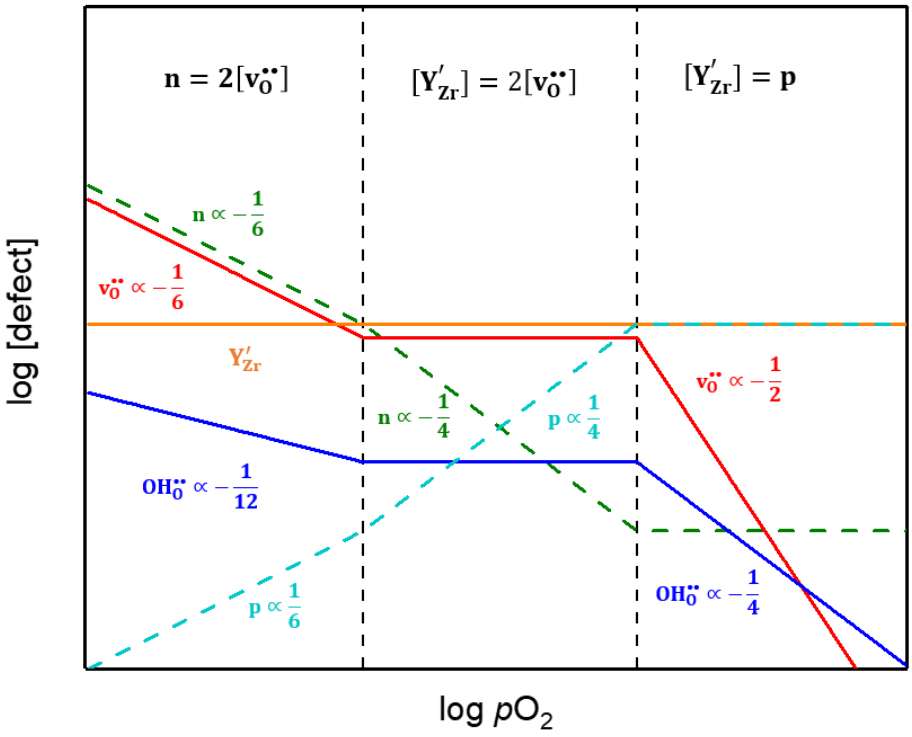

Figure 2.3 Brouwer diagram for BZY with changing pO_2.

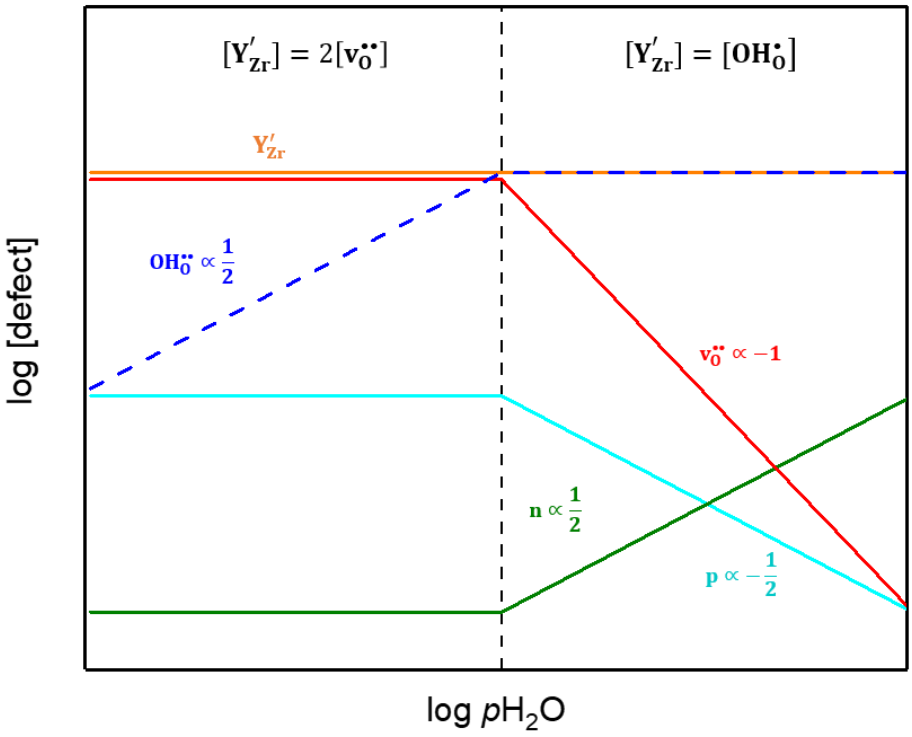

Figure 2.4 Brouwer diagram for BZY with changing pH_2O.

As shown above, the defect models of a pure proton conductor rely upon that the electronic defects are the minority defects. However, this model does not apply for mixed electronic and ionic conductors such as BGLC, where the electronic defects are no longer a minoity. A defect model for BGLC has been proposed by Vøllestad et al. [13] where the pO_2 dependency affects the concentration of the Co oxidation states:

$$\frac{1}{2}O_2\,(g) + v_O^{\bullet\bullet} + 2Co_{Co}^{1/2\prime} \rightleftharpoons O_O^x + 2Co_{Co}^{1/2\bullet} \tag{2.13}$$

$$\frac{1}{2}O_2\,(g) + v_O^{\bullet\bullet} + Co_{Co}^{3/2\prime} \rightleftharpoons O_O^x + Co_{Co}^{1/2\bullet} \tag{2.14}$$

$$\frac{1}{2}O_2\,(g) + v_O^{\bullet\bullet} + 2Co_{Co}^{3/2\prime} \rightleftharpoons O_O^x + 2Co_{Co}^{1/2\prime} \tag{2.15}$$

where the Co oxidation states are set as +3.5 when considering $\delta = 0$. The defect model for BGLC suggests that the oxide experiences p-type conductivity as a result of increasing number of Co^{4+} in the structure, with increasing partial pressures of oxygen, as shown in Figure 2.5.

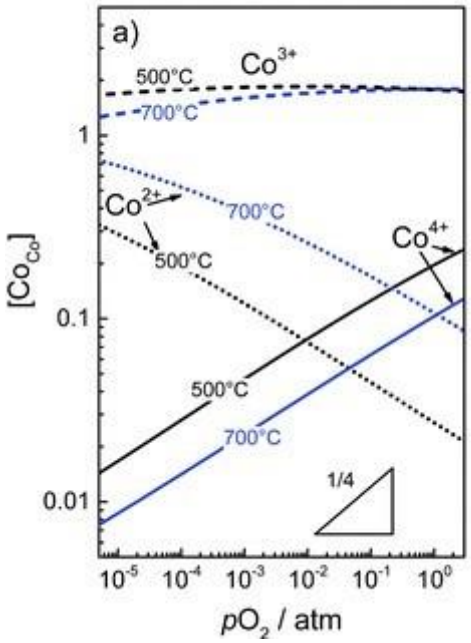

Figure 2.5 Concentration of Co 2+, 3+ and 4+ vs. pO_2 for 500 °C and 700 °C [13].

Due to the electronic defects not being minority defects, the way to produce protonic defects change compared to the BZY model. As explained above, the protonic defects are created by the hydration of the oxide by consuming oxygen vacancies. However, for oxides which are considered as possible positrode materials with mixed-valent transition metals ions, the situation is more complicated. For these materials, the protonic defect can also be obtained by hydrogenation, where the mixed-valent transition metals change their oxidation state to form protonic defects. For simplicity, reaction 2.10 and 2.13 are combined to describe the proton uptake at the expense of a hydrogenation:

$$H_2O\,(g) + 2O_O^x + 2Co_{Co}^{1/2\bullet} \rightleftharpoons 2Co_{Co}^{1/2\prime} + 2OH_O^\bullet + \frac{1}{2}O_2(g) \tag{2.16}$$

The hydrogenation has been shown both theoretically and experimentally [14, 15] and the conditions determine whether the proton uptake is from hydration or due to hydrogenation.

The electroneutrality for BGLC when hydrated can be expressed as:

$$2[v_O^{\bullet\bullet}] + \frac{1}{2}\left[Co_{Co}^{\frac{1}{2}\bullet}\right] + [La_{Ba}^\bullet] + [OH_O^\bullet] = \frac{3}{2}\left[Co_{Co}^{\frac{3}{2}\prime}\right] + \frac{1}{2}\left[Co_{Co}^{\frac{1}{2}\prime}\right] \tag{2.17}$$

2.3 Transport in Oxides

For most electrochemical cells, there needs to be movement of reactants to the reaction sites and transport of products away from these sites to function. For PCECs, there are three types of transport mechanisms; migration, diffusion and convection. The last transport mechanism will not be discussed further in this thesis, due to the mobility of ions in solid oxides being independent of convection. Movement of charged species which occurs in response to a gradient of electrical potential is called migration. The following section is based on [8, 16].

The flow of particles is expressed through Fick's first law, where particles move from high to low concentration:

$$J = -D\frac{\delta c}{\delta x} \tag{2.18}$$

The J is the particle flux density, D is the diffusion coefficient and $\frac{\delta c}{\delta x}$ the concentration gradient of the particles.

When transport of a species, i, is affected by a driving force F_i, the particle flux density J_i is given by the product of the concentration of the particles (c_i) and the average drift velocity (v_i), which is a product of the force exerted on the particles and the mechanical mobility B_i, ($v_i = F_iB_i$):

$$J_i = c_i v_i = c_i F_i B_i \tag{2.19}$$

When species i with a charge, z_i, is exposed to an electric field E, the force on the particles is given by:

$$F_i = -z_i e\frac{\delta \varphi}{\delta x} = -z_i eE \tag{2.20}$$

where e is the elementary charge.

By combining equation 2.19 and 2.20 the flux density becomes:

$$J_i = -c_i B_i z_i eE \tag{2.21}$$

where the current density j_i is given by:

$$j_i = -z_i e J_i = -(z_i e)^2 c_i B_i E \tag{2.22}$$

The charge mobility (u_i) for a species is a product of the mechanical mobility multiplied with the magnitude of the charge of each particle ($u_i = |z_i| e B_i$). Then equation 2.22 can be rewritten as:

$$j_i = -|z_i| e c_i u_i E = -\sigma_i E \tag{2.23}$$

Equation 2.23 gives rise to an essential definition of the partial electrical conductivity of a species ($\sigma_i = |z_i| e c_i u_i$). The partial electrical conductivity unit can be Scm^{-1} or $\Omega^{-1}cm^{-1}$ and is an essential component in the understanding of conducting behaviour in solid oxides.

The total electrical conductivity (σ_t) for a material is given by the sum of all the partial conductivities of the charge carriers:

$$\sigma_t = \sum \sigma_i = \sigma_{ion} + \sigma_{el} \tag{2.24}$$

In most cases, one of the charge carriers dominates the conductivity, and the minority charge transport contributions are neglected. The mobility of electronic charge carriers is negligibly higher compared to ions. As seen in Equation 2.23, there are two parameters to enhance ionic conductivity: mobility and concentration. The mobility of species in a solid is increased by temperature, due to the higher energy the species has, and the jump attempts over the energy barrier that succeeds increases. The concentration of a species has been shown earlier to change by different atmospheric conditions, as shown in Figure 2.3 and Figure 2.4.

Electronic conductivity (σ_{el}) is related to the motion of the electronic charge carrier electrons and holes through, the substance. They are known as n- (σ_n) and p-type (σ_p) conductivity, respectively. The conductivity for each charge carrier is expressed in terms of their concentration and their corresponding mobilities (u_n and u_p):

$$\sigma_{el} = \sigma_n + \sigma_p = enu_n + epu_p \tag{2.25}$$

Ionic conductivity (σ_{ion}) on the other hand, occurs in the presence of vacancy sites or interstitial ions in the crystalline structure. The mobility of ions is due to the thermal activation of ion hopping, which is related to diffusion and follows the Nernst-Einstein relationship:

$$D_i = \frac{k_B T}{z_i e} u_i = \frac{k_B T}{c_i (z_i e)^2} \sigma_i \tag{2.26}$$

In equation 2.26, the D_i is the diffusion coefficient of charge species i, k_B is the Boltzmann's constant and T is the temperature in Kelvin.

Since the Nernst-Einstein relationship applies to jumping processes, the conductivity will have a temperature dependency, where the conductivity can be written in the Arrhenius form

$$\sigma_i T = \sigma_0 \, e^{-\frac{E_a}{k_b T}} \tag{2.27}$$

where E_a is the activation energy, that includes the enthalpy of formation and mobility of the hopping defect. σ_0 is the temperature-independent pre-exponential factor, which includes entropy of formation and mobility of the defect.

As mention previously, conductivity can be increased with the increase of defect concentration. When using BZY as an example, the conductivity can be related to the defect concentration through Equation 2.23 and 2.25. From the defect model of BZY, the pO_2 dependency of the defects is shown in Table 2.1. When combining the dependencies with Equation 2.23 and 2.25, the conductive changes at different boundary conditions that apply for the BZY model. For BZY, the total conductivity against pO_2 can be plotted, as illustrated in Figure 2.6, with the boundary condition represented in Table 2.1. From Figure 2.6, the ionic conductivity range can be increased with an increasing concentration of oxygen vacancies as the ionic conductivity would move with the y-axis in the illustration.

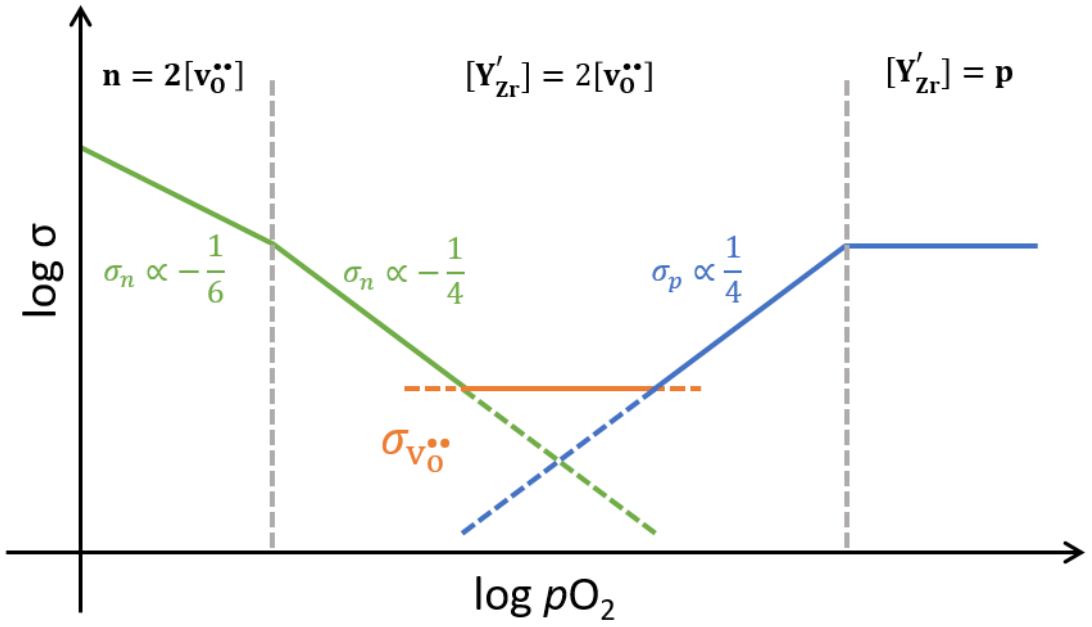

Figure 2.6 Illustration of conductivity measurements vs pO_2. The bold line shows the dominating conductivity. The ionic conductivity is here represented by the mobility of oxygen vacancies.

Proton Transport

When protons are dissolved in oxides, they usually associate with oxygen in the lattice to form hydroxide ions instead of occupying a lattice position. This is due to the lack of electron shells of protons and it will, therefore, interact strongly with the electron cloud of the oxide ion. A proton may move by two different mechanisms in an oxide: the vehicle mechanism and the free transport mechanism, also known as the Grotthuss mechanism.

The Grotthuss mechanism is the most common transport operation for protons in oxides. Here, the proton jumps from one oxide to another and then the hydroxide rotates to a position where a next jump can be successful. This rotation and reorientation are assumed to involve an activation energy where the jump itself is considered to be the rate-determining step.

In the vehicle mechanism, on the other hand, the proton is transported with the oxygen. The hydroxide ion then moves via oxygen vacancies or as an interstitial ion. The smaller radius of the hydroxide ion and the higher charge than the oxide ion gives it a smaller activation energy for diffusion than an oxide ion.

2.4 The Positrode

2.4.1 Electrode Polarisation

An electrode that remains at its null potential (E_n) while a current is applied to the electrode of either sign and any magnitude, is said to be totally depolarised. In contrast, when no Faradaic current passes at any potential, it is said to be totally polarised. When an electrode is totally depolarised, the electrode behaves like a resistor. However, when an electrode is totally polarised, the electrode behaves as a capacitor due to the double layer at the electrode/electrolyte interface.

For an electrode, the typical case is that a current runs through the electrode, which yields a potential loss or gain from E_n depending on the current direction. The difference between the E_n and the yield potential is known as overpotential (η). The overpotential is calculated by the difference between the null potential (E_n) and the measured potential (E):

$$\eta = |E - E_n| \tag{2.28}$$

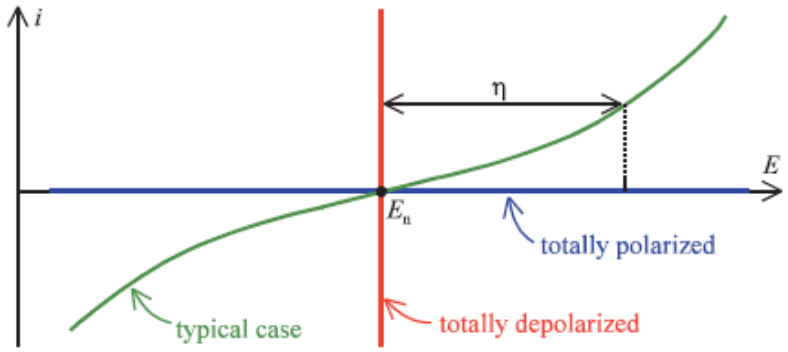

Figure 2.7 Illustration of electrode behaviour in the I-V curve when the electrode is totally polarized or depolarised and typical case [16].

Electrode polarization can be associated with the respective overpotential [16]. Kinetic polarisation is also known as charge transfer polarisation, which is due to the slow kinetics of the electrochemical reaction taking place. This behaviour occurs typically at the TPB in a PCEC, which contributes to a charge transfer overpotential (η_{ct}). Charge transfer polarisation can be seen in an I-V curve when the curve goes from a totally polarised behaviour to an increase in current when the potential increases.

Ohmic polarisation, which leads to ohmic overpotential (η_{ohm}), appears when a current flows across a cell and arises due to the motion of electrons and ions through the electrolyte and the electrodes. The ohmic overpotential can be seen as the linear part in an I-V curve and is related to Ohm's law; $\eta_{ohm} = IR_{cell}$ where R_{cell} represents the sum of resistance through the cell.

Transport or mass transport polarisation is due to the slowness of supply of the reactants or the removal of products at the electrode/electrolyte interface. As a result of a current that flows through the interface, a concentration gradient of reactants and products appears and leads to a mass transport overpotential (η_{mt}). The mass transport polarisation can be seen as the limiting current in an I-V curve.

2.4.2 Triple Phase Boundary

For PCEC, electrode reactions take typically place at the electrode/electrolyte interface, which is in contact with the gas phase. These areas that connect all three phases are referred to as the TPB, shown in Figure 2.8. The TPB allows the electrode reaction to occur due to the presence of all the reactance at the same time [17]. Hence, expansion of the TPB to also becomes on the positrode surface alone will increase the reaction rate as well as the cell performance.

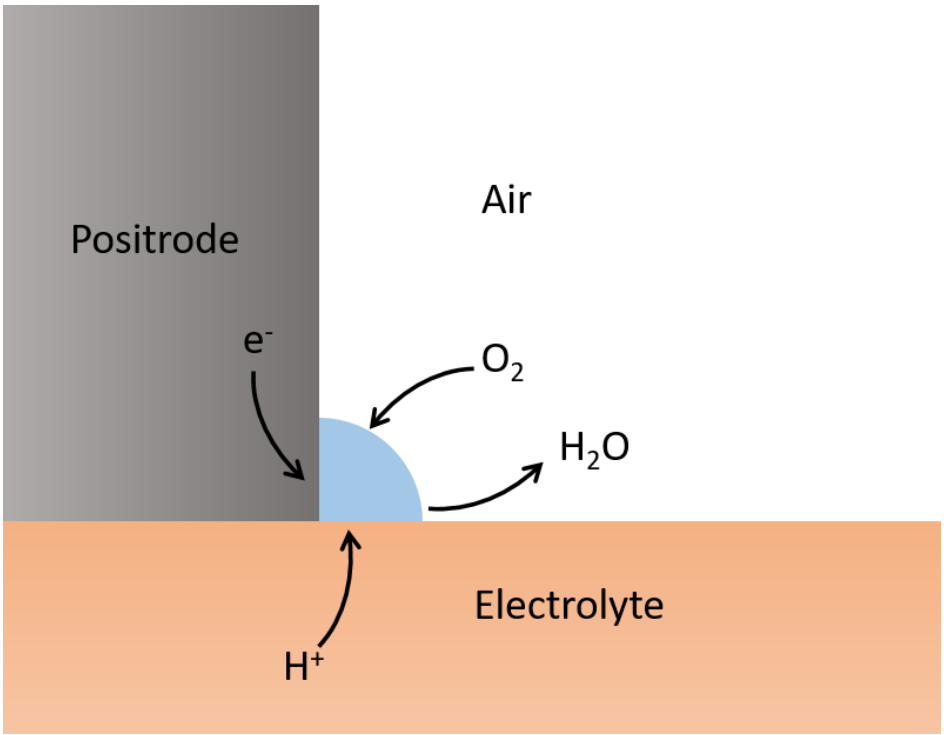

Figure 2.8 Illustration of the TPB (blue circle) when the positrode is a pure electronic conductor.

The OER at the positrode can be written as follow:

$$O_2(g) + 4e^-_{electrode} + 4H^+_{electrolyte} \rightleftharpoons 2H_2O\ (g) \quad (2.29)$$

Reaction 2.29 shows that the TPB is needed to make the reaction happen when there is only an electron conductor as the electrode.

2.4.3 Positrode Processes

The positrode reaction includes several processes that can be divided into two contributions; mass transfer (*mt*) and charge transfer (*ct*). These processes are driven by the concentration of the species, their mobility and their with each other. Mass transfers are processes that involve the exchange of species from one phase to another, i.e. diffusion, absorption and desorption. Charge transfers are in general associated with electron transfer such as redox reactions of species. However, the exchange or transfer of charge species between two phases is also associated as charge transfer contribution. For a PCEC, the exchange of protons from the electrolyte to the electrode or the TPB is seen as charge transfer processes. The pathways for the reaction depends on the properties of the electrode, which relate to the rate of the reaction, and therefore the kinetics at the electrode.

As the positrode experiences proton uptake either with or without oxygen vacancies, the possible positrode processes for a PCEC can be divide into two groups; with and without $v_O^{\bullet\bullet}$ assistance, a proposed by Poetzsch et al. [18].

First, the $v_O^{\bullet\bullet}$ assisted path:

1. Absorption/desorption of water on an oxygen vacancy represented as an open site *:

$$* + H_2O\ (g) \rightleftharpoons H_2O_{ads} \quad (2.30)$$

2. Splitting of absorbed water, mass transfer of protons on the surface:

$$H_2O_{ads} \rightleftharpoons H^+_{surf} + OH^-_{ads} \rightleftharpoons 2H^+_{surf} + O^{2-}_{ads} \quad (2.31)$$

3. Charge transfer oxidation of absorbed oxygen:

$$O^{2-}_{ads} \rightleftharpoons 2e^-_{electrode} + O_{ads} \quad (2.32)$$

3.1 Charge transfer oxidation of water:

$$O_{ads} + H_2O\ (g) \rightleftharpoons H_2OO_{abs} \rightleftharpoons O_{2_{abs}} + 2H^+ + 2e^- \quad (2.33)$$

4. Desorption/absorption of oxygen gas:

$$O_{2_{abs}} \rightleftharpoons O_2(g) + * \quad (2.34)$$

The second path without $v_O^{\bullet\bullet}$ assistance:

1. Absorption/desorption of water on the surface that is chemisorption to the surface:

$$2H_2O\ (g) \rightleftharpoons 2H_2O_{ch,abs} \quad (2.35)$$

2. Charge transfer, oxidation of water:

$$2H_2O_{ch,abs} \rightleftharpoons 2H^+_{surf} + 2OH_{ch,abs} + 2e^-_{electrode} \quad (2.36)$$

2.1. Second charge transfer, oxidation of oxygen:

$$2OH_{ch,abs} \rightleftharpoons 2H^+_{surf} + 2O_{ch,abs} + 2e^-_{electrode} \quad (2.37)$$

3. Absorption/desorption of oxygen from the surface:

$$O_{ch,abs} \rightleftharpoons O_{2_{surf}} \rightleftharpoons O_2(g) \quad (2.38)$$

Furthermore, both of the pathways follow the same path of proton transportation:

1. Diffusion of protons, from the surface to bulk or surface to TPB:

$$H^+_{surf} \rightleftharpoons H^+_{bulk} \text{ or } H^+_{surf} \rightleftharpoons H^+_{TPB} \quad (2.39)$$

2. Charge transfer of protons from the electrode to the electrolyte:

$$H^+_{Bulk/TPB} \rightleftharpoons H^+_{Electrolyte} \quad (2.40)$$

The reaction rate for each process depends on different factors like involved species, electrode properties, active reaction sites and geometry. All the reaction steps are considered to be in equilibrium when a current flows through the electrochemical cell, except the rate-determining step (RDS). The RDS is known to be the slowest step of the processes and cause an overpotential with a related polarisation resistance, which determines the overall reaction rate.

2.5 Kinetics of electrode reactions

2.5.1 Activation Energy

Whenever a Faradaic reaction takes place on a surface, interface or in a solution, there is an energy barrier to overcome. Furthermore, experiments have shown that most rate constants vary with temperature. This behaviour was first recognised by Arrhenius, and the proposed that the rate constant ofa reaction is dependent on the energy barrier and the temperature:

$$k = A_0 e^{-\left(\frac{E_A}{RT}\right)} \tag{2.41}$$

The equation is known as the Arrhenius equation, where E_A is the activation energy and A_0 is known as the pre-exponential factor. The exponential factor expresses the probability of surmounting the activation energy, whereas the pre-exponential factor is related to the frequency of attempts of the reaction, thus also known as the frequency factor.

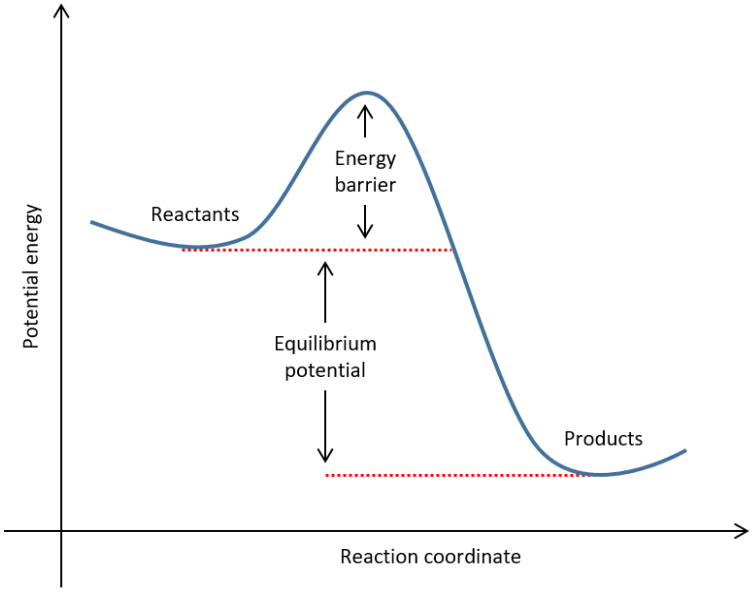

Figure 2.9 Simple illustration of potential energy change of an exothermic reaction [19].

The idea of activation energy has led to the illustration of reaction paths in terms of potential energy along a reaction coordinate, as illustrated in Figure 2.9. The height of the energy barrier is the activation energy of the reaction. In general, the reaction coordinate shows the progress of a favoured path for a chemical reaction.

2.5.2 Rate of Charge Transfer Electrode Processes

The charge transfer processes, as mentioned earlier, include electron transfer and transfer of charge species over an interface. The rate of the charge transfer processes is dependent on the potential difference at the interface and can, therefore, be related to the Faraday current. This section is based on [19] and [16].

Faradaic current is directly proportional to the rate of an electrochemical reaction. For electrodes, the reactions are known to be heterogeneous, as the reaction occurs only at the electrode surface or phase boundaries. Hence, the rate depends on the mass transfer to the electrode, surface effects and kinetic limitations. Furthermore, the reaction rate (r) is described in units of mol/s per unit area:

$$r = \frac{i}{nFA} = \frac{j}{nF} \tag{2.42}$$

where j is the current density (A/cm^2), n is the stoichiometric number of electrons consumed in the reaction and F is the Faraday's constant.

When considering reversible electrochemical reactions, there is a forward and a backward reaction, also known as a cathodic and anodic reaction depending on the reaction direction. The reaction rate for the direction (d) can then be written as:

$$r_d = k_d a_i = \frac{j_d}{nF} \tag{2.43}$$

where k_d is the rate constant for the given direction, a is the activity of the species (i) and j_d is the current densite for the direction. The current density for the reaction can then be written as:

$$j = j_c - j_a = nF(k_c a_i - k_a a_i) \tag{2.44}$$

where a and c stands for anodic and cathodic direction, respectively.

The charge transfer reaction between the electrode and the electrolyte can be seen as a single charge reaction, where the proton needs to overcome an energy barrier to move across the interface. When the reaction is running in fuel cell mode, as shown in Reaction 2.40, the forward reaction becomes where the proton moves from the electrolyte over to the TPB, which is the cathodic reaction. Hence, the backward reaction becomes the anodic contributions, and the net current density for the charge transfer reaction becomes:

$$j_{ct} = j_c - j_a = nF(k_c a_{\mathrm{H}^+_{\mathrm{ely}}} - k_a a_{\mathrm{H}^+_{\mathrm{TPB}}}) \tag{2.45}$$

Since the activity of protons is in equilibrium with the atmospheric pressure ($p\mathrm{O_2}$ and $p\mathrm{H_2O}$), the rate depends on the potential difference between the TPB and electrolyte.

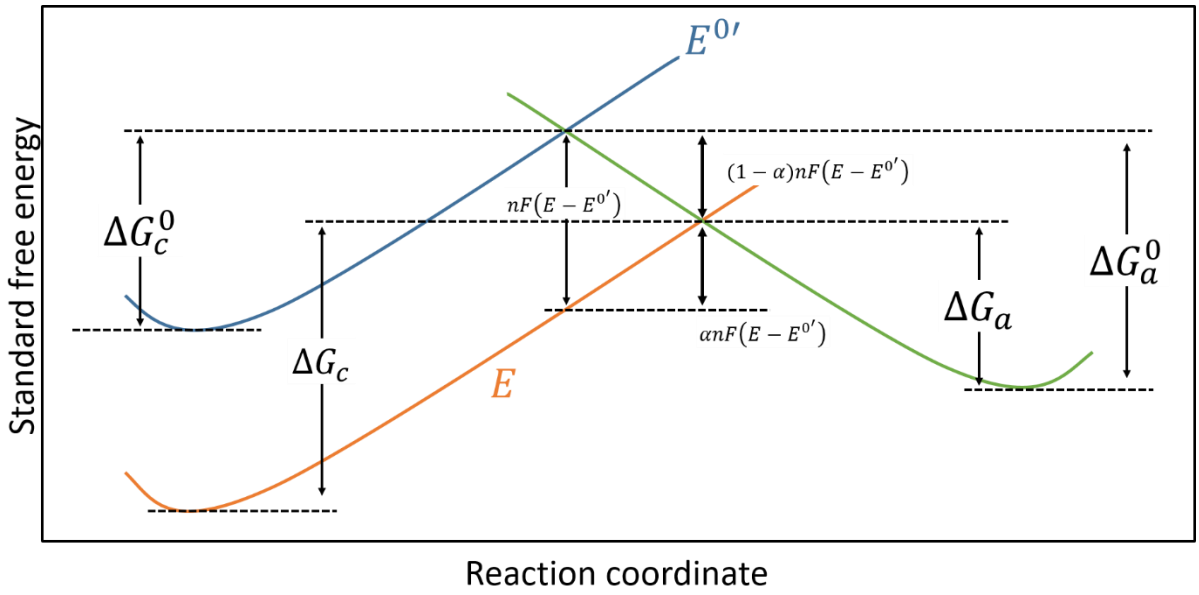

Figure 2.10 Effect of potential change on the standard free energy [19].

When the electrode potential (E) is equal to the formal potential ($E^{0\prime}$) and $E^{0\prime}$ is equal to the equilibrium potential (E_{eq}) ($E = E^{0\prime} = E_{eq}$), the cathodic and anodic activation energy become ΔG_c^0 and ΔG_a^0 , respectively. If E is changed from $E^{0\prime}$, the lower curve in Figure 2.10 moves by a change of $nF(E - E^{0\prime})$. If the change in potential is positive as shown in Figure 2.10, the anodic barrier (ΔG_a) has become less than ΔG_a^0, where the differences is equal to $(1-\alpha)nF\left(E - E^{0\prime}\right)$, were α is the transfer coefficient or the symmetry factor. As for the cathodic barrier (ΔG_c) and ΔG_c^0, the difference is $\alpha nF\left(E - E^{0\prime}\right)$. Hence, the cathodic and anodic barriers becomes:

$$\Delta G_a = \Delta G_a^0 + \alpha nF\left(E - E^{0'}\right) \tag{2.46}$$

$$\Delta G_a = \Delta G_a^0 - (1-\alpha)nF\left(E - E^{0'}\right) \tag{2.47}$$

The rate constant can then be assumed to have an Arrhenius form and be expressed as:

$$k_c = A_{0,c}\exp\left(-\frac{\Delta G_c}{RT}\right) = A_{0,c}\exp\left(-\frac{\Delta G_c^0}{RT}\right)exp\left(\frac{-\alpha nF\left(E - E^{0'}\right)}{RT}\right) \tag{2.48}$$

$$k_a = A_{0,a}\exp\left(-\frac{\Delta G_a}{RT}\right) = A_{0,a}\exp\left(-\frac{\Delta G_a^0}{RT}\right)exp\left(\frac{(1-\alpha)nF\left(E - E^{0'}\right)}{RT}\right) \tag{2.49}$$

The first part in these equations includes the pre-exponential and standard Gibbs free energy, which are independent of potential changes and can be written as k_c^0 and k_a^0. When considering the interface is in equilibrium, $E = E^{0\prime}$ and $k_c^0 = k_a^0 = k_{ct}^0$, then by inserting these relations into Equation 2.45, the net current density becomes:

$$j_{ct} = j_c + j_a = nFk_{ct}^0\left[a_{\mathrm{H}^+_{\mathrm{ely}}}exp\left(\frac{-\alpha nF\left(E - E^{0'}\right)}{RT}\right) - a_{\mathrm{H}^+_{\mathrm{TPB}}}exp\left(\frac{(1-\alpha)nF\left(E - E^{0'}\right)}{RT}\right)\right] \tag{2.50}$$

In equilibrium, the net current density becomes zero, and the electrode is known to adopt a potential based on the bulk concentration as imposed by the Nernst equation. The Equation 2.50 at zero current density and $n = 1$ becomes:

$$Fk_{ct}^0 a_{\mathrm{H}^+_{\mathrm{ely}}}exp\left(\frac{-\alpha F\left(E_{eq} - E^{0'}\right)}{RT}\right) = Fk_{ct}^0 a_{\mathrm{H}^+_{\mathrm{TPB}}}exp\left(\frac{(1-\alpha)F\left(E_{eq} - E^{0'}\right)}{RT}\right) \tag{2.51}$$

Since equilibrium applies, the bulk concentration of protons in the electrolyte ($a^*_{\mathrm{H}^+_{\mathrm{ely}}}$) and TPB ($a^*_{\mathrm{H}^+_{\mathrm{TPB}}}$) are equal to the surface concentration:

$$exp\left(\frac{F\left(E_{eq} - E^{0'}\right)}{RT}\right) = \frac{a^*_{H^+_{ely}}}{a^*_{H^+_{TPB}}} \tag{2.52}$$

However, there is still a Faradayc activity, which is known as the exchange current density (j_0), which is equal in magnitude to j_c or j_a. That is

$$j_{0,ct} = Fk_{ct}^{0} a_{\mathrm{H}_{ely}^{+}}^{*} \exp\left(\frac{-\alpha F\left(E_{eq} - E^{0'}\right)}{RT}\right) \tag{2.53}$$

When both sides of Equation 2.52 are raised to the power of $-\alpha$ and substituted into 2.53, it gives rise to:

$$j_{0,ct} = Fk_{ct}^{0} a^{*(1-\alpha)}_{\mathrm{H}_{ely}^{+}} a^{*\alpha}_{\mathrm{H}_{TPB}^{+}} \tag{2.54}$$

The exchange current density is proportional to the standard rate constant k_{ct}^{0}. Hence, a greater value of j_0 yields a small overpotential needed to reach a sizeable current flow. On the contrary, a large overpotential is needed for small values of j_0 for reaching a sizeable current flow. When α = ½ in Equation 2.54, the exchange current density increases with an order of ½, with increasing concentration (activity) of protons in the electrolyte and the TPB.

With j_0 the current density can be described in terms of the potential difference from the equilibrium potential, rather than the formal potential, by the following equation:

$$j_{ct} = j_{0,ct}\left[\frac{a_{\mathrm{H}_{ely}^{+}}}{a^{*}_{\mathrm{H}_{ely}^{+}}} \exp\left(\frac{-\alpha F\eta}{RT}\right) - \frac{a_{\mathrm{H}_{TPB}^{+}}}{a^{*}_{\mathrm{H}_{TPB}^{+}}} \exp\left(\frac{(1-\alpha)F\eta}{RT}\right)\right] \tag{2.55}$$

where $\eta = E - E_{eq}$.

If there are no mass transfer effects to the electrode, meaning the surface concentration does not differ from the bulk, Equation 2.55 becomes

$$j_{ct} = j_{0,ct}\left[\exp\left(\frac{-\alpha F\eta}{RT}\right) - \exp\left(\frac{(1-\alpha)F\eta}{RT}\right)\right] \tag{2.56}$$

and gives the current-potential relation known as the Butler-Volmer equation. The Butler-Volmer equation describes how the current density is proportional to the overpotential, which is required to overcome the energy barrier.

If the overpotential is sufficiently small, a Taylor expansion of the exponential term of the Butler-Volmer equation can be made, and the equation can be reexpressed as

$$j_{ct} = -\frac{j_{0,ct} F \eta}{RT} \tag{2.57}$$

The negative ratio between the overpotential and the charge transfer current density gives rise to a resistance known as the charge transfer resistance

$$\mathrm{R_{ct}} = -\frac{\eta}{j_{ct}} = \frac{RT}{F j_{0,ct}} \tag{2.58}$$

The equation shows that the charge transfer resistance approaches zero at larger $j_{0,ct}$, i.e. greater charge transfer kinetics.

However, for large values of overpotential, either positive or negative, one of the exponential terms becomes negligible. When a large cathodic overpotential arises $\left(\exp\left(-\frac{\alpha F \eta}{RT}\right) \ll \exp\left(\frac{(1-\alpha) F \eta}{RT}\right)\right)$, the Butler-Volmer equation becomes:

$$\mathrm{j_{ct}} = j_{0,ct} e^{\left(\frac{(1-\alpha) F \eta}{RT}\right)} \tag{2.59}$$

Or,

$$\eta = \frac{RT}{(1-\alpha)F} \ln j_{ct} - \frac{RT}{(1-\alpha)F} \ln j_{0,ct} \tag{2.60}$$

The last equation is known as the Tafel equation, which gives raise for the Tafel slope trough $\eta = a + b \log j$, wherein here:

$$a = -\frac{2.303RT}{(1-\alpha)F} \log j_{0_{ct}} \qquad b = \frac{2.303RT}{(1-\alpha)F} \tag{2.61}$$

The flatter the Tafel-slope, the better electrode kinetics, and less overpotential needed to reach mass transfer limitation, also known as mass transfer polarisation.

2.5.3 Rate of Mass Transfer Electrode Processes

As mentioned earlier, the mass transfer processes consist of diffusion of species and absorption and desorption of them. The rate of mass transfer is dependent on the rate constant and concentration of the different contribution that leading to mass transfer limitation for the positrode.

For PCECs, the first step in the electrode reaction, as shown earlier, is the exchange of water vapour (Reaction 2.30) on the surface. When expressing the rate of adsorption with Langmuir isotherm, the surface is thought to have a certain amount of active sites per unit area. The assumptions that all sites are equivalent and that adsorption only proceeds to a monolayer coverage are needed for the Langmuir isotherm model to be valid.

The fraction coverage (θ) of the sites is the occupied sites divided by the viable sites on the surface. When conditions are isotherm, the rate of assiociativ adsorption of water vapour on the electrode surface becomes:

$$r = p\mathrm{H_2O}k_{\mathrm{ads}}(1-\theta) - k_{des}\theta \tag{2.62}$$

When the system is in equilibrium, the absorption rate is equal to the desorption rate:

$$p\mathrm{H_2O}k_{\mathrm{ads}}(1-\theta) = k_{des}\theta \tag{2.63}$$

The equilibrium constant (K_{eq}) for the reaction is known to be k_{ads}/k_{des}:

$$\theta = \mathrm{K_{eq}}p\mathrm{H_2O} \tag{2.64}$$

The equation above can be rewritten as:

$$\theta = \frac{\mathrm{K_{eq}}p\mathrm{H_2O}}{1+\mathrm{K_{eq}}p\mathrm{H_2O}} \tag{2.65}$$

Hence, when the surface is mostly covered $\theta \approx 1$. However, under diluted conditions, the numbers of viable sites is known to by significant larger than the number of occupied sites, and θ can be neglected.

After absorption, charge transfer follows and then diffusion of the species. However, diffusion is a physical process caused by a concentration gradient, as mention earlier. Diffusion is, therefore, not a chemical reaction as it is not affected by potential changes and the particle flux of diffusion is given by Fick's first law, shown in Equation 2.18.

2.6 Electrochemical Impedance Spectroscopy (EIS)

EIS is an analytical tool used to study electrochemical kinetics at electrode interfaces and determination of conducting mechanisms in various materials. The following information in this section is based on [20, 21].

2.6.1 Impedance and Admittance

Under experimental circumstances, impedance is measured by using an alternating current (AC) voltage signal (U), which can be described as a sinusoidal function over time t:

$$\mathrm{U(t)} = \mathrm{U_0}\sin(2\pi f \mathrm{t}) = \mathrm{U_0}\sin(\omega \mathrm{t}) \tag{2.66}$$

where U_0 usually is a small amplitude given in volt, applied with a frequency *f* which can be expressed as the angular frequency $\omega = 2\pi f$. When a sinusoidal voltage is applied, the current will response as a sinusoid function with the same frequency only with a phase shift (ϕ). The current signal (I(t)) will, together with the phase shift, have a different amplitude, I_0:

$$\mathrm{I(t)} = \mathrm{I_0}\sin(2\pi f \mathrm{t} + \phi) = \mathrm{I_0}\sin(\omega \mathrm{t} + \phi) \tag{2.67}$$

This phase shift is a result of capacitive and resistive components in the circuit.

With the ratio of input voltage and the measured current the complex impedance of the system can be calculated by Ohm's law:

$$Z' = \frac{U(t)}{I(t)} = \frac{\mathrm{U_0}\sin(\omega \mathrm{t})}{\mathrm{I_0}\sin(\omega \mathrm{t} + \phi)} = Z_0 \frac{\sin(\omega \mathrm{t})}{\sin(\omega \mathrm{t} + \phi)} \tag{2.68}$$

By using Euler's relationship:

$$\mathrm{e}^{j\phi} = \cos\phi + j\sin\phi \tag{2.69}$$

the impedance can be express a complex function, where the potential and current are described as:

$$U(t) = U_0 e^{j\omega t} \tag{2.70}$$

$$I(t) = I_0 e^{j\omega t - j\phi} \tag{2.71}$$

By combining equation 2.68, 2.70 and 2.71:

$$Z' = Z_0 e^{j\phi} = Z_0(\cos\phi + j\sin\phi) = Z_{real} + jZ_{im} \tag{2.72}$$

The impedance can then be presented as a complex number, involving two components. One of the parts is the real component (Z_{real}), which is in phase with the applied voltage and is an obstacle for the charge transport, resistance. The second part is the imaginary component (Z_{im}), which is out of phase with the applied voltage, where j = $\sqrt{-1}$.

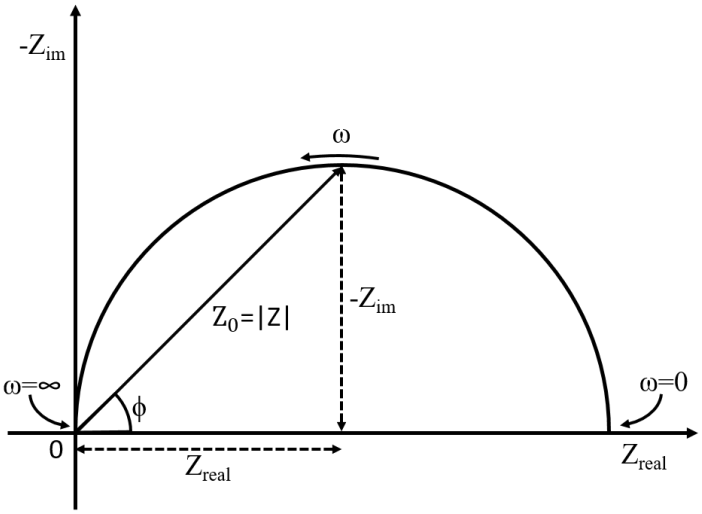

Figure 2.11 Illustration of complex impedance plot.

The inverse of impedance is admittance (Y). Admittance can be expressed as a complex number, like the impedance, with a real and imaginary component, conductance G and susceptance B, respectively. Admittance is measured in S (Simens) and is the inverse of impedance.

$$Y = \frac{1}{Z'} = \frac{I}{U} = G + jB \tag{2.73}$$

2.6.2 Equivalent Circuit and Circuit Elements

An equivalent circuit is a tool used to analyse the EIS measurements, which can describe the electrochemical processes taking place. To describe EIS measurement with an equivalent circuit, there are three circuit elements that are used: resistor, capacitor and inductor.

Resistor

For an ideal resistor, the voltage across it will give rise to a current instantly and therefore considered to be in phase with each other (ϕ=0). Hence, the impedance can be described as a real part (resistance) that is given by Ohm's law:

$$Z_R = R = \frac{U}{I} = \frac{U_0 \sin(\omega t)}{I_0 \sin(\omega t)} = \frac{U_0}{I_0} \tag{2.74}$$

Capacitor

A capacitor consists of two parallel plates, which are separated by a vacuum or a dielectric material. When voltage is applied, charge is built up, and the ability to store charge depends on the capacitance, C, where the general term of capacitance is:

$$\mathrm{C} = \varepsilon_0 \varepsilon_r \frac{\mathrm{A}}{\mathrm{L}} \tag{2.75}$$

where A is the area of the plates, L is the distance between them and ε_0 and ε_r are the vacuum – and relative permittivity, respectively. When an alternating voltage is applied over an ideal capacitor, a phase-shift current will be produced with $\phi = \pi/2$. Therefore, the impedance of a capacitor will consist of one frequency-dependent imaginary part:

$$\mathrm{Z_c} = \frac{1}{\mathrm{j}\omega \mathrm{C}} \tag{2.76}$$

where C is the capacitance of the capacitor with the units given in farad (F).

Inductor

In contrast to a capacitor, which is an ideal insulator, the inductor is an ideal conductor. When an alternating voltage is applied over the inductor, a phase-shift current is produced with $\phi=\pi/2$. The impedance of an inductor consists then of one frequency-dependent imaginary part:

$$Z_L = \mathrm{j}\omega L \tag{2.77}$$

Where *L* is the inductance of the inductor and is given with the unit henry (H).

Constant Phase Element (CPE)

A constant phase element (CPE) is a model used to describe non-ideal capacitor behaviour. A CPE can be recognised as a depressed semi-circle in the EIS measurements, and is a combination of resistance and capacitance. The impedance of this element is:

$$\mathrm{Z_{CPE}} = \frac{1}{Y_0(\mathrm{j}\omega)^n} \tag{2.78}$$

where the parameter *n* is related to the phase angle, and typically $0 \leq n \leq 1$. When $n = 1$, Y_0 acts like a pure capacitor, while for $n \approx 0$ the impedance acts as a pure resistor. The effective capacitance is calculated by:

$$\mathrm{C_{CPE}} = Y_0^{\frac{1}{n}} R_P^{\left(\frac{1}{n}-1\right)} \tag{2.79}$$

where the R_p is the corresponding polarisation resistance.

Randles circuit

The most common equivalent circuit used for simulating electrochemical interfaces is the Randles circuit. The circuit typically consists of an electrolyte resistor (R1) with its corresponding capacitor (CPE1) in series with the polarisation contribution from the electrode, which is generally, charge transfer resistance (R2) and mass transfer resistance (R3), and CPE2 and CPE3 are then the respective capacitance, as seen in Figure 2.12.

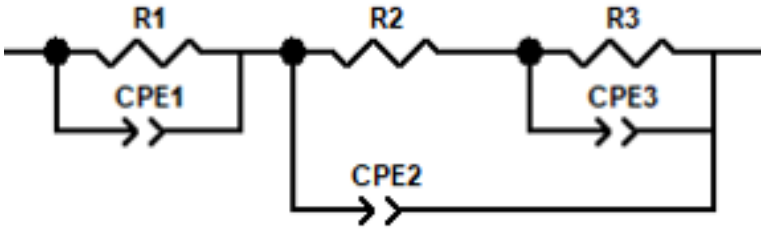

Figure 2.12 Randles type of circuit used for determining electrolyte (R1) and electrode contributions (R2 and R3).

2.6.3 Impedance spectra

EIS sweep contains information of the different contribution from the electrochemical cell. The different contributions are effected at different frequencies. Hence, a sweep is measured over a broad range of frequencies to cover all the contributions. The measurement is represented graphically by a Nyquist plot. By using a suitable equivalent circuit, the Nyquist plot can be simulated, and the values of interest can be extracted.

Nyquist plot

The most common graphical representation of impedance spectra is known as a Nyquist plot. The plot presents a graphical representation of both real and imaginary components.

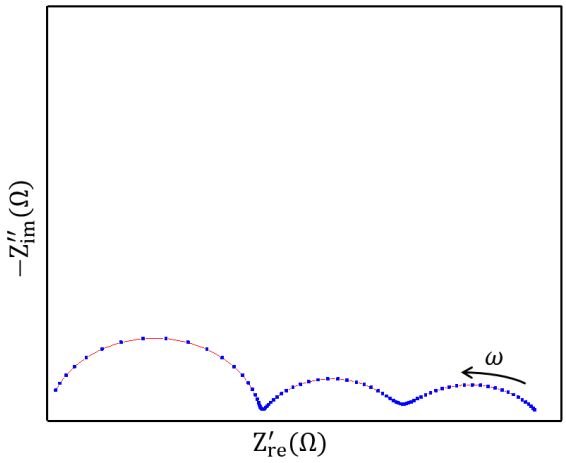

Figure 2.13 Illustration of a Nyquist plot, where the first semicircle is bulk or ohmic contribution at the higher frequencies, while the second and third are electrode contributions.

3 Literature

3.1 Ceramic Electrochemical Cells

Ceramic electrochemical cells (CECs) have shown several attractive advantages such as fuel flexibility, high fuel to electricity conversion, low environmental impact, and the absence of precious-metal catalysts [22-25]. The first generation of conventional CECs, SOECs, based on yttria-stabilised ZrO_2 (YSZ) electrolyte have a high operating temperature between 700 °C and 1000 °C. High operating temperatures of SOEC to achieve sufficient ionic conductivity and fuel utilisation result in several challenges connected to thermal stressing and limited compatible materials [3, 25, 26]. SOECs with samarium-doped ceria (SDC) electrolyte reported performance temperatures as low as ~ 600 °C [27, 28], but the performance drops rapidly with decreasing temperature due to the high activation energy for oxygen-ion conduction. In comparison, PCECs offer higher performance at a lower operating temperature due to the low E_a for proton conduction [29-31].

For SOECs, the fuel gas (H_2, CH_4) is diluted at the negatrode by the products or the reactants when using it in a fuel cell - or electrolyse mode, respectively [17, 26, 32]. For PCECs, however, the fuel at the negatrode will not be diluted, due to the production and usage of water happening at the positrode side.

The negatrode half-cell reaction for PCECs:

$$H_2\ (g) \rightleftharpoons 2H^+ + 2e^- \tag{3.1}$$

The positrode half-cell reaction for PCECs:

$$O_2(g) + 4H^+ + 4e^- \rightleftharpoons 2H_2O\ (g) \tag{3.2}$$

This property of fuel consumption at the negatrode and production at the positrode facilitates a higher fuel utilisation [33, 34], in comparison to SOECs.

3.1.1 Proton Ceramic Electrolytes

The first proton conduction at high temperatures was reported by Iwahara et al. [35] in a study of $SrCeO_3$-based oxides, in the early 1980s. From then on, perovskite-type oxides based on ABO_3 (A=Sr, Ba, Ca. B=Ce, Zr) [36-38] have been extensively studied for proton conduction and electrochemical applications such as fuel cells, electrolysers, hydrogen separation, etc. [39]. $BaCeO_3$- and $BaZrO_3$-based materials have shown to be benchmark materials among numerous of studied oxides [40-43], due to their high proton conductivity. Furthermore, these materials have tendencies to become mixed ionic conductors (H^+/O^{2-}) when they are exposed to a hydrogen-containing atmosphere and air on separate sides at high temperatures [44, 45].

The presence of oxygen vacancies ($v_O^{\bullet\bullet}$) in the oxide structure promotes, to a small extent, proton conduction in oxides. The presence of oxygen vacancies can be achieved by substitutional acceptor doping (A'_B) of the material structure, as in Equation 3.3. Often acceptor doped B-sites are charge-compensated by oxygen vacancies, holes or both, depending on the atmosphere constitution and temperature.

$$[A'_B] = 2[v_O^{\bullet\bullet}] + p \tag{3.3}$$

In a study by Iwahara et al. [46], $BaCeO_3$ was acceptor doped with different trivalent cations, to show the effect of proton transport compared to the ionic radius of dopant M in ($BaCe_{0.9}M_{0.1}O_{3-\delta}$). This study shows that the proton transport decreased with the increase of the ionic radius of M cation. The increase of the cation radius resulted in the orthorhombic structure becoming asymmetric, which promotes oxide ion transport rather than proton transport. Furthermore, Kreuer et al. [47, 48] studied the effect of M cation concentration and proton transport. The study revealed that proton mobility was drastically reduced with the increase of acceptor concentration, resulting in an increase of the basicity of the oxygens in the structure and therefore to stronger binding of protons to the oxygens. Results form quasi-elastic neutron scattering suggested that acceptor dopants may act as direct trap sites for protons [47].

Furthermore, proton conductivities for various oxides have been calculated from available data by Norby & Larring [29]. These results were summarised and illustrated over a range of temperatures by Kreuer [45], shown here in Figure 3.1.

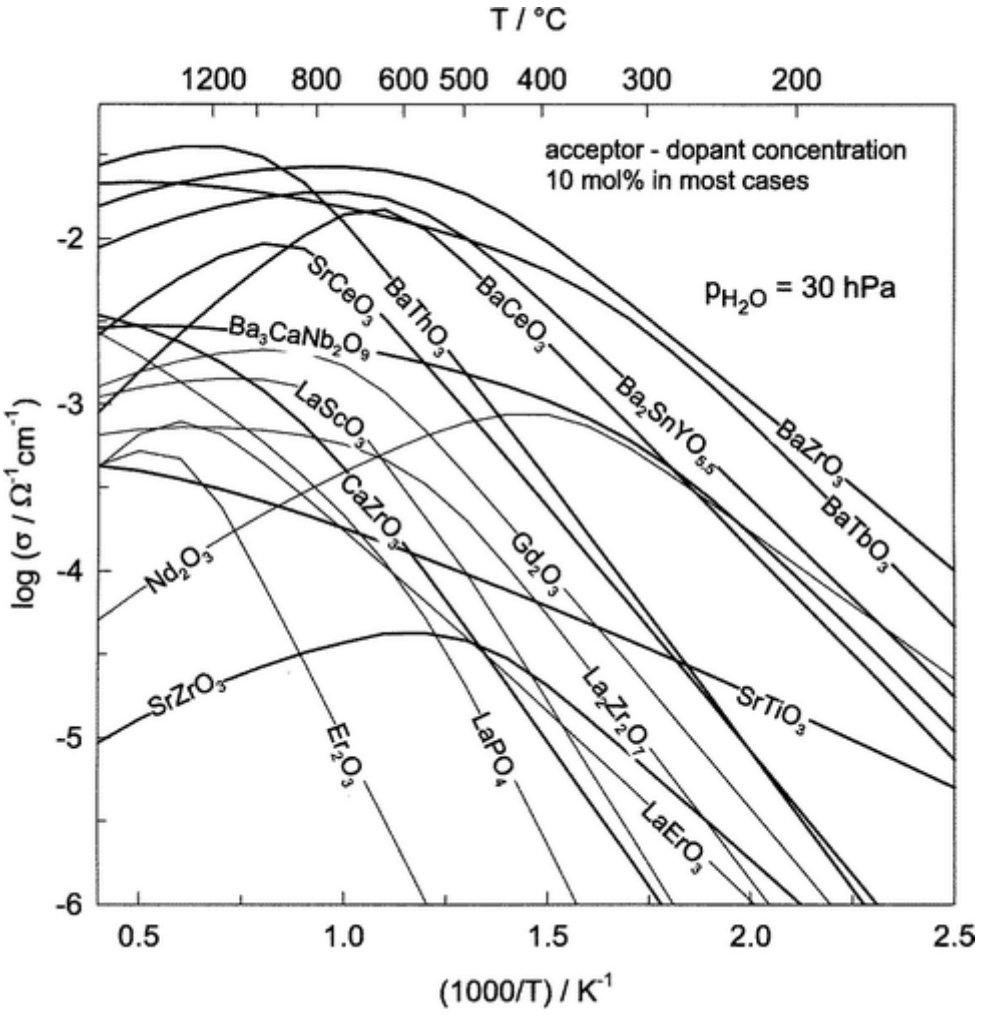

Figure 3.1 Proton conductivities for various oxides as a function of temperature [45].

Based on these studies, $BaCeO_3$- and $BaZrO_3$-based oxides were identified to be the most promising electrolyte for commercial usage, due to their high protonic conductivity. However, $BaCeO_3$-based oxides suffer from chemical instability when they are exposed to atmospheres containing CO_2 and water vapour, which react with the basic-cation to form $BaCO_3$ and $Ba(OH)_2$ [49, 50]. Furthermore, BZY has shown poor proton conductivity due to high grain boundary resistance and poor sinterability [51, 52]. In 2000 Katahira et al. [53] reported that Zr-substituted $BaCeO_3$ ($BaCe_{0.9-x}Zr_xY_{0.1}O_{3-\delta}$) (BZCY) improved the chemical stability against CO_2 when the Zr concentration was 40 % or higher ($x \geq 0.4$). A later study has also shown improved chemical stability in water vapour [54]. However, with an increase of Zr, the protonic conductivity decreases, together with increasing mixed protonic, oxide and electronic conduction at high temperatures [53, 54]. Despite the decreased protonic transport, BZCY has enticed much interest as material for PCECs, SOECs and other applications due to its stability [54-57].

3.2 Positrode Materials for PCECs

Although considerable research has been conducted in the development of materials as ceramic electrolytes for PCECs, the development of positrode materials has lacked behind. Several attempts to introduce positrode materials from SOECs have shown the necessity to take the reaction occurring at the positrode (Equation 3.2) into account.

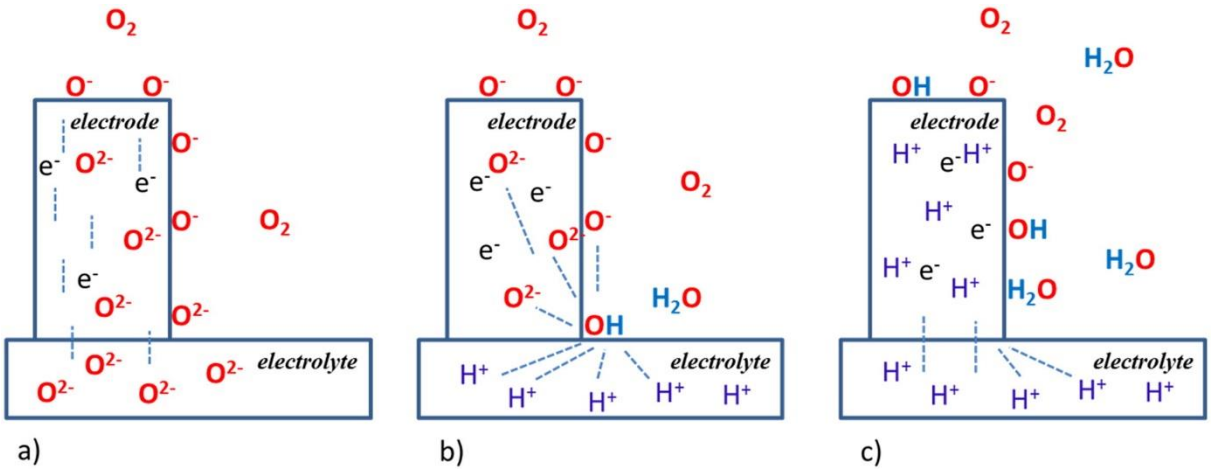

Figure 3.2 Illustration of (a) MOEC on an oxygen ion-conducting electrolyte, (b) MOEC conductor on a proton-conducting electrolyte and (c) MPEC on a proton conduction electrolyte [7].

Since the positrode reaction involves water vapour, the electrode requires a high porosity to allow water, to and away from the TPB. Platinum was broadly tested as positrode, due to its high catalytic activity. However, platinum exhibited high overpotential with proton-conducting electrolyte as well as increased Area Specific Resistance (ASR) when applied over electrolyte with increasing Zr content. In combination with the high material cost, platinum became not preferred in a broad-scale applications [57, 58]. Furthermore, MOECs have been tested as positrode for PCECs. Iwahara et al. [59] tested $La_{0.6}Ba_{0.4}CoO_{3-\delta}$, $La_{0.6}Ba_{0.4}MnO_{3-\delta}$ and $Ca_{0.85}Ce_{0.15}MnO_{3-\delta}$ as possible positrode materials. They reported that $La_{0.6}Ba_{0.4}CoO_{3-\delta}$ performed best among them, but without any significant improvement in comparison with a to a platinum positrode.

In 1999, Tao et al. [60] proposed that candidates for positrode materials for PCEC should exhibit high electronic and proton conductivity, together with acceptable catalytic activity. They additionally suggested that the positrode reaction (Equation 3.2) can be divided into:

$$\frac{1}{2}O_2\,(g) + 2e^- \rightleftharpoons O^{2-} \tag{3.4}$$

$$2H^+ + O^{2-} \rightleftharpoons H_2O\,(g) \tag{3.5}$$

Reaction 3.4 occurs at the surface of the positrode while Reaction 3.5 occurs at the TPB when the positrode is a metal or MOEC. However, positrode materials that obtain MPEC properties would extend the TPB zone to the surface area of the positrode and thus lead to faster kinetics of the electrochemical processes, as shown in Figure 3.2 c). Hence, MPEC materials have captured great interest, as promising positrode materials for PCECs.

3.2.1 Mixed Protonic and Electronic Conductors (MPEC)

In order for oxides to have proton conductivity, the oxide requires protonic defects in the lattice structure. The concentration of these protonic defects is related to the ability of water uptake of the oxide, i.e. hydration. Protonic defects in oxides are preferably not occupying a lattice site, but rather to stick to an oxide ion to form hydroxides on oxygen sites ($OH_o^{\bullet}$). Protonic defects in oxides have shown to either appear due to hydration (Equation 2.11) or hydrogenation (Equation 2.16).

Perovskite (ABO_3) structured materials have shown to fulfil these properties, as the B-site cations are generally mixed-valent transition metals which allow for oxygen flexibility, electronic conductivity and catalytic activity. The A-site cations are usually alkaline earth or rare earth metal, that provides the necessary basicity to stabalise protons together with substantial higher valent cation to introduce oxygen vacancies [61-63]. Double perovskite ($AA'BB^*O_6$) materials have shown to be sufficient positrode candidates as well, with the large variety of cations on A-site and B-site cation redox capability. The different A-sites are commonly a lanthanide and alkali earth mix, that form partial vacant oxygen sublattices [64-68].

The study of Zohurian et al. [69] shows that the basicity of the oxides has a significant effect on the proton uptake of oxides. In the study, several compositions in the perovskite family (Ba, Sr, La)(Fe, Co, Zn, Y)$O_{3-\delta}$, which were thought to be potential positrode materials for PCFCs were studied for their water uptake by Thermogravimetric Analysis (TGA). The study revealed that an increase of Ba on A-site increased the proton concentration. However, a small amount

of substitutional La with Ba was necessary for the stability of the cubic perovskite structure. The study also demonstrated that the basicity of the B-site cations is key for proton uptake for the oxide, as shown in Figure 3.3.

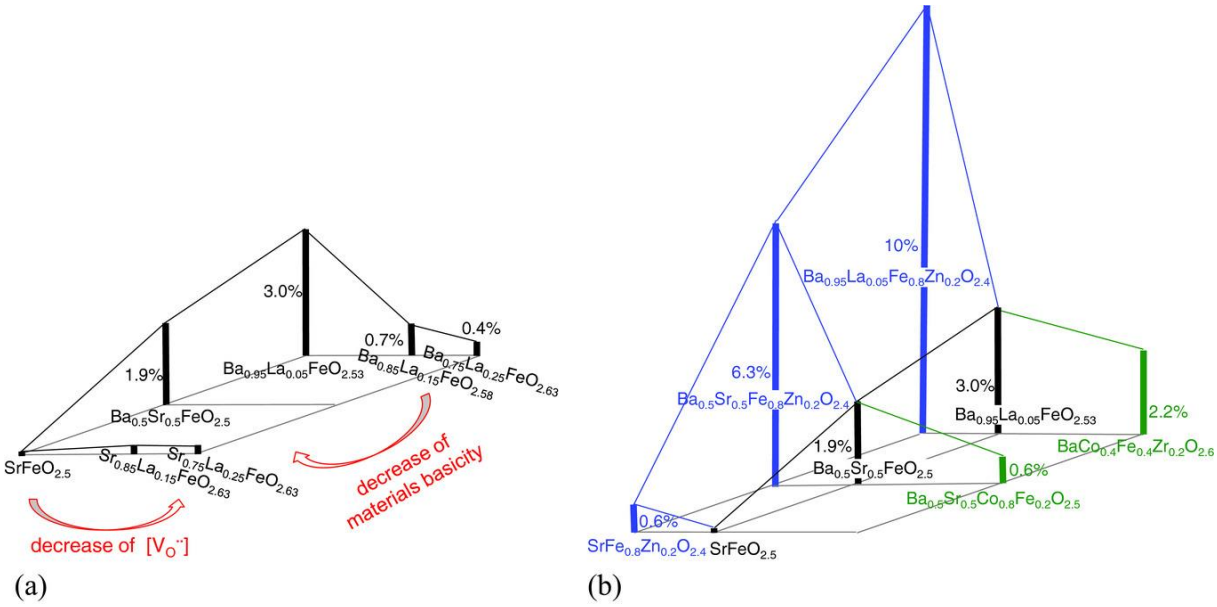

Figure 3.3 Proton uptake for oxides shown in mol % (z-axis) at 250 °C and $pH_2O \approx 0.016$ atm. a) Variation of La and Sr content on A-site. b) Effect of substitution of Zn and Co on the B-site [69].

3.2.2 $BaGd_{0.8}La_{0.2}Co_2O_{6-\delta}$ (BGLC)

In 2015 $BaGd_{0.8}La_{0.2}Co_2O_{6-\delta}$ (BGLC82) was proposed as a MPEC by Strandbakke et al. [7]. BGLC, together with $BaPrCo_2O_{6-\delta}$ (BPC), $BaGdCo_{1.8}Fe_{0.2}O_{6-\delta}$ (BGCF) and $BaPrCo_{1.4}Fe_{0.6}O_{6-\delta}$ (BPCF) were tested for hydration properties, oxygen stoichiometry and performance as positrodes on $BaZr_{0.7}Ce_{0.2}Y_{0.1}O_{3-\delta}$ (BZCY72) electrolyte. All of the samples have the same crystal structure as a double perovskite illustrated in Figure 3.4.

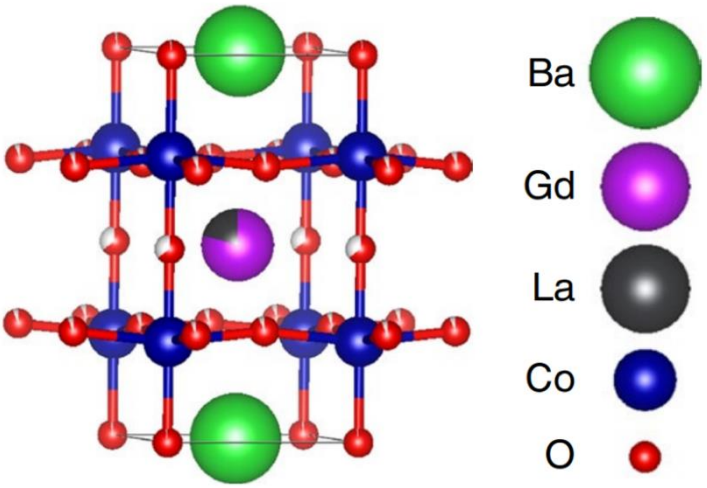

Figure 3.4 BGLC double perovskite structure with δ = 0.5

TGA revealed that the Gd-containing samples showed a higher oxygen deficiency than the Pr-samples, where BGLC showed the highest deficiency (Figure 3.5 a)). However, BGLC was the only sample that showed hydration at 400 °C and $pO_2 = 4 \cdot 10^{-4}$ atm with a switch from $pH_2O = 3 \cdot 10^{-5}$ atm to pH_2O = 0.02 atm. The weight gain of BGLC is equivalent to a proton concentration of 3 mol% (Figure 3.5 b)). BGLC was also tested for hydration in air like condition (pO_2 = 0.2 atm), where the proton concentration was at 0.6 mol% at 400 °C.

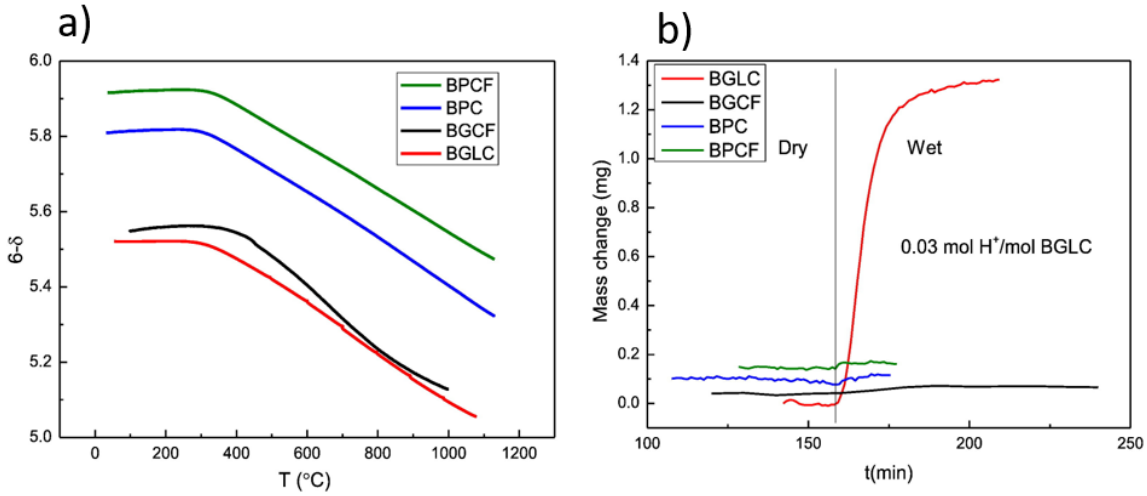

Figure 3.5 a) Oxygen non-stoichiometry vs T for the samples tested in air. b) Mass changes for the powder after isothermal switch at 400 °C and $pO_2 = 4 \cdot 10^{-4}$ atm with a switch from $pH_2O = 3 \cdot 10^{-5}$ atm to pH_2O = 0.02 atm [7].

Electrochemical measurements revealed that BGLC82 on BCZY72 electrolyte has the lowest polarisation resistance of the double perovskite electrodes. BGLC exhibited a polarisation

resistance as low as 0.046 Ωcm^{-2} at 700 ℃ and 10 Ωcm^{-2} at 350 ℃, where the activation energies measured at 700 ℃ and 350 ℃ were around 1.3 eV and 0.5 eV, respectively.

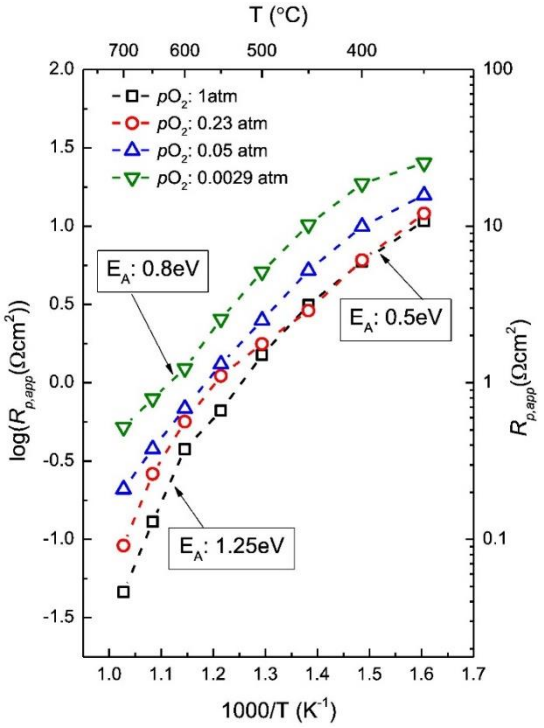

Figure 3.6 The total polarization resistance of BGLC vs. 1000/T for various pO_2 and pH_2O = 0.025 [7].

So far BGLC has exhibited the lowest polarisation resistance reported under water-rich atmosphere on BCZY72 electrolyte together with an electronic conductivity greater than 800 Scm^{-1} [4, 13, 70]

Further work has been conducted by M.K Pedersen [71] where the BGLC positrode were placed on top of a BZCY72 electrolyte pellet. The work showed that BGLC experiences bulk proton conductivity at low temperatures. From this study, a reaction model for the processes that occur in BGLC was developed and their dependencies established, as shown in Table 3.1.

Table 3.1 Reaction model for BGLC as positrode with bulk diffusion of protons. The *m* and *n* are the oxygen and water vapour dependency, respectively, if the reaction is rate-determining [71].

Step	Elementary reaction	Process	*m*	*n*
1	$O_2(g) + 2^*_{BGLC} \leftrightarrow 2O_{BGLC(ads)}$	Exchange of oxygen gas	1	0
2	$O_{BGLC(ad)} + 2e^- \leftrightarrow O^{2-}_{BGLC(ads)}$	Electron transfer	½	0
3	$H^+_{BZCY} \leftrightarrow H^+_{BGLC(bulk)}$	Charge transfer	0	¼
3a	$H^+_{BGLC(bulk)} \leftrightarrow H^+_{BGLC(surf)}$	Bulk diffusion of protons	--	--
4	$O^{2-}_{BGLC(ads)} + H^+_{BGLC(surf)} \leftrightarrow OH^-_{BGLC(ads)}$	Proton exchange	¼	½
5	$OH^-_{BGLC(ads)} + H^+_{BGLC(surf)} \leftrightarrow H_2O_{BGLC(ads)}$	Water formation/split	0	1
6	$H_2O_{BGLC(ads)} \leftrightarrow H_2O\ (g) + {}^*_{BGLC}$	Exchange of water vapour	0	1
Total reaction: $O_2(g) + 2^*_{BGLC} + 4e^- + 4H^+ \leftrightarrow 2H_2O\ (g) + 2^*_{BGLC}$				

Nevertheless, BGLC has been observed to segregate into two phases under 1.5 atm of steam and at 600 °C to $BaCoO_3$ and $Ba_{1-x}Gd_{0.8}La_{0.2+x}Co_2O_{6-\delta}$ [70], and M.K Pedersen's study experienced seconde phases of Co oxides at the surface [71]. Hence, the stability of BGLC might be questionable under operating conditions.

4 Experimental

In this chapter, the experimental methods and equipment used for this work are described.

4.1 Sample Preparation

4.1.1 Electrode materials

The double-perovskites $BaGd_{0.8}La_{0.2}Co_{1.8}Zn_{0.2}O_{6-\delta}$ (BGLC82: Zn), $BaGd_{0.8}La_{0.2}Co_{1.8}Ti_{0.2}O_{6-\delta}$ (BGLC82: Ti) and $BaGd_{0.8}La_{0.2}Co_{1.8}Zr_{0.2}O_{6-\delta}$ (BGCL82: Zr) were synthesised by solid-state reaction with the precursors in the table below. The stoichiometric quantities of each precursor powder were weighed and mixed.

Table 4.1 The different precursors used for the solid-state reaction synthesis.

Precursor	Purity	Supplier
$BaCO_3$	99.8 %	Alfa Aesar
Gd_2O_3	99.9 %	Alfa Aesar
La_2O_3	99.9 %	Aldrich
Co_3O_4	99.7 %	Alfa Aesar
ZnO	99.99%	Aldrich
TiO_2	97 %	Aldrich
ZrO_2	99.99%	Aldrich

Due to possible hydration of Gd_2O_3 and La_2O_3, the powders were dried at 900 ℃ for 5 h and then cooled down fast from 600 ℃ to room temperature to ensure the right stoichiometric amount. After Gd_2O_3 and La_2O_3 were dried, all the precursors were mixed and crushed in an agate mortar. The mixed powder was then calcined in an alumina crucible at 1100 ℃ for 48 h

with a ramp rate of 150 ℃/h for heating and cooling. The calcined powder was then grinded and calcined on more time.

The double–perovskite BGLC82: Zr was also synthesised by the sol-gel method with the precursors in the table below. The stoichiometric quantities of each precursor powder were weighed.

Table 4.2 The different precursors used for the sol-gel synthesis.

Precursor	**Purity**	**Supplier**
$BaCO_3$	99.8 %	Alfa Aesar
$Gd(NO_3)_3 \cdot 6H_2O$	99.99 %	Aldrich
$La(NO_3)_3 \cdot 6H_2O$	98 %	Fluka
$Co(NO_3)_2 \cdot 6H_2O$	99 %	Sigma- Aldrich
$Zn(NO_3)_2 \cdot 6H_2O$	99 %	Sigma- Aldrich
$ZrO(NO_3)_2 \cdot XH_2O$	99 %	Aldrich[I]

Citric acid was used as a solvent and the amount of citric acid was 1:1 mol with mol cations. The respective amount of citric acid was diluted with water before $BaCO_3$ was added to the solution. When all the $BaCO_3$ was dissolved, the rest of the precursors were added to the solution. This gave a clear purple solution. The water was boiled off, the solution formed a gel, and it was placed in a heating cabinet at 250 ℃. The solution was left in the heating cabinet for 30 min for the combustion reaction to happen. The powder was then grinded and fired at 400 ℃ for 1 h with a ramp rate of 300 ℃/h. Then the powder was grinded and calcined for 5 h at 1100 ℃ with a ramp rate of 250 ℃/h.

All powders were characterised by SEM and XRD after calcination. The calcined powders were pressed to pellets with a diameter of 6 mm and a thickness between 1.0-2.8 mm by uniaxial

[I] The molar mass given by the producer was 231.23 g/mol.

cold-pressing at approximate 2 ton in a hydraulic press Specac GS15011. The pellets were sintered at 1200 °C for 24 h with a ramp rate of 100 °C/h.

The sintered pellets were weighed and measured before they were characterised with SEM and XRD.

4.1.2 Electrolyte sample

The supporting electrolyte was $BaZr_{0.7}Ce_{0.2}Y_{0.1}O_3$ (BZCY72) from Cerpotech. The powders were ball milled at 250 rpm for 20 min in isopropanol, and then dried in a heating cabinet for 3-5 hours. The dried powders were pressed to pellets with a diameter of 25 mm and height of ca. 1.7 mm. Sacrificial powder was used to prevent the pellets from being in contact with the alumina crucible and contamination. The pellets were stacked on top of each other to prevent bending when sintering and sacrificial powder was used between the pellets.

The pellets were sintered at 1600 °C for 15 h with a ramp rate at 200 °C/h. They were weighed and measured before characterised with SEM and XRD.

Table 4.3 Electrolyte pellets dimensions and relative density (RD %). The numbering refers to the placement in the stack while sintering, where I was the upper pellet.

Sample	Temp (°C)	M_a (g)	H_a (mm)	D_a (mm)	RD %
BZCY72 I	1600	1.645	1.37	18.23	76,07
BZCY72 II	1600	1.651	1.37	18.34	75,44
BZCY72 III	1600	1.309	1.17	18.22	70,96
BZCY72 IV	1600	1.623	1.53	18.18	67,58

Pt contacts and surface polishing

After the pellets were sintered, they were painted with their Pt contact points. The pellets were painted with three layers of M-001511 PLATINUM INK (Pt-ink) from METALOR. The ink was first dried at 150 °C for 10 minutes before being sintered at 900 °C for 20 min. For the BGLC samples, the contact points were painted on one of the flat surfaces of the pellet. For the

BZCY72 samples, the counter electrode was painted on first by masking an outcut of a circle with tape. Accordingly, the reference electrode was painted on the edge at the same side as the counter electrode, without connecting with the counter electrode.

Thereafter, the electrodes and electrolyte surfaces on the opposite side of the painted contacts were grinded and polished to a mirror-like surface. This was performed to obtain the best possible contact between the electrode and electrolyte. The surface polishing was done with a Multiprep^{TM} from Allied High Tech Products, with grinding paper down to 3μ.

4.2 Sample Characterisation

4.2.1 Scanning Electron Microscopy (SEM)

For the study of the cross-section, phase composition and surfaces of each sample, a FEI-SEM (FEI Quanta 200 FEG-ESEM) with a field emission gun (FEG) was used. The microscope was operated under high-vacuum (10^{-5} Pa) with acceleration voltages of 15-25 kV. Elemental spot analysis was conducted by using an Energy Dispersive X-Ray Spectroscopy (EDS) Pegasus 2200 EDS detector coupled to the SEM.

4.2.2 X-Ray Diffraction (XRD)

The crystal structure and phase composition of all the samples were studied by XRD on a Bruker AXS D8 Discover with $CuK_{\alpha 1}$ λ = 1.54060 Å and $CuK_{\alpha 2}$ λ = 1.54439 Å radiation. The samples were scanned in the range 10° to 70° (2θ) with a step size of 0.02 °/s. The diffractograms were analysed in DIFFRAC.EVA v4.3 by comparing tHem to the Powder Diffraction File database from the International Centre for Diffraction Data and BGLC82 without dopants.

4.2.3 Thermogravimetric Analysis (TGA)

TGA was employed to study the properties of hydration OF the materials. The measurements were carried out in a STA 499 F1 Jupiter, where powder samples of each material were analysed. The powder samples were contained in alumina crucibles and placed on the sample carrier for the TGA. The atmosphere in the TGA was controlled by the TGA gas controller and a gas mixer with the ability to shift from dry to wet atmosphere and H_2O to D_2O shift. The

measurements were conducted in synthetic air (80% /20%, N_2/O_2), where the samples were heated to 900 ℃ FOR 10 min with a ramp rate of 5 ℃/min before cooled to measurement temperature with a ramp rate of 1 ℃/min. The desired temperatures for analysis were 300 ℃, 400 ℃ and 500 ℃. The samples were left in dry conditions at the desired temperature for no less than 8 h to ensure equilibrium in oxygen stoichiometry. The atmosphere was then switched from dry to wet conditions ($pH_2O \approx 0.025$ atm) and then switched from H_2O to D_2O. Before each shift, the conditions were held constant until the scale had stayed at equilibrium for a minimum of 45 minutes.

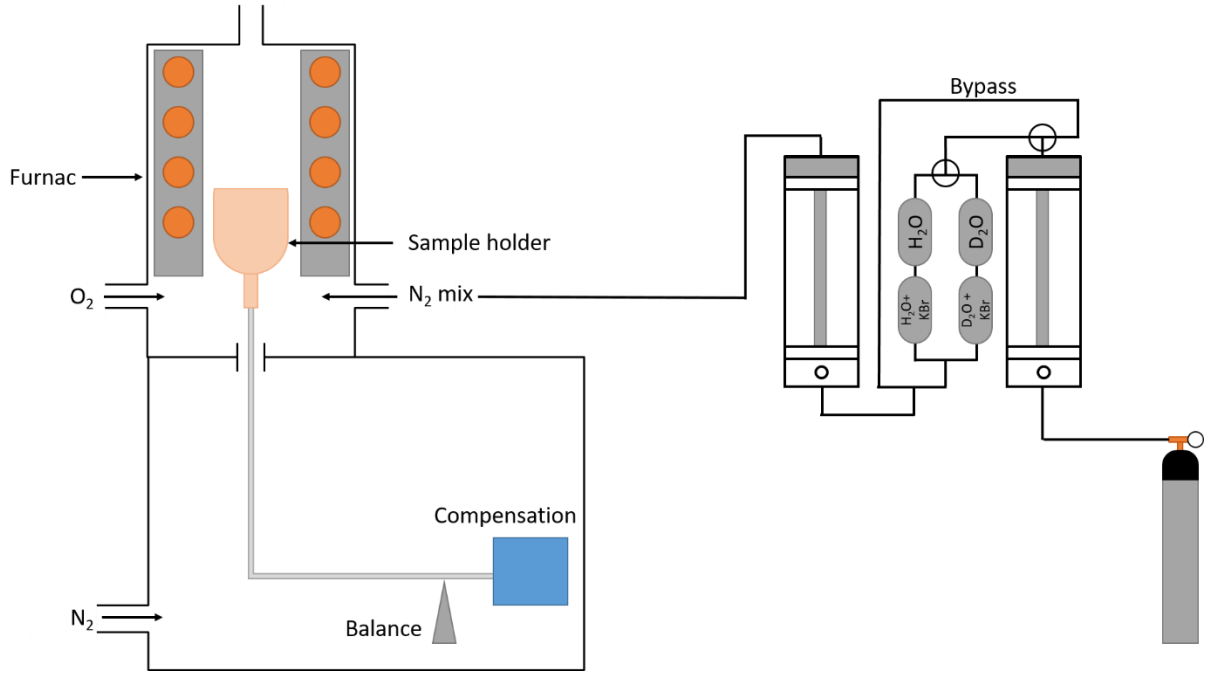

Figure 4.1 Overview over a TGA measurement setup.

4.3 Electrochemical Measurements

The electrochemical measurements were performed with a Gamry Reference 3000 instrument. Potentistatic EIS measurements were performed with an AC amplitude of 30-70 mV, over a frequency of 1 MHz to 0.01 Hz. The temperature was decreased from 650 ℃ to 350 ℃ with 50 ℃ steps.

4.3.1 Instrumental Setup

Measurement Cell

All the electrochemical measurements were carried out in a ProboStat^{TM} measuring cell by NorECs AS. The ProboStat^{TM} comes with electrode and thermocouple feed-throughs and two gas in- and outlets for inner and outer chambers, as shown in Figure 4.2.

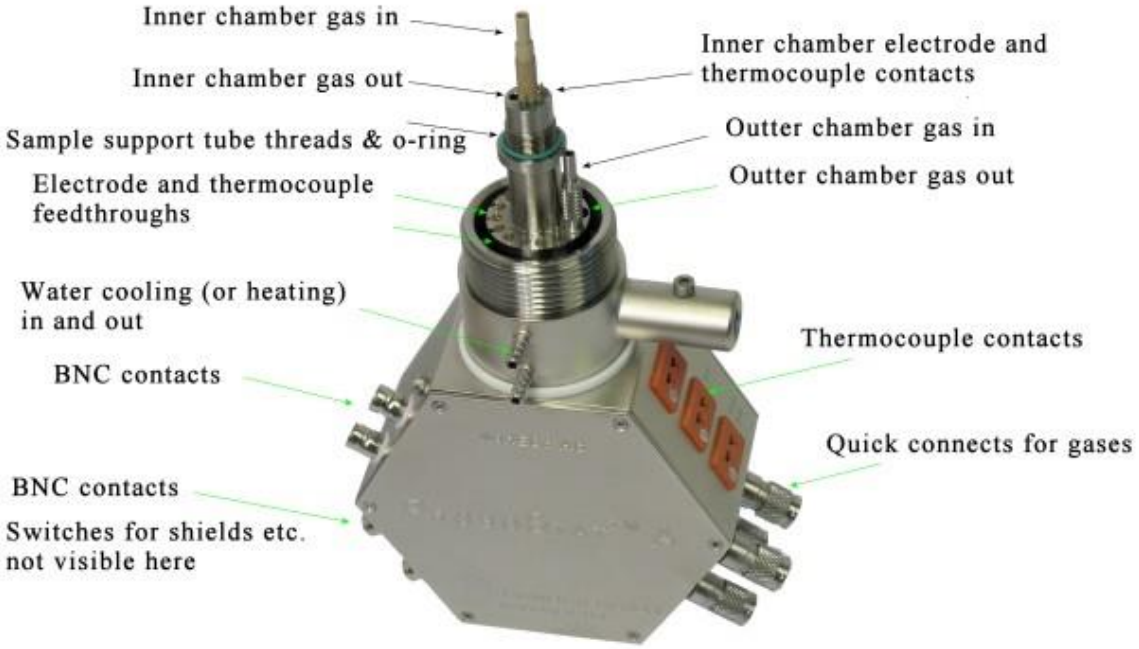

Figure 4.2 Example of a ProboStat^{TM} measuring cell, with a description of the main component [72].

Electrode Setup

A modified point-contact three-electrode four-probe setup with a circular planar geometry was used for the electrochemical measurement as can be seen inthe Figure below.

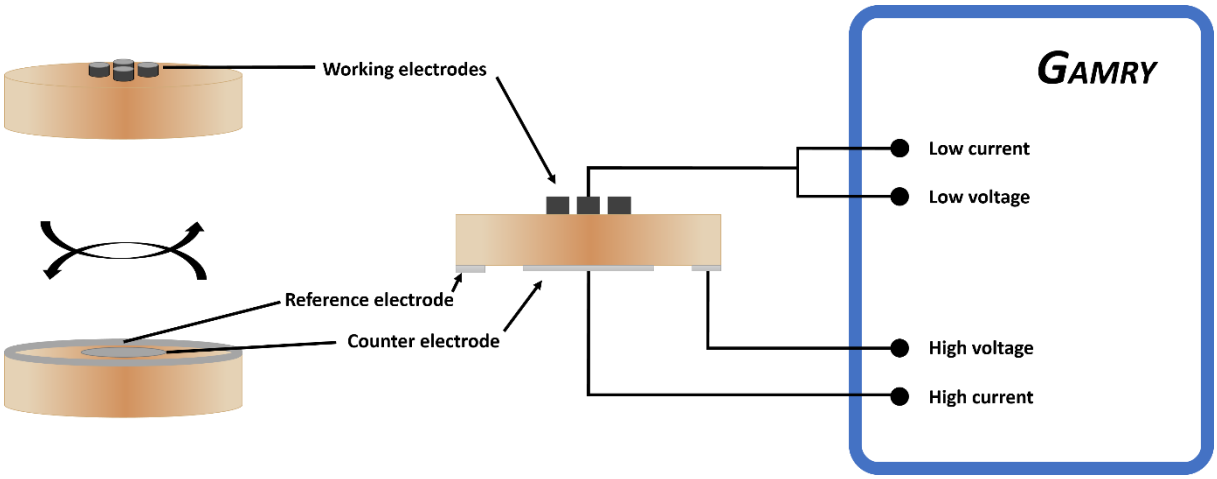

Figure 4.3 Illustration of the measurement cell connected to the Gamry.

The counter electrode (CE) and the reference electrode (FE) are located on the opposite side of the working electrodes (WE). The WE's was placed over the counter electrode to limit the overall current. Every WE was connected to BNC contacts at the ProboStat™ with Pt wires, which made it possible to measure on the samples separately.

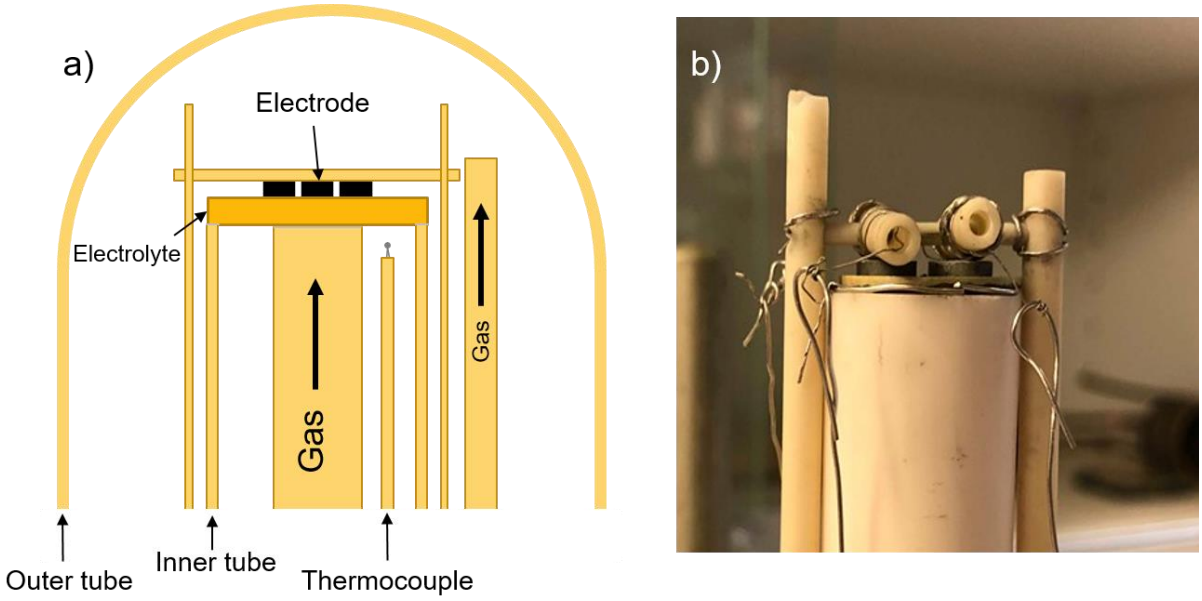

Figure 4.4 a) Illustration of the measurement cell inside the outer tube to the ProboStat™, were b) is a real image of the cell placed on the alumina tubing.

Gas Mixer

In order to obtain the desired atmosphere inside the measurement cell, the pO_2 was controlled by mixtures of O_2 and Ar of different ratios. For the pH_2O, synthetic air was used, and the partial pressure was controlled by passing the gas stream through a saturated solution of potassium bromide at room temperature, which provided a $pH_2O \approx 0.027$ atm, approximately. The different gas mixtures were obtained by an in-house built gas mixer containing a series of flow meters connected by Cu-tubing.

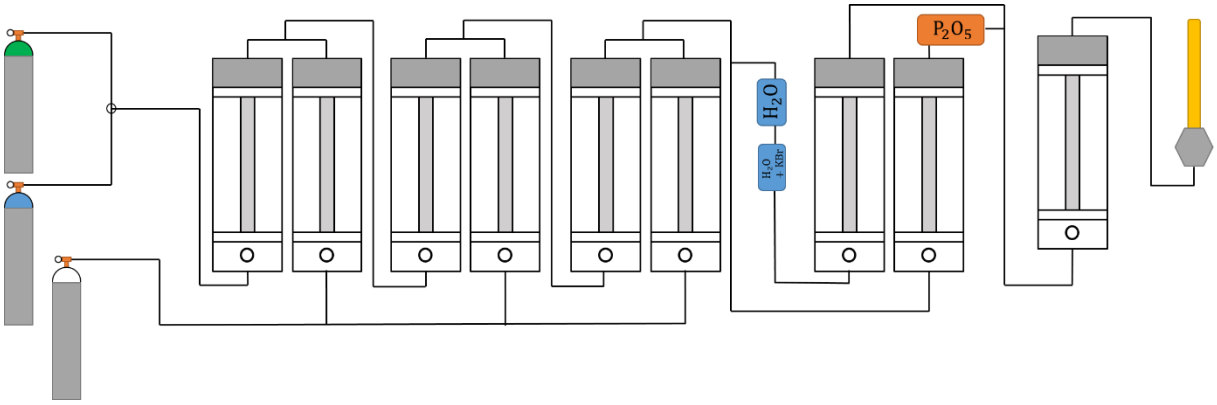

Figure 4.5 Schematics of the gas mixer and the ProboStat™

4.3.2 Measurement Series

Partial pressures of oxygen and water vapour were adjusted systematically; pO_2 of 0.0005, 0.003, 0.01, 0.25 and 0.97 atm, and pH_2O of 0.0005, 0.001, 0.003, 0.01 and 0.027 atm were measured at each temperature step. Every pO_2 dependency was measured with a pH_2O of 0.027 atm. For every change in either temperature or partial pressures, the system was relaxed in the preferred conditions for 1 hour to reach equilibrium, and a single frequency measurement was conducted to ensure equilibrium had been reached.

4.4 Data Analysis

4.4.1 Deconvolution

The impedance data were deconvoluted by using the analysis software ZView® v3.5e by Scribner Associates, Inc.. Three semi-circles were observed in the Nyquist diagram, each was

assigned to a particular contribution from the system. The first semi-circle is found in the high frequencies (HF) and corresponds to the electrolyte bulk resistance. The second and third semi-circles correspond to the responses from the electrode and can be found in the mid- (MF) and low frequencies (LF) area. The MF semi-circle corresponds to charge transfer resistance and double-layer capacitance, while the LF semi-circle corresponds to the mass transfer resistance and capacitance. The EIS spectra were fitted using an equivalent circuit based on a Randles type circuit, showed in Figure 2.12.

4.5 Electrochemical Analysis

The data from the deconvolution were collected in a spreadsheet in Origin. Temperature, pO_2, pH_2O dependencies of the bulk, the charge and the mass transfer resistance with their corresponding capacitances were plotted in logarithmic scale to analyse trends. The activation energies and pre-exponential values were determined through Arrhenius plots. Linear regression was used to obtain the dependencies, activation energy and pre-exponential values.

4.6 Error and Uncertainty

Errors and uncertainties associated with experimental work are impossible to avoid. Therefore, it is essential to identify as many sources of errors as possible to avoid or minimise them. Characterisation methods, like XRD and SEM, have well documented systematic errors and will therefore not be discussed further.

First, during sample preparation, a small number of impurities must be considered regardless of thorough cleaning of the equipment before use. Moreover, uncertainties may occur during weighing due to the uncertainty of the analytical balance of ± 0.2 mg. Regarding the TGA measurements, the thermos balance used has an uncertainty of ± 5 μg.

For the SSR synthesis, the powders need to be evenly mixed to obtain the right stoichiometry and to reduce the forming of secondary phases. The precursors can also be a source of error, as some powders are hygroscopic (La_2O3 and Gd_2O_3), which can lead to under stoichiometry. To preventing under stoichiometric, the powders were dried before use, as mention earlier. When sintering pellets, contamination may occur due to reaction with the crucible in use, and sacrificial powder are used to minimise the uncertainty. During electrochemical measurements,

the gas mixer and the ProboStat^{TM} may be sources of several errors, including gas leakages. From the manual, it is expected a certain pH_2O is present after passing the drying stage of < $1 \cdot 10^{-6}$ atm. However, due to leakages in the system, Kofstad and Norby estimated it to be around $3 \cdot 10^{-5}$ atm[73]. Additionally, each flow meter has an accuracy of ± 5 %, which leads to an increase of uncertainty with the increases of flow meters used in the gas mixer. The thermocouples that were used in furnaces, TGA and measurement cell have an uncertainty of ±1-2 K, depending on their age and degree of contamination. For the TGA and measurement cell, the thermocouples were placed close to the sample without interfering with the sample, to minimise the temperature gradient. For the furnace, the crucible was placed in the middle of the furnace to counteract the temperature gradient best as possible.

Solid-state systems suffer from much higher resistances in the solid electrolyte, which may lead to uncertainties . The placement of the RE and CE on the electrolyte can cause inaccuracy and misleading results if incorrectly placed. For the RE, it should be placed such that the equipotential lines do not change position when measuring from high to low frequencies. Therefore, the RE is painted as a circle around the electrolyte. The CE should be symmetrically aligned with the WE[74].

When studying sample composition with EDS, it is important to know that it is a semi-quantitative technique and therefore only be used as an estimate. The uncertainty that's reported to EDS is 1-2 atomic mole per cent.

5 Results

In this section, all the research findings are presented. The characterisation results of the samples through SEM, EDX and XRD are introduced, along with TGA hydration analises of BGLC82: Ti and BGLC82: Zn. The following section is designated to the outcomes from the electrochemical measurements carried out.

Unfortunately, the temperature measurement was not done continuously from high temperature, but rather at every 100 ℃ steps (600 – 350 ℃) and then for every 50 ℃ steps (650 – 450 ℃), which has resulted in some uncertainties in the results.

5.1 Characterisation

Before the electrochemical measurement, the microstructure and composition of the samples were examined, together with the density of each sintered pellet. The electrode and electrolyte pellet should be as dense as possible to obtain better control of the geometric and contact area.

5.1.1 Microstructure and Elemental Characterisation

The microstructure of the electrodes powder was analysed through SEM, and for elemental characterisation, EDX was used.

Table 5.1 EDX result given in atomic % (At%) the electrode materials.

Element	Theoretical (At%)	BGLC82: Ti (At%) X= Ti	BGLC82: Zn (At%) X= Zn	BGLC82: Zr SSR (At%) X= Zr	BGLC82: Zr SG (At%) X= Zr
Ba	25	22	25	25	24
Gd	20	21	22	22	21
La	5	4.2	5.9	4.8	6.6
Co	45	47	44	44	43
X	5	6.3	4.1	4.7	5.1

5.1.2 Crystal Structure

Diffractograms of the sintered pellets were obtained from XRD at room temperature. The diffractograms of each sample were compared to undoped BGLC82 and the Powder Diffraction File database of the International Centre for Diffraction Data for the second phase that appear for the Zr doped electrodes.

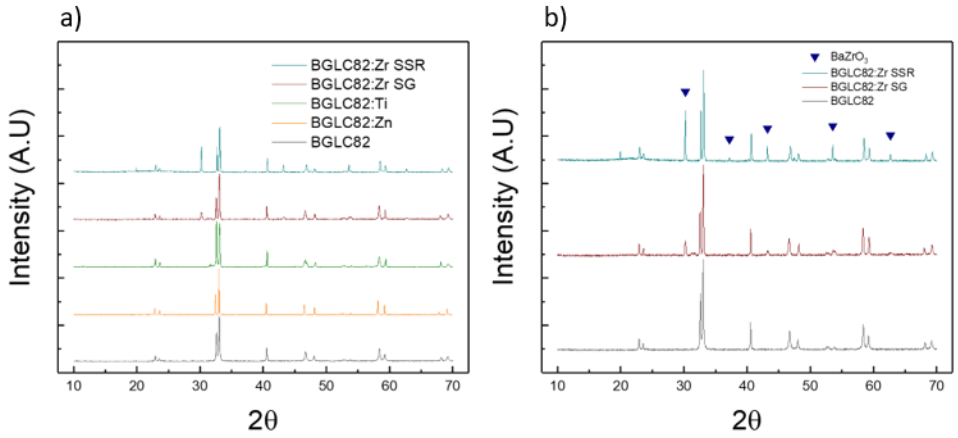

Figure 5.1 XRD of the electrode material, where a) is the electrode materials compared to BGLC82 and b) shown the two Zr electrodes, which shows $BaZrO_3$ as a second phase.

5.1.3 Hydration

The oxides were tested for hydration at various temperatures and with isotope exchange. However, BGLC82: Zr SSR and Zr SG were not tested for hydration, due to the unknown phase compositions of the oxides.

As explained earlier, oxides start to hydrate when exposed to water-rich atmospheres. Hydration can be observed as weight gain for the oxides, as shown in Figure 5.2. However, when changing the protons with deuterium, the weight gain increases further for some oxides, and the proton uptake can be determined more accurately. The flowing defect reaction occurs when pH_2O/pD_2O shift are exposed for an oxide.

$$D_2O\,(g) + 2OH_O^{\bullet} \rightleftharpoons 2OD_O^{\bullet} + H_2O\,(g) \qquad (5.1)$$

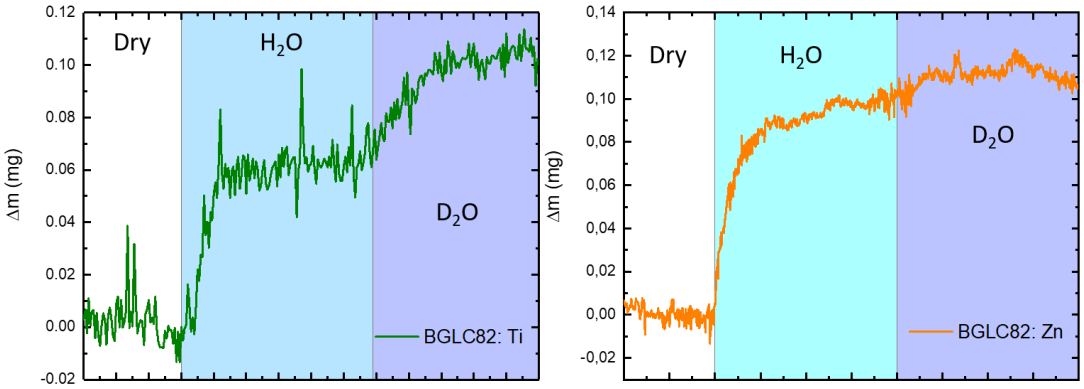

Figure 5.2 TGA measurement of BGLC82: Ti and BGLC82: Zn with atmospheric switches at 300 °C and pO_2 = 0.20. From white to light blue area represents a dry atmosphere to wet atmosphere shift, while light blue to purple represents pH_2O to pD_2O shift.

From Figure 5.2, the weight gain can be extracted and calculated to mol protons. The proton uptake is then represented graphically with a mol % H^+ vs. temperature, as shown in Figure 5.3.

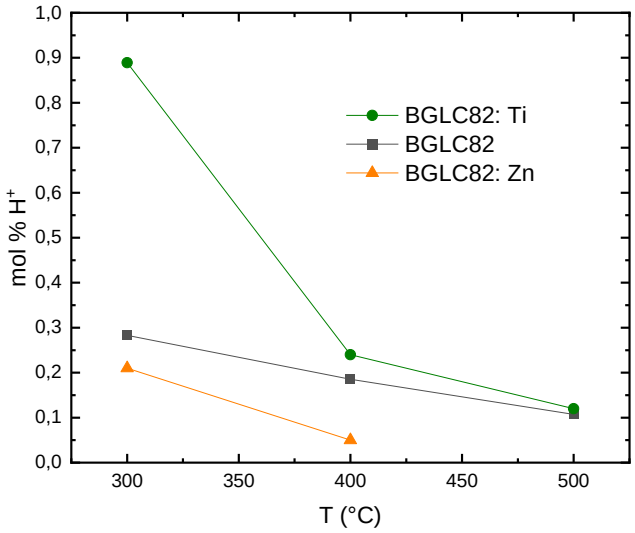

Figure 5.3 Proton concentration vs. T (°C), the measurement was carried out at pO_2 = 0.20 atm and pH_2O = 0.025 atm.[II]

[II] BGLC82 measurment was carried out by Ragnar Strandbakken

5.1.4 Post Electrochemical Characterisation

Electrolyte

After the electrochemical measurements, the electrolyte and electrodes contact surfaces were investigated for interdiffusion. Footprints from the working electrodes on the electrolyte can be seen in Figure 5.4.

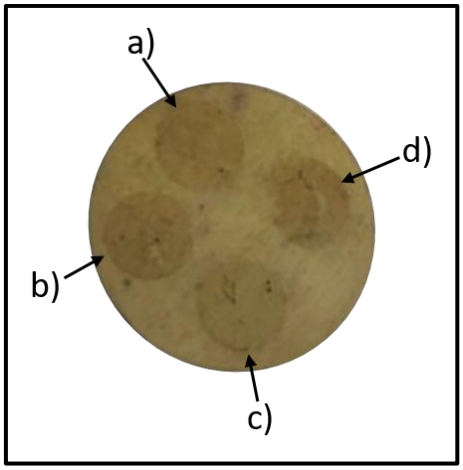

Figure 5.4 Footprint of the working electrodes on the BZCY72 electrolyte after measurements. a) BGLC82: Ti, b) BGLC82: Zr SG, c) BGLC82: Zn and d) BGLC82: Zr SSR left a footprint for each sample.

The footprints were further studied with SEM and EDX. There was no significant change of the electrolyte surface from the footprint areas and the rest of the electrolyte, which can be seen in Figure 5.5.

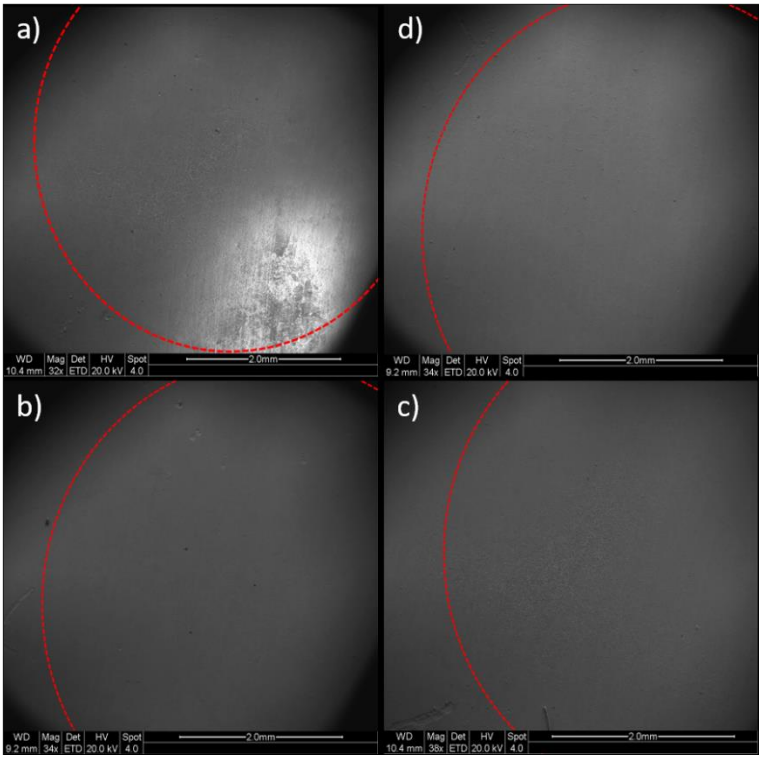

Figure 5.5 SEM images from the used BCZY72 electrolyte. The red dotted circles represent the edge of the footprints. Where a) BGLC82: Ti, b) BGLC82: Zr SG, c) BGLC82: Zn and d) BGLC82: Zr SSR footprints are located in SEM images.

EDS was measured over the footprint areas. To determine diffusion from the working electrodes, Co was used as an indicator, due to its characteristic energy level. The EDS analysis, showed no significant measure of diffusion, as shown in Table 5.2.

Table 5.2 EDS results from the footprint of the BZCY72.

Element	**BGLC82: Ti**	**BGLC82: Zn**	**BGLC82: Zr SG**	**BGLC82: Zr SSR**
Ba (At %)	48	50	48	48
Zr (At %)	34	34	34	35
Ce (At %)	9	9	9	11
Y (At %)	7	7	7	7
Co (At %)	0.6	0.4	1	1

Electrodes

For the positrode pellets, EDS measurements exhibit minor concentration of ZrO on the contact surface of the positrodes, which also can be seen in SEM images as small grain of ZrO.

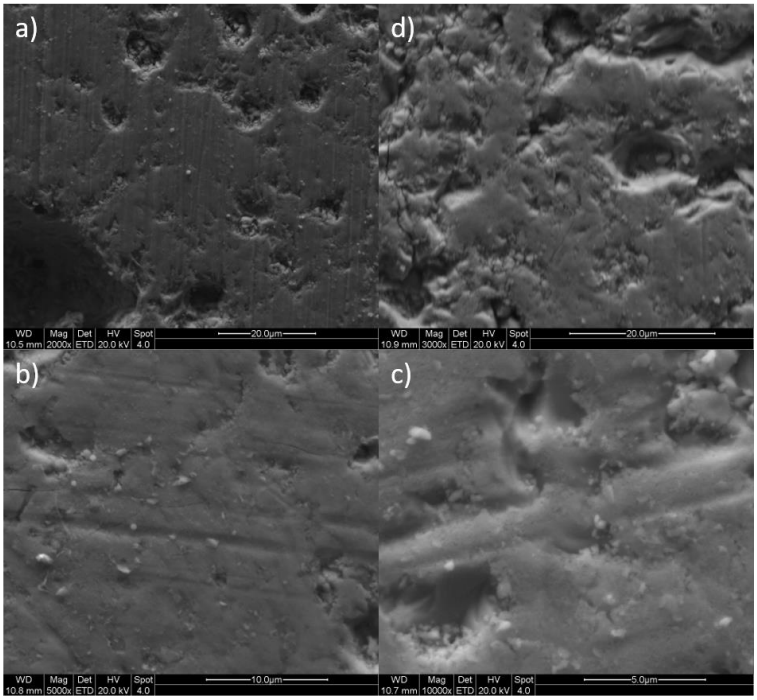

Figure 5.6 The contact surface of the positrode pellets, a) BGLC82 Ti, b) BGLC82: Zr SG c) BGLC82: Zn and d) BGLC82: Zr SSR.

5.2 Electrochemical Characterisation

The EIS measurement was carried out at OCV, with positive and negative bias as a function of temperature and partial pressure of oxygen and water vapour. The impedance spectra provide information about the contributions from the interface, that can be assigned to processes at the interface by deconvolution. The three contributions were assigned to each of the three semi-circles of the impedance measurements, by capacitance and frequency area. By using a Randle type equivalent circuit to deconvolute the measurements, as shown in Figure 5.7, R1 was related to the electrolyte contribution, which yields the ohmic resistance (R_{ohm}) and ohmic capacitance (C_{ohm}), where R2 and R3 were assigned to the electrode polarisation contributions $R_{p,2}$ and $R_{p,3}$, respectively. The respective capacitances for the polarisation contributions were assigned to CPE2 ($C_{p,2}$) and CPE3 ($C_{p,3}$). However, as the high and low-frequency arcs were visible, the

mid-frequency response was more challenging to distinguish, and resulted in a higher uncertainty for the charge transfer contribution.

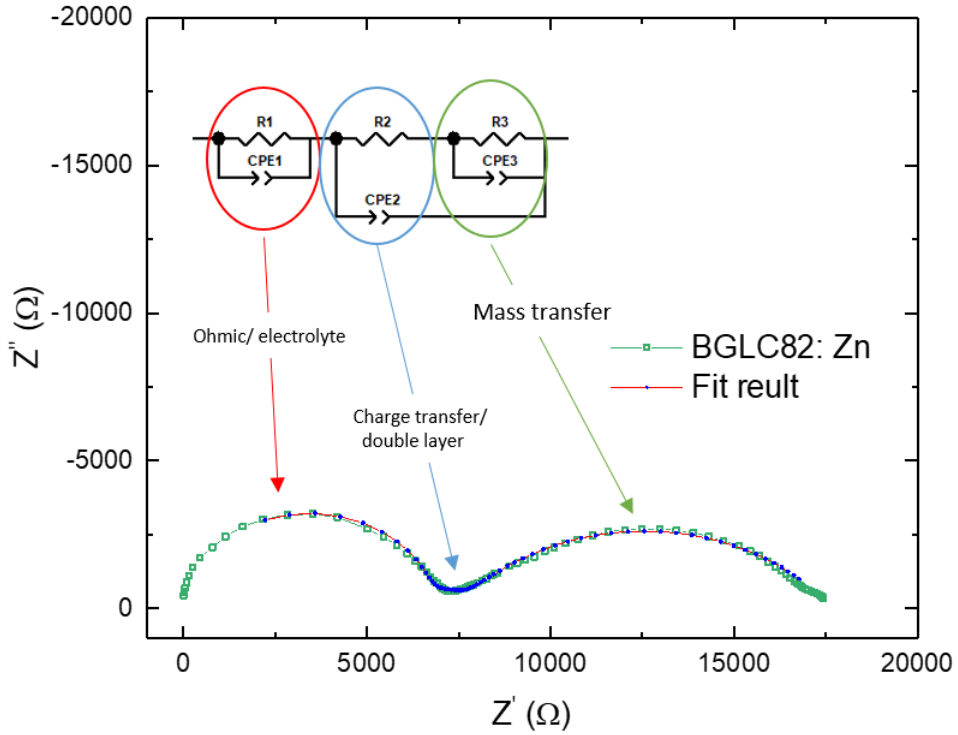

Figure 5.7 EIS spectre of BGLC82: Zn on BZCY72 electrolyte at 500 °C pO_2 = 0.003 atm and pH_2O = 0.025 atm, that was deconvoluted by Randle circuit.

The resistances and capacitances measured at OCV, as a function of T, pO_2 and pH_2O are presented first in this section followed by the bias measurements as a function of T and pH_2O.

5.2.1 Temperature Dependencies

The temperature dependencies for the different contribution, and the different electrodes are presented in Figure 5.8.

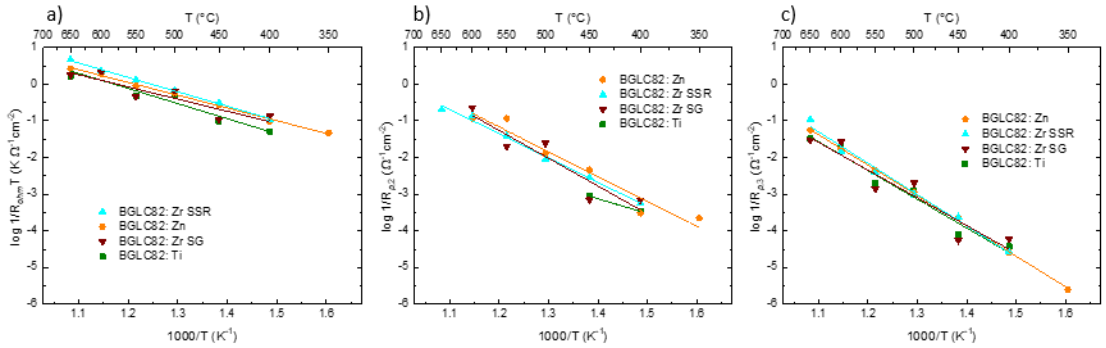

Figure 5.8 Temperature dependency for the different contribution, a) ohmic, b) $R_{p,2}$ and c) $R_{p,3}$, where measurements were carried out at pO_2 = 0.20 atm and pH_2O = 0.025 atm.

The different electrodes show a similar temperature dependency for all the contributions. The $R_{p,2}$ contribution for BGLC82: Ti was only obtained from two temperatures, due to the challenge to distinguish the $R_{p,2}$ and $R_{p,3}$ contributions at higher temperatures. The normalized resistance values of each contribution and electrode at high, intermediate and low temperature are shown in Table 5.3.

Table 5.3 The ohmic and polarisation resistances for the different electrodes on a BZCY72 electrolyte at high, intermediate and low temperatures. The measurements were carried out in pO_2 = 0.20 atm and pH_2O = 0.025 atm.

	T (°C)	R_{ohm} (kΩcm^2)	$R_{p,2}$ (kΩcm^2)	$R_{p,3}$ (kΩcm^2)
	650	0.56	--	0.030
BGLC82: Ti	500	1.5	--	0.80
	400	12	2.9	26
	650	0.35	--	0.019
BGLC82: Zn	500	1.3	0.079	0.89
	400	69	3.3	38

	650	0.20	0.0048	0.0092
BGLC82: Zr SSR	500	1.2	0.11	1.0
	400	61	1.8	37
	650	0.52	--	0.034
BGLC82: Zr SG	500	1.2	0.041	0.49
	400	51	1.4	16

As presented in Table 5.3, the samples exhibit close to the same ohmic resistance with some deviation, which might come from the placement of the samples on the electrolyte.

The respective capacitances for the electrode contributions are shown in Figure 5.9.

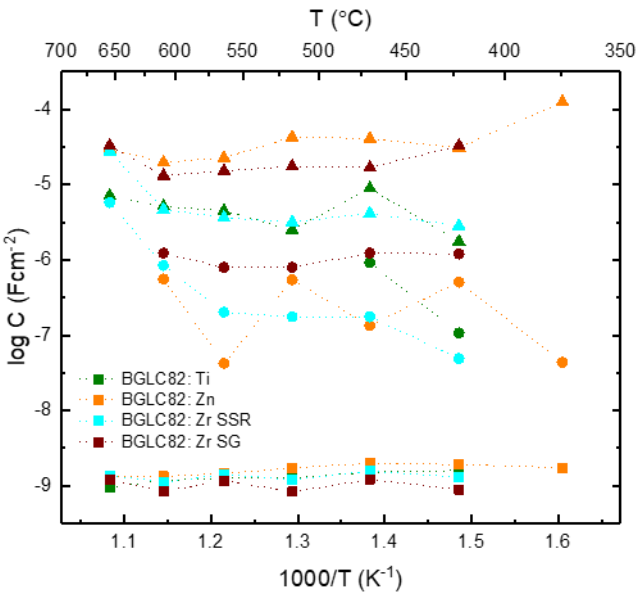

Figure 5.9 Temperature dependencies for the electrodes capacitances, where (■) is from the ohmic contribution, (●) from the $R_{p,2}$ and (▲) for the $R_{p,3}$ with pO_2 = 0.20 atm and pH_2O = 0.025 atm.

From Figure 5.9, the capacitance of the ohmic contribution is in range of ~10^{-10} - 10^{-9} Fcm^{-2}. For the two polarization contributions, the capacitance for $R_{p,2}$ are seen in a range of ~10^{-8} – 10^{-6} Fcm^{-2} and for $R_{p,3}$ ~10^{-6} – 10^{-5} Fcm^{-2}. The capacitance at high, intermediate and low temperature are presented in Table 5.4 for all of the different electrodes.

Table 5.4 Capacitance values for the ohmic (C_{ohm}) and polarization resistances ($C_{p,2}$ and $C_{p,3}$), at high, intermediate and low temperatures. The measurements were carried out in pO_2 = 0.20 atm and pH_2O = 0.025 atm.

	T (°C)	C_{ohm} (Fcm^{-2})	$C_{p,2}$ (Fcm^{-2})	$C_{p,3}$ (Fcm^{-2})
	650	$9.4 \cdot 10^{-10}$	--	$7.0 \cdot 10^{-6}$
BGLC82: Ti	500	$1.3 \cdot 10^{-9}$	--	$2.5 \cdot 10^{-6}$
	400	$1.6 \cdot 10^{-9}$	$1.1 \cdot 10^{-7}$	$1.7 \cdot 10^{-6}$
	650	$1.4 \cdot 10^{-9}$	--	$2.9 \cdot 10^{-5}$
BGLC82: Zn	500	$1.7 \cdot 10^{-9}$	$5.4 \cdot 10^{-7}$	$4.3 \cdot 10^{-5}$
	400	$1.9 \cdot 10^{-9}$	$5.1 \cdot 10^{-7}$	$3.1 \cdot 10^{-5}$
	650	$1.4 \cdot 10^{-9}$	$5.7 \cdot 10^{-6}$	$2.8 \cdot 10^{-5}$
BGLC82: Zr SSR	500	$1.2 \cdot 10^{-9}$	$1.8 \cdot 10^{-7}$	$3.2 \cdot 10^{-6}$
	400	$1.3 \cdot 10^{-9}$	$4.9 \cdot 10^{-8}$	$2.8 \cdot 10^{-6}$
	650	$1.2 \cdot 10^{-9}$	--	$3.3 \cdot 10^{-5}$
BGLC82: Zr SG	500	$8.3 \cdot 10^{-10}$	$7.9 \cdot 10^{-7}$	$1.7 \cdot 10^{-5}$
	400	$8.9 \cdot 10^{-10}$	$1.2 \cdot 10^{-6}$	$3.3 \cdot 10^{-5}$

Activation Energy

The activation energy and pre-exponetional factor (A_o) were determined by linear regression of ln $1/R_{ohm} \cdot T$ vs. $1/T$ for the electrolyte and ln $1/R_p$ vs. $1/T$ for the electrode process by the following expression:

$$\frac{1}{R_p} = A_0 \exp\left(-\frac{E_a}{RT}\right) \tag{3.80}$$

where R_p is the polarisation resistance, R is the gas constant and T is the temperature in Kelvin.

The Arrhenius plots for the three contributions are shown in Figure 5.10 for the different electrodes. The respective information extracted from each Arrhenius plot is shown in Table 5.5.

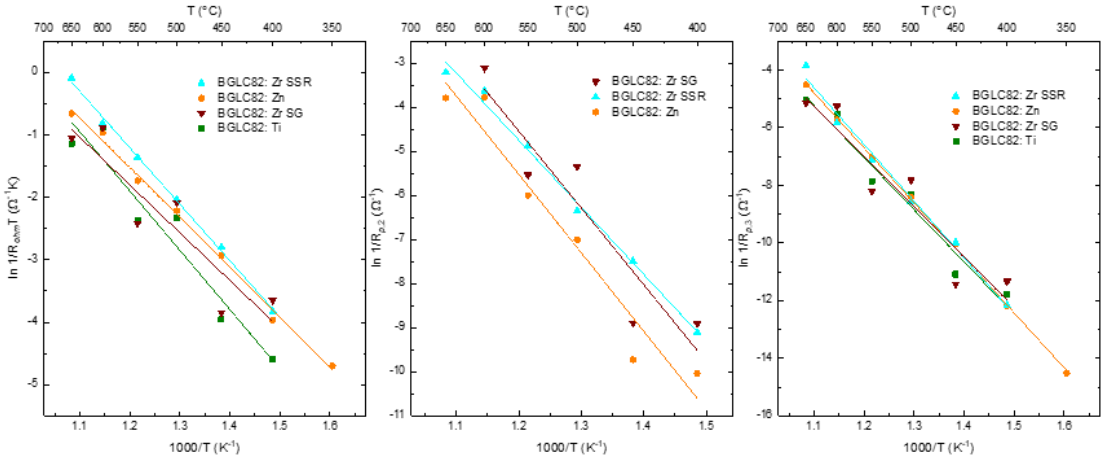

Figure 5.10 Arrhenius plot of a) ohmic b) $R_{p,2}$ and c) $R_{p,3}$ contribution for the various electrodes on a BZCY72 electrolyte at pO_2 = 0.20 and pH_2O = 0.025.

Table 5.5 Activation energies and the pre-exponentials of the three contributions and all the samples.

	Contribution	T (°C)	E_a (eV)	Pre-exponential factor ($\Omega^{-1}cm^{-2}$)
BGLC82: Zn	Ohmic	650 – 350	$0.69 \pm 0.02_1$	$3.2 \cdot 10^3$
	$R_{p,2}$	600 – 350	$1.5 \pm 0.1_8$	$1.8 \cdot 10^6$
	$R_{p,3}$	650 – 350	$1.64 \pm 0.01_9$	$1.0 \cdot 10^7$
BGLC82: Ti	Ohmic	650 – 400	$0.8 \pm 0.1_1$	$1.3 \cdot 10^4$
	$R_{p,3}$	650 – 400	$1.6 \pm 0.1_5$	$2.2 \cdot 10^6$
BGLC82: Zr SSR	Ohmic	650 – 400	$0.77 \pm 0.01_8$	$1.5 \cdot 10^4$
	$R_{p,2}$	650 – 400	$1.31 \pm 0.05_4$	$7.5 \cdot 10^5$
	$R_{p,3}$	650 – 400	$1.69 \pm 0.08_4$	$2.4 \cdot 10^7$
BGLC82: Zr SG	Ohmic	650 – 400	$0.6 \pm 0.1_4$	$1.6 \cdot 10^3$
	$R_{p,2}$	600 – 400	$1.5 \pm 0.3_2$	$1.3 \cdot 10^7$
	$R_{p,3}$	650 – 400	$1.4 \pm 0.2_6$	$1.0 \cdot 10^6$

Since the different electrodes are operating on the same electrolyte, the activation energies of the electrolyte are similar for all cases. The pre-exponential factor depends significantly on geometric factor, the concentration of species and attempt rates.

5.2.2 Partial pressure dependencies

The variation of the partial pressure of oxygen and water vapour for the samples gives essential information about the positrode reaction mechanisms. The effect of varying temperatures might result in changes of dominating charge carriers and their mobilities. The partial pressures changes at canstant temperatures, the concentration of the involved species changes, which provides information about how the positrode reaction occurs. The partial pressure dependencies for all the samples are presented in this section.

pO_2 - Dependency

Oxygen is an essential species for the positrode Reaction 3.2. By varying the partial pressure of the atmosphere, the effect can be studied, which yields information about the different contributions. An example of the EIS measurement is shown in Figure 5.11, where the high and middle-frequency range does not experience enormous changes, compared to the low-frequency range.

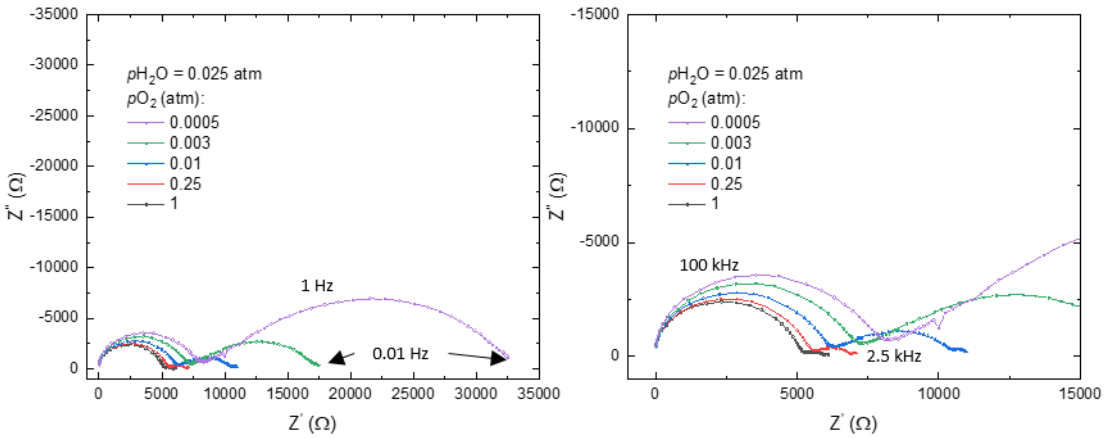

Figure 5.11 EIS measurement of BGLC82: Zn on BZCY72 with various oxygen partial pressures and pH_2O = 0.025 atm at 500 °C.

The resistances and capacitances were distinguished for every experimental matrix by deconvolution. The pO_2 dependencies of ohmic and polarization resistances for BGLC82: Zn are presented in Figure 5.12, and a comparison of the dependency to the polarization resistances between the electrodes of a selected temperature is presented in Figure 5.13. The full dependency plot of the other electrodes are shown in the Appendix (Figure A.2.1). The dependency values are presented in Table 5.6 for all of the electrodes.

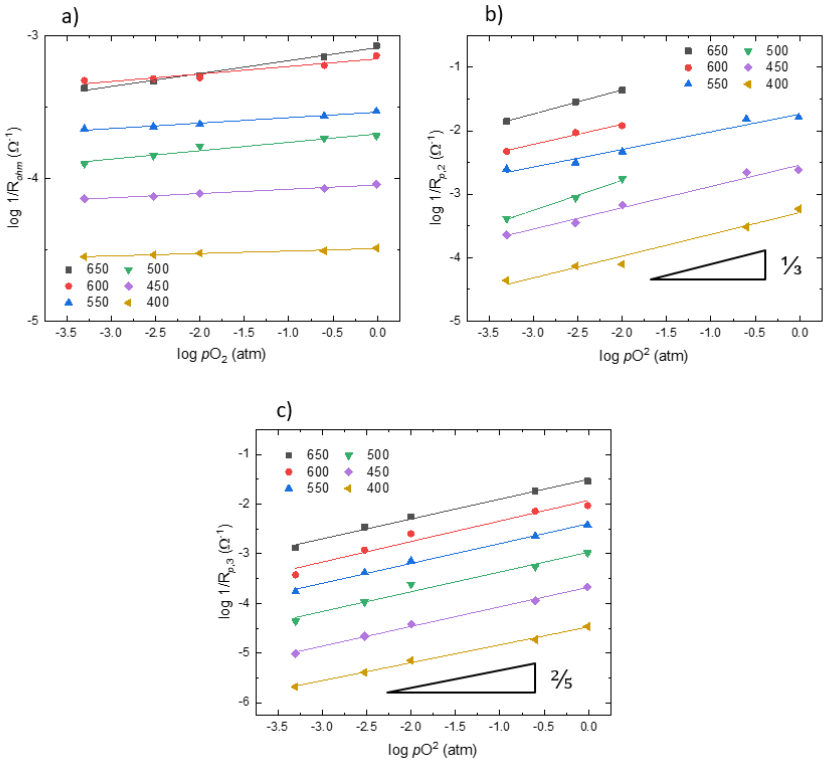

Figure 5.12 pO_2 dependencies for BGLC82: Zn on BZCY72, where the three contribution a) ohmic, b) $R_{p,2}$ and c) $R_{p,3}$ are presented.

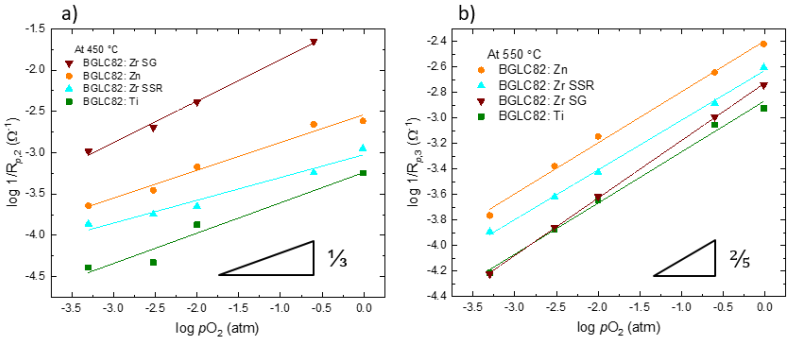

Figure 5.13 pO_2 dependencies for the two polarization resistances, where a) $R_{p,2}$ for the electrodes at 450 °C and b) $R_{p,3}$ for all the electrodes at 550 °C, pH_2O = 0.025 atm for all the measurements.

pH2O- Dependency

Water is the other species of the positrode Reaction 3.2, where the concentration can be changed in the system and information for the contributions can be obtained. An EIS measurement is shown in Figure 5.15, where the low-frequency range shows a change with changes in water vapour pressures.

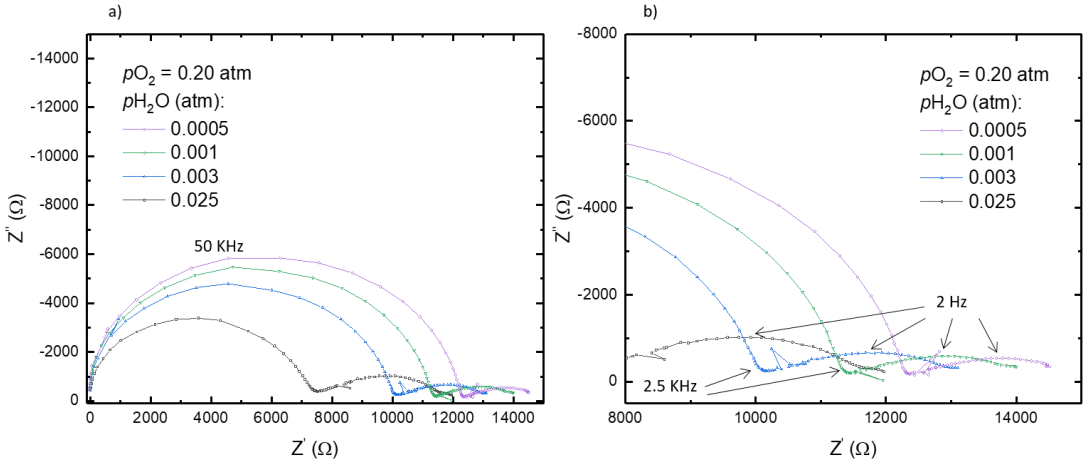

Figure 5.14 Impedance sweep for BGLC82: Zn on a BZCY72 electrolyte at 500 °C with pO_2 = 0.20 and various pH_2O.

The resistances and capacitances were distinguished for every experimental matrix by deconvolution. The pH_2O dependencies of ohmic and polarization resistances for BGLC82: Zn are presented in Figure 5.15, and a comparison of the dependency to the polarization resistances between the electrodes of a selected temperature is presented in Figure 5.16. The full dependency plot for the other electrodes are shown in the Appendix (Figure A.2.2). The dependency values are presented in Table 5.6 for each electrode.

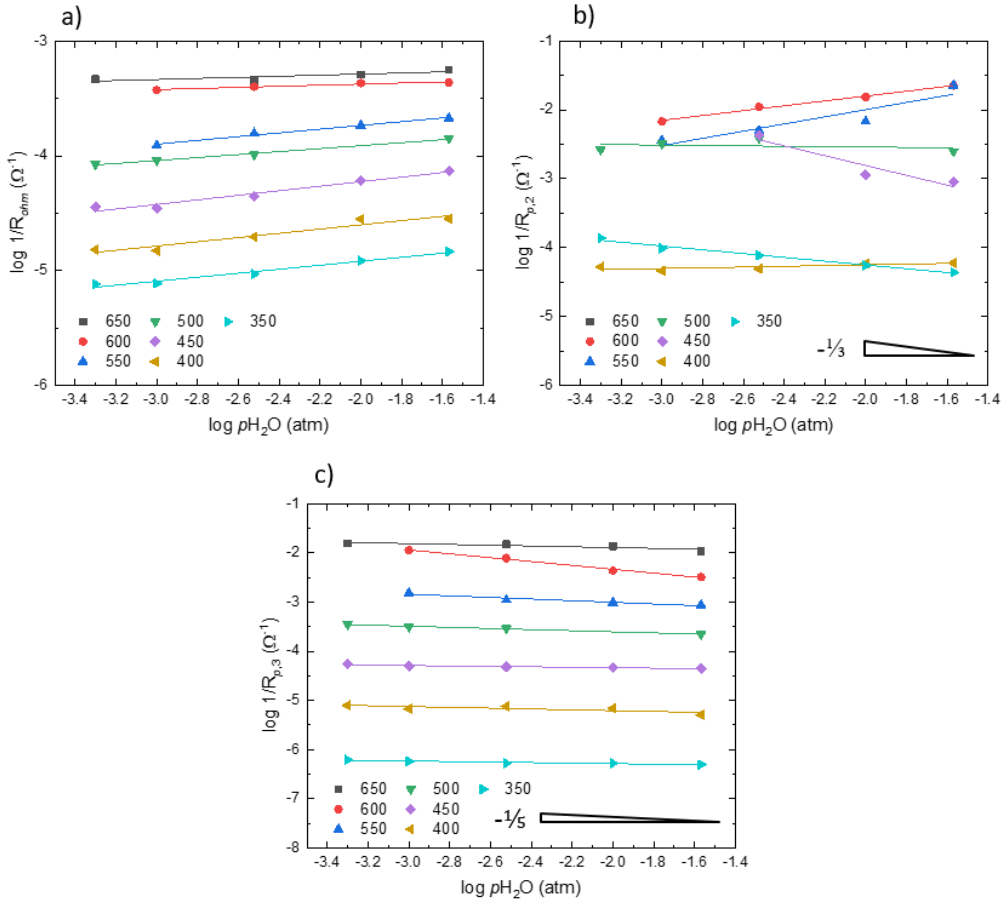

Figure 5.15 pH_2O dependencies for BGLC82: Zn on BZCY72, where the three contributions a) ohmic, b) charge transfer and c) mass transfer are presented.

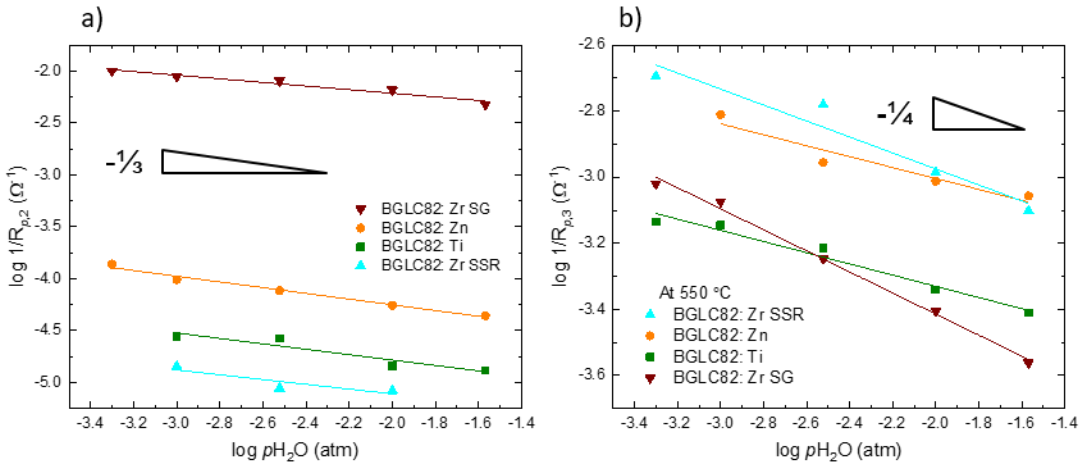

Figure 5.16 pH_2O dependencies for the two polarization resistances, where a) shows $R_{p,2}$ for BGLC82: Zn and Zr SSR are at 350 °C, BGLC82: Ti at 400 °C and BGLC82: Zr SG at 500 °C. b) shows $R_{p,3}$ for all the electrodes at 550 °C, pO_2 = 0.20 atm for all the measurements.

Reaction Orders

The oxygen and water vapour pressure dependencies of the positrode contribution are presented in Table 5.6. The oxygen and water vapour dependencies are represented as m_p and n_p, respectively, by the following formula:

$$\frac{1}{R_p} \propto (pO_2)^{m_p}(pH_2O)^{n_p} \tag{2.81}$$

Table 5.6 The reaction orders $R_{p,2}$ (p,2) and $R_{p,3}$ (p,3) for the different electrodes.

BGLC82: Ti				
T (°C)	$m_{p,2}$	$n_{p,2}$	$m_{p,3}$	$n_{p,3}$
650	--	--	½	-⅓
600	¼	--	⅖	-⅖
550	--	--	⅖	-⅕
500	⅕	--	⅖	-⅓
450	½	-⅕	⅖	-⅕
400	¼	-¼	⅓	-⅕
350	--	--	⅕	--
Avg	⅓	-⅕	⅖	-¼

BGLC82: Zn				
T (°C)	$m_{p,2}$	$n_{p,2}$	$m_{p,3}$	$n_{p,3}$
650	⅖	--	⅖	-1/10
600	⅓	⅖	⅖	-⅖
550	⅓	½	⅖	-⅕
500	½	0	⅖	-1/10
450	⅓	-⅔	⅖	-1/10
400	⅓	1/10	⅖	-1/10
350	--	-⅓	--	1/10
Avg	⅓	0	⅖	-⅕

BGLC82: Zr SSR				
T (°C)	$m_{p,2}$	$n_{p,2}$	$m_{p,3}$	$n_{p,3}$
650	½	-⅓	⅖	-¼
600	¼	-⅖	⅖	-⅓
550	⅓	-½	⅖	-¼
500	--	-⅕	⅖	-⅓
450	⅓	-⅕	⅓	-⅓
400	1/10	-⅖	⅓	-⅕
350	1/10	-¼	⅓	-1/10
Avg	¼	-⅓	⅓	-¼

BGLC82: Zr SG				
T (°C)	$m_{p,2}$	$n_{p,2}$	$m_{p,3}$	$n_{p,3}$
650	--	--	½	-⅓
600	¼	--	⅖	-⅓
550	⅓	-⅘	⅖	-⅓
500	½	-⅕	⅖	-⅕
450	⅕	0	⅖	-⅓
400	¼	-⅕	⅖	-⅕
350	--	--	--	--
Avg	⅓	-⅓	⅖	-¼

5.3 Bias Measurements

When a potential difference from OCV is applied to the EIS measurement, the reaction is either pushed towards the cathodic or anodic reaction rate of the positrode reaction depending on the respective potential. In this work, a negative potential yields a cathodic reaction while a positive potential gives an anodic reaction, which are shown in Reaction 5.2 and 5.3, respectively.

$$4H^+ + 4e^- + O_2\ (g) \overset{k_c}{\rightarrow} 2H_2O\ (g) \tag{5.2}$$

$$4H^+ + 4e^- + O_2\ (g) \overset{k_a}{\leftarrow} 2H_2O\ (g) \tag{5.3}$$

The external potential is hereafter referred to as bias and the cathodic and anodic directions as negative and positive, respectively.

By measuring EIS with bias in either direction separately, the different contribution yield information about the reaction that is occurring, its kinetics and limitations. These measurements will then provide a better understanding of the electrodes behaviour under various operations required for a positrode in a PCEC.

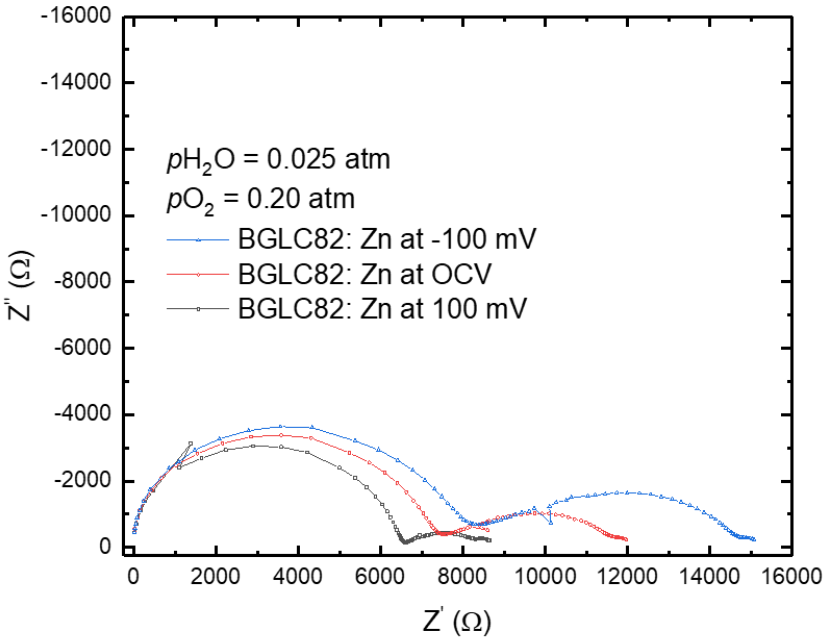

Figure 5.17 The difference in EIS measurements at OCV and bias at both directions for BGLC82: Zn on a BZCY72 electrolyte at 500 °C.

The following section is dedicated to the bias measurement conducted on the different electrodes, with varying temperatures and water vapour pressures. The BGLC82: Zr SG electrode is not included due to lack of obtained data points.

5.3.1 Negative Bias - Cathodic

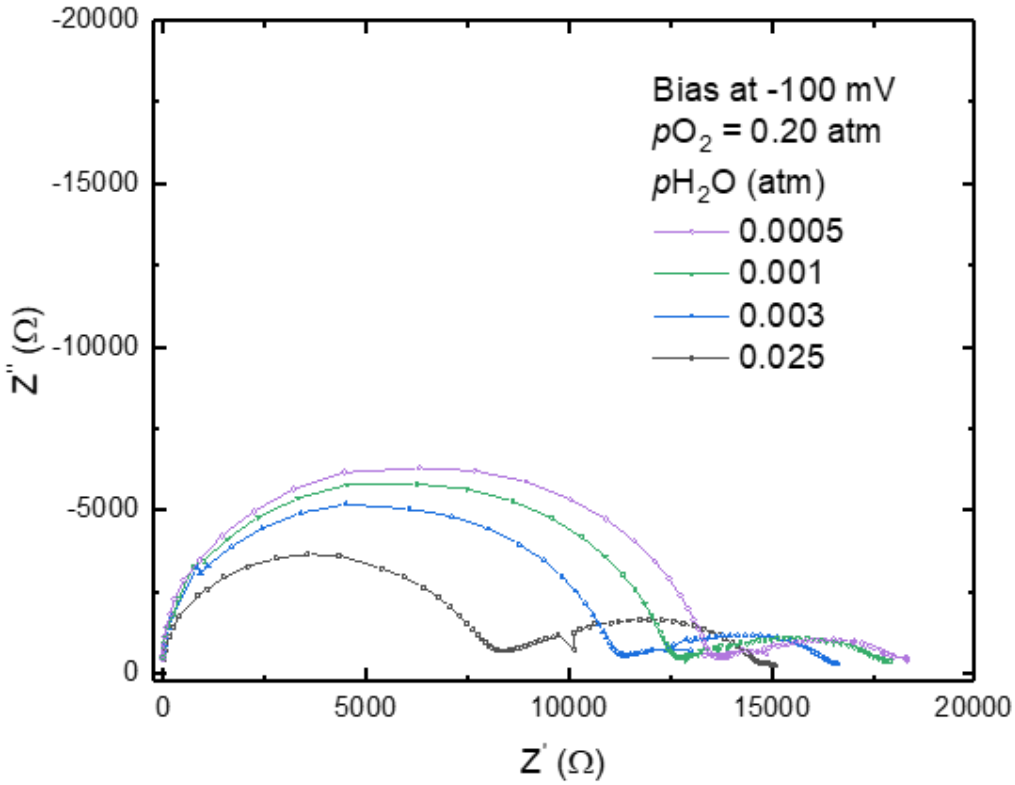

Figure 5.18 Impedance sweep of BGLC82: Zn on BZCY72 electrolyte at 500 °C with various water vapour pressures.

The resistances and capacitances were distinguished for every experimental matrix by deconvolution. The pH_2O dependencies of ohmic and polarization resistances for the different electrodes are shown in the Appendix (Figure A.3.1). The temperature dependencies for the ohmic and polarisation resistances are shown in Figure 5.19, where the values at high, intermediate and low temperatures are presented in the Appendix (Table A.3.1)

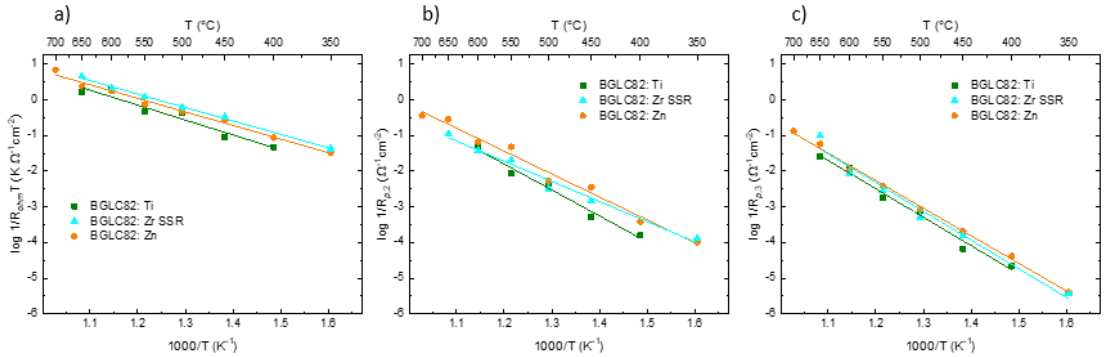

Figure 5.19 Temperature dependencies for the ohmic and polarization resistances, where a) ohmic, b) $R_{p,2}$ and c) $R_{p,3}$, for each of the electrodes.

The respective activation energies and pre-exponentials from Figure 5.19 are shown in the Appendix in Table A.3.3.

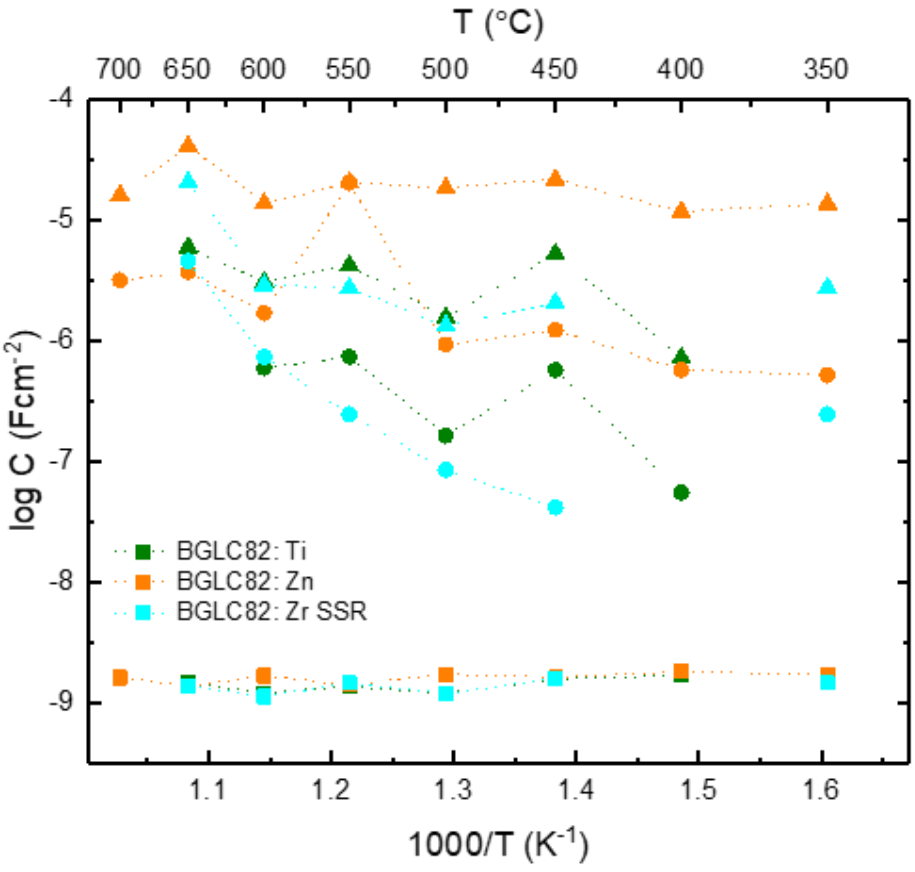

Figure 5.20 Temperature dependencies for the respective capacitance for the resistance contributions, where (■) are related to ohmic, (●) for $R_{p,2}$ and (▲) $R_{p,3}$, for each of the electrodes.

The respective capacitance temperature dependencies are shown in Figure 5.20, whereas the values for high, intermediate and low temperatures are shown in Table A.3.2 in the Appendix. The respective reaction orders for $R_{p,2}$ and $R_{p,3}$ gained from the pH_2O dependencies in Figure A.3.1, are shown in Table 5.7

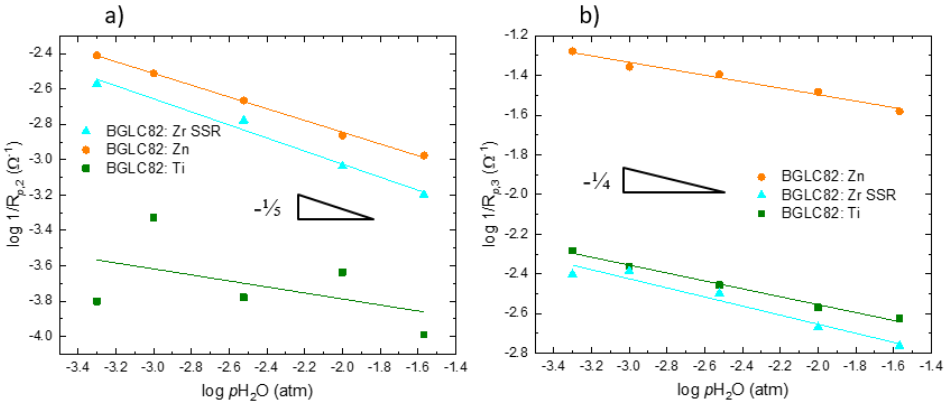

Figure 5.21 pH_2O dependencies comparison between the electrodes and the polarisation resistances a) $R_{p,2}$ at 500 °C for BGLC82: Zn and Zr SSR, and at 450 °C for BGLC82: Ti, and b) $R_{p,3}$ at 600 °C for BGLC82: Ti and Zr SSR, and at 700 °C for BGLC82: Zn. The measurements were carried out at pO_2 = 0.20 atm and with a negative bias at 100 mV.

Table 5.7 The reaction orders $R_{p,2}$ (p,2) and $R_{p,3}$ (p,3) of the different electrodes under negative bias.

	BGLC82: Ti		BGLC82: Zn		BGLC82: Zr SSR	
T (°C)	$n_{p,2}$	$n_{p,3}$	$n_{p,2}$	$n_{p,3}$	$n_{p,2}$	$n_{p,3}$
700	--	--	-1/10	-1/5	--	--
650	--	-1/5	-1/3	-1/10	-1/4	-1/10
600	-1/4	-1/5	-1/2	-1/10	-1/5	-1/4
550	--	-1/10	-1/5	-1/10	-1/3	-1/3
500	-1/2	-1/5	-1/3	0	-1/3	-1/4
450	-1/5	-1/5	-3/5	0	-1/10	-1/4
400	--	-1/5	-1/10	0	-1/10	-1/10
350	--	--	-1/10	-1/10	--	--
Avg	-1/3	-1/5	-1/3	-1/10	-1/5	-1/5

5.3.2 Positive Bias - Anodic

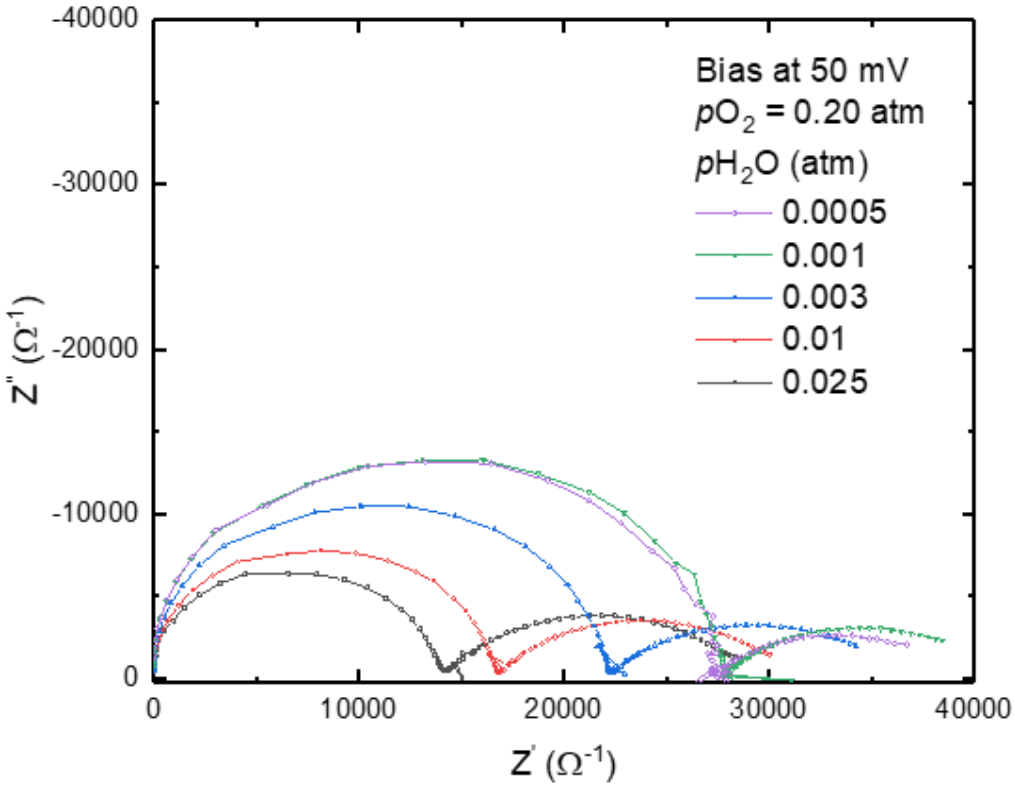

Figure 5.22 Impedance sweep of BGLC82: Zn on BZCY72 electrolyte at 450 °C with various water vapour pressures.

The electrode contributions were extracted from the EIS measurements, similar to what is shown in Figure 5.22. The pH_2O dependencies of the ohmic and polarization resistances are shown in Figure A.4.1 in the Appendix. The temperature dependencies for each of the electrode contributions are shown in Figure 5.23, where the respective values at high, intermediate and low temperatures are present at Table A.4.1 in the Appendix.

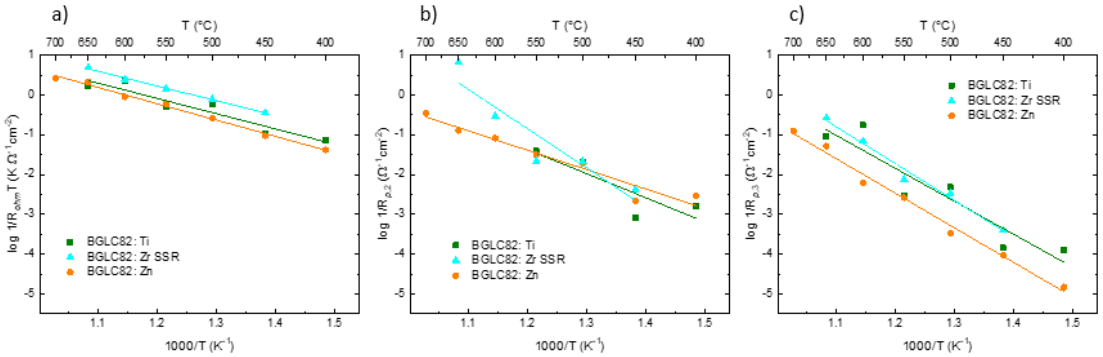

Figure 5.23 Temperature dependencies of the different contributions, a) ohmic, b) $R_{p,2}$ and c) $R_{p,3}$, where measurements were carried out at pO_2 = 0.20 atm, pH_2O = 0.025 atm and with a positive bias of 50-100 mV.

The corresponding activation energies and pre-exponentials of the ohmic and polarisation resistances that are obtained from Figure 5.23 are presented in Table A.4.3 in the Appendix.

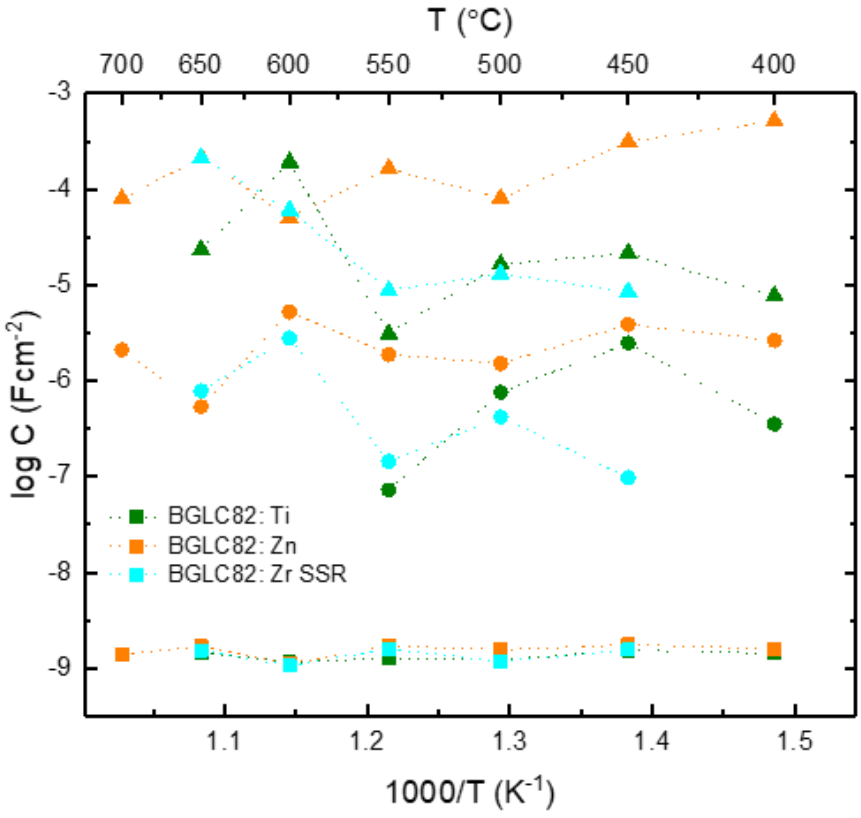

Figure 5.24 The respective capacitance temperature dependencies for the different electrodes, where (■) are related to ohmic, (●) for $R_{p,2}$ and (▲) $R_{p,3}$.

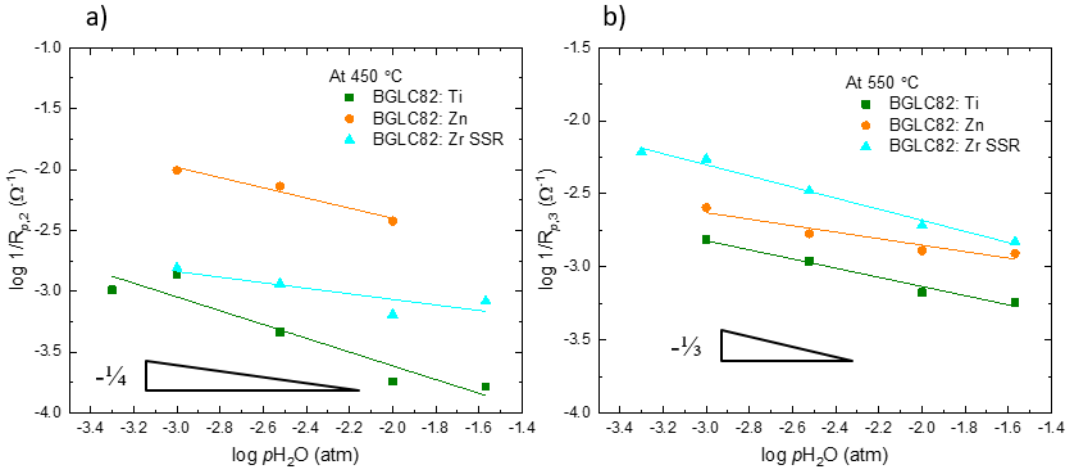

Figure 5. 25 pH$_2$O dependencies comparison between the electrodes and the polarisation resistances a) R$_{p,2}$ at 450 °C and b) R$_{p,3}$ at 550 °C, with a positive bias and pO$_2$ = 0.20 atm.

The respective pH$_2$O dependencies of the different contributions and the various electrodes are presented in Figure A.4.1, while the reaction orders are presented in Table 5.8.

Table 5.8 The reaction orders R$_{p,2}$ (p,2) and R$_{p,3}$ (p,3) of the different electrodes under positive bias.

	BGLC82: Ti		BGLC82: Zn		BGLC82: Zr SSR	
T (°C)	$n_{p,2}$	$n_{p,3}$	$n_{p,2}$	$n_{p,3}$	$n_{p,2}$	$n_{p,3}$
700	--	--	--	--	--	--
650	--	-⅓	--	--	--	--
600	--	--	--	--	--	-¾
550	--	-⅓	-⅓	-⅕	-⅓	-⅖
500	-⅓	-⅓	-⅕	-¼	0	-⅖
450	-½	-⅖	-⅖	-1/10	-¼	-⅓
400	-⅕	-¼	-⅖	-1/10	-⅓	-⅓
350	--	--	-1/10	-1/10	--	--
Avg	-¼	-⅓	-⅓	-1/10	-¼	-⅖

6 Discussion

The interpretation and discussion of the obtained results in this work are presented in this chapter, with focus on clarifying the different behaviour between the electrodes at OCV and bias, as well as comparing them to BGLC82. Proton uptake and structural properties are made clear and are included in the analysis of the different electrode materials. Additionally, the electrolyte contribution is interpreted to justify the experimental setup. Finally, possible directions for further investigation of the prepared electrode are considered.

6.1 Structural - Insight

The electrode materials BGLC82: Ti and BGLC82: Zn were successfully synthesized by the solid-state reaction, as shown by the XRD in Figure 5.1. The same synthesis approach was unsuccessful in obtaining a pure single phase of BGLC82: Zr. The presence of a secondary $BaZrO_3$ phase was observed. The sol-gel approach of the BGLC82: Zr showed a decrease of the secondary phase, but was not successful either in obtaining a pure single phase. The sol-gel method has proven to yield a notably smaller amount of the secondary phase, indicating that the solid-state reaction suffers from inhomogeneous distribution of precursors compared to the sol-gel method, which has been reported when doping materials [75]. At the same time, the small amount of the secondary phase obtained from the sol-gel method can be an indication that the solubility limit of Zr in BGLC82 had been reached.

6.2 Proton Uptake

Due to the secondary phase in both BGLC:82 Zr, the proton uptake properties of these materials were not tested, as the $BaZrO_3$ might result in a higher proton uptake for the composite electrode. The BGLC82: Ti and BGLC:82 Zn both exhibit water uptake from TGA measurement, as shown in Figure 5.3. The two compositions of BGLC82 were exposed to D_2O vapour where BGLC82: Ti exhibited a second weight gain, as seen in Figure 5.2, which yielded a higher proton uptake at 300 °C for BGLC82: Ti than BGLC82 and BGLC82: Zn. The calculations is shown in the Appendix.

For materials with mixed valent cations (Co, Fe, Cu, etc.), like BGLC82, the electronic defects are not minority defects, as explained in the theory part. This changes the proton uptake of BGLC82: Zn and Ti. In addition, a proton uptake process for materials with mixed valent cations, known as hydrogenation is reported in literature. The protonic defects are obtained through hydrogenation, as shown below:

$$H_2O\,(g) + 2O_O^x + 2M_M^x \rightleftharpoons 2OH_O^\bullet + 2M_M' \qquad (6.1)$$

where M is a mixed valent cation.

By considering the defect model for mixed valent cations and the suggested defect model for BGLC82 reported by Vøllestad et al. [13], the electroneutrality for BGLC82 acceptor doped with zinc becomes

$$\frac{1}{2}\left[Co_{Co}^{\frac{1}{2}'}\right] + \frac{3}{2}\left[Co_{Co}^{\frac{3}{2}'}\right] + \frac{3}{2}\left[Zn_{Co}^{\frac{3}{2}'}\right] = 2[v_O^{\bullet\bullet}] + \frac{1}{2}\left[Co_{Co}^{\frac{1}{2}\bullet}\right] + [OH_O^\bullet] \qquad (6.2)$$

and for BGLC82 donor doped with titanium

$$\frac{1}{2}\left[Co_{Co}^{\frac{1}{2}'}\right] + \frac{3}{2}\left[Co_{Co}^{\frac{3}{2}'}\right] = [OH_O^\bullet] + 2[v_O^{\bullet\bullet}] + \frac{1}{2}\left[Ti_{Co}^{\frac{1}{2}\bullet}\right] \qquad (6.3)$$

TGA measurements, shows that BGLC82 acceptor-doped with zinc exhibits smaller proton uptake than BGLC82, as shown in Figure 5.3. The acceptor-doped BGLC82 exhibit no weight gain at the D_2O shift as seen in Figure 5.2, indicating the proton uptake is too small to measure with TGA, and the majority of the weight gain is from oxygen, as the material obtains protonic defects through hydration. The proton uptake decreased upon acceptor doping suggesting that the concentration of oxygen vacancies are not increased with the acceptor defect and the increase of holes in the form of $Co_{Co}^{\frac{1}{2}\bullet}$, is known to reduce proton stability, as seen in the electroneutrality (Equation 6.2).

For the donor-doped sample with titanium, the electroneutrality (Equation 6.3**)** indicates that the oxygen vacancies are not a compensating defect of titanium. This implies that the proton uptake from hydration will not increase with the dopant. The donor-dopant is compensated by electrons in the form of $Co_{Co}^{\frac{1}{2}'}$ and $Co_{Co}^{\frac{3}{2}'}$ and strengthen the proton stability as seen in the electroneutrality (Equation 6.3). BGLC82: Ti exhibits a weight increase with the D_2O shift, as

seen in Figure 5.2. The increase observed was ⅔ of the H_2O shift, making the proton uptake too significant to only be related to hydration and indicating that hydrogenation occurs for the material. The weight gain obtained from D_2O implies that 94 % of the protons are obtained by hydrogenation, whereas the rest of the protons (6 %) are obtained by hydration. The higher temperatures measurements indicate that more oxygen vacancies occur as the ratio between hydrogenation and hydration becomes 65 % and 35 %. The TGA measurements of BGLC82: Ti correspond to reported observations in the literature where the basicity of the dopant stabilises the protonic defect in the oxides [47, 48, 69].

6.3 Positrode at OCV – Insight

One of the main objectives of this work is to understand the effect of dopants on B-site for BGLC82. In this section, behaviours and results obtained from OCV measurement of the different electrodes will be compared to literature values, and each other to understand the effect of substitution on B-site for BGLC82. First, insight into the values from the electrolyte behaviour to validate the experimental setup.

6.3.1 Electrolyte contribution

The measurement setup allowed a large variety of electrodes to be tested over a short amount of time by placing them on the same electrolyte. The question if the measurements obtained by the experimental setup are comparable with each other and documented work has to be discussed.

An attempt to justify the experimental setup is made by looking at the activation energy values obtained from the different electrodes. From Table 5.5, the activation energies for the ohmic contribution measured at the different electrodes are similar to each other, with an average of $0.71\ eV \pm 0.08_9$. The average activation energy is similar to the reported value in M.K. Pedersen work [71] where the BGLC82 pellet was placed on a BZCY72 electrolyte pellet, with an activation energy of $0.78_5\ eV \pm 0.06_5$. However, the values are higher than other reported literature values of 0.4 – 0.6 eV [38, 76]. The discrepancy between the values might originate due to grain boundary resistance in the measured resistance. The grain boundary has shown to affect the proton conductivity through oxides [52], which results in an average conductivity of protons described by Equation 2.24. The average activation energy for protons moving through

the grain boundary regions and grain boundary-free regions is given by the total conductivity of protons defined by the Arrhenius equation for jumping mechanisms (Equation 2.27). Furthermore, the electrolyte capacitances obtained at OCV were measured to be in a range of ~10^{-10}–10^{-9} Fcm^{-2} for all the electrodes, which implies that the same process occurs for the different measurements. The consistency of capacitances and activation energies for the electrolyte implies that the experimental setup provided acceptable data for each of the electrodes.

6.3.2 Positrode contribution

As mentioned earlier, the values for the $R_{p,2}$ and $R_{p,3}$ exhibit scattering of the data points for the temperature dependencies, as the measurements were carried out in the following temperature order 600 – 350, 650, 550, and 450, which led to some inaccuracy in the data. The data points are still included, as there is no significant change in the results by not including them.

The question if there is a $R_{p,2}$ contributions that can be seen in the impedance measurement remains, as there is no notable semicircle at the mid-frequency range like for R_{ohm} and $R_{p,3}$. However, deconvolution of the different impedances implies that there is a contribution, but masked by the two significant contributions R_{ohm} and $R_{p,3}$. The masking of the $R_{p,2}$ contributions results in challenges in obtaining acceptable data points, which can be seen in the pO_2 and pH_2O dependencies in Figure 5.12 b) and Figure 5.15 b).

$R_{p,2}$ contribution

The $R_{p,2}$ contributions are observed in the mid-frequency range in the impedance, where the charge transfer processes appear. The obtained values of the capacitances were in a range of ~10^{-8} – 10^{-6} Fcm^{-2} for all the electrodes, as seen in Figure 5.9 and Table 5.4.

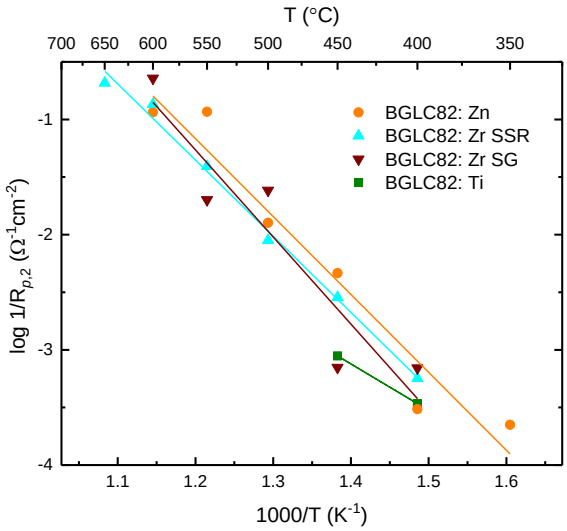

Figure 6.1 Temperature dependencies of $R_{p,2}$ for the different electrodes.

The activation energies of $R_{p,2}$ average around 1.4 eV ± 0.2 for all the electrodes, as shown in Table 5.5. BGLC82 seems to exhibit a similar activation energy at temperatures between 700 – 500 °C [71]. BGLC82 exhibits a lower activation energy for $R_{p,2}$ of 0.85 eV at 500 – 350 °C [71]. This change in activation energy was not observed for any of the tested electrodes in this work. The similar capacitances and activation energies for the tested electrodes imply that the same type of process is measured over the temperatures range and the different electrodes.

Table 6.1 The $R_{p,2}$ resistance at 400 °C for the different BGLC82 compositions and BGLC82.

	BGLC82: Zn	BGLC82: Ti	BGLC82: Zr SSR	BGLC82: ZR SG	BGLC82[71]
$R_{p,2}$ at 400 °C	3.2 kΩcm^2	2.9 kΩcm^2	1.7 kΩcm^2	1.4 kΩcm^2	2.3 kΩcm^2

The $R_{p,2}$ values at 400 °C for all the electrodes are seen in Table 6.1. BGLC82: Zr SG obtained the lowest resistance of all the electrodes tested and the literature value of BGLC82. The BGLC82: Zr SSR exhibit similar resistance as the BGLC82: Zr SG electrode, where BGLC82: Ti and Zn obtain a similar resistance ~ 3 kΩcm^2.

Table 6.2 The pre-exponential factor (A_0) of $R_{p,2}$ for the tested electrodes and BGLC82.

	BGLC82: Zn	BGLC82: Ti	BGLC82: Zr SSR	BGLC82: ZR SG	BGLC82[71]
A_0 **for** $R_{p,2}$ **($\Omega^{-1}cm^{-2}$)**	$1.7 \cdot 10^6$	--	$7.4 \cdot 10^5$	$1.2 \cdot 10^7$	$7.2 \cdot 10^6$

For the pre-exponential factor, BGLC82: Zr SG exhibit the highest values of all the electrode and BGLC82, as seen in Table 6.2. The high value indicates that BGLC82: Zr SG has more active sites for the charge transfer reaction than the other electrodes. The pre-exponential and the low $R_{p,2}$ resistance indicates that BGLC82: Zr SG performed better than BGLC82.

For the $R_{p,2}$, the different electrodes exhibit pO_2 dependencies close to ⅓ and a negative water vapour dependencies between 0 and -⅓. The dependencies indicate that the redox reaction of absorbed oxygen, Reaction 2.32, is the rate-limiting step for the $R_{p,2}$ contributions. This step has also been suggested as a possible RDS by Poetzsch et al. [18]. The $R_{p,2}$ exhibited negative water dependencies at all the electrodes. This can be an indication that the electrode surface is saturated with OH^- and H_2O. This means that the electrodes are not operating in dilute conditions. This implies that the Langmuir isotherm model is not valid, as there is too few no open sites at the electrode surface

An explanation for the performance of the BGLC82: Zr SG electrode is that at a lower temperature, proton uptake for the electrode increases, as shown for BGLC82: Ti. This behaviour suggests that BGLC82: Zr can exhibit higher proton uptake than BGLC82 and BGLC82: Ti. However, BGLC82: Zr SSR showed similar performance as BGLC82: Zr SG, but XRD showed a higher amount of $BaZrO_3$ than the sol-gel method and therefore experienced the similar performance as it is seen as a composite electrode.

$R_{p,3}$ contribution

The $R_{p,3}$ polarisation resistance exhibit capacitances in a range of ~10^{-6}-10^{-5} Fcm^{-2}, which is close to the capacitance of $R_{p,2}$. However, the $R_{p,3}$ are seen as the third semicircle in the Nyquist plot, which is the low-frequency range where the mass transfer contribution appears.

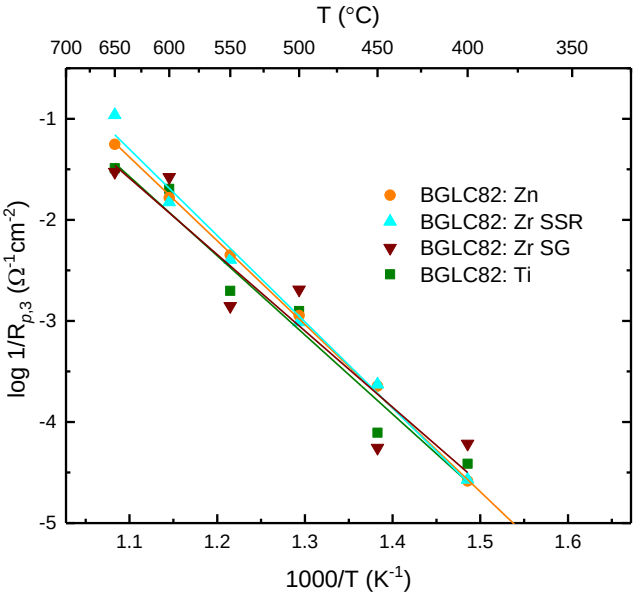

Figure 6.2 Temperature dependencies of $R_{p,3}$ for the different electrodes.

The activation energy of $R_{p,3}$ average around 1.5 eV ± 0.2 for all the electrodes, and are similar to the observed value of BGLC82 at 1.4 eV ± 0.2 [71]. Like the activation energies of $R_{p,2}$, the $R_{p,3}$ did not exhibit lower activation energy at low temperature, which has been seen for BGLC82 [7, 71]

Table 6.3 The $R_{p,3}$ resistance at 500 °C for the different BGLC82 compositions and BGLC82.

	BGLC82: Zn	BGLC82: Ti	BGLC82: Zr SSR	BGLC82: ZR SG	BGLC82[71]
$R_{p,3}$ at 500 °C	0.89 kΩcm^2	0.79 kΩcm^2	1.0 kΩcm^2	0.49 kΩcm^2	0.33kΩcm^2

BGLC82 exhibits the lowest resistance of $R_{p,3}$ at 500 °C, where BGLC82: Zr SG obtained the lowest resistance of the tested electrodes, as seen in Table 6.3. BGLC82: Ti and Zn obtained similar resistances, with BGLC82: Ti obtaining the lower value of them. BGLC82: Zr SSR was the electrode with the highest resistance.

The pre-exponentials for the $R_{p,3}$ for the different electrodes are shown in Table 6.4. BGLC82: Zr SG was the electrode closest to BGLC82 in $R_{p,3}$ at 500 °C, but experienced a lower pre-exponential factor than BGLC82. This means that BGLC82: Zr SG has fewer active sites than

BGLC82. For the other electrodes BGLC82: Ti obtained a pre-exponential close to BGLC82: Zr SG. BGLC82: Zn and Zr SSR obtained a similar pre-exponential as BGLC82.

Table 6.4 The pre-exponential factor (A_0) of $R_{p,3}$ for the tested electrodes and BGLC82.

	BGLC82: Zn	BGLC82: Ti	BGLC82: Zr SSR	BGLC82: ZR SG	BGLC82[71]
A_0 **for** $R_{p,3}$ ($\Omega^{-1}cm^{-2}$)	$1.0 \cdot 10^7$	$2.2 \cdot 10^6$	$2.4 \cdot 10^7$	$1.0 \cdot 10^6$	$1.2 \cdot 10^7$

For the oxygen and water vapour dependencies, the electrodes exhibit a positive pO_2 dependency of ⅖ and a negative water vapour dependency of - ¼. The dependencies indicate that the rate-limiting step is the dissociative exchange of oxygen (Reaction 2.34) [18]. The negative pH_2O dependency for $R_{p,3}$, indicates that the electrode surface is saturated as mentioned for $R_{p,2}$.

The $R_{p,3}$ resistances of the electrodes exhibit to be higher compared to BGLC82. Previous work has shown that BGLC82 exhibit polarization resistance down to 0.5 Ωcm^2 at 650 ℃ [7] and 5.2 $k\Omega cm^2$ at 350 ℃ [71]. This difference might be due to the size of the working electrodes and microstructure, as the mass transfer processes will vary with electrode size because the processes that yield polarisation resistance are absorption and desorption of species. Other studies have shown low polarisation resistance in large-area PCFC [77, 78]. This indicates that the normalizing area should be different for the charge transfer and mass transfer processes when presented.

6.4 Positrode at Bias –Insight

Positrode materials for PCEC should exhibit high performances in both directions of the positrode reaction. EIS measurements at OCV yield an average performance of the positrode as both direction equally dominates. By applying either a negative or positive bias, one of the direction will dominate and provide specialised results for the positrode. These results will disclose whether the positrode performers best as an anode or cathode.

6.4.1 Electrolyte at Bias

The obtained data from the ohmic contributions is shown in Table A.3.1-Table A.3.3 for the negative bias, and Table A.4.1 – Table A.4.3 for the positive bias measurements.

The validity of the experimental setup can be determined by comparing the results of the electrolyte OCV and bias measurements. The jumping mechanism determines the movement of protons in the electrolyte according to the Nernst-Einstein relationship (Equation 2.26). This means that the proton should experience the same energy barrier for different potentials, as the potential gradient does not affect the diffusion of species. The activation energies for the electrolyte are presented in Table 6.5 for both positive and negative bias and OCV.

Table 6.5 Activation energies (E_a) for the proton jumping at different bias and OCV, with the different BGLC82 composition as the working electrode. The obtained E_a of the bias measurements are found in the Appendix.

	E_a at Positive-bias (eV)	E_a at OCV (eV)	E_a at Negative-bias (eV)
BGLC82: Zn	0.70 ± 0.02	0.69 ± 0.02	0.74 ± 0.03
BGLC82: Ti	0.7 ± 0.1	0.8 ± 0.1	0.8 ± 0.1
BGLC82: Zr SSR	0.73 ± 0.02	0.77 ± 0.01	0.74 ± 0.02
BGLC82: Zr SG	--	0.6 ± 0.2	--
Avg	0.7 ± 0.1	0.7 ± 0.3	0.8 ± 0.1

The activation energies for proton jumping obtained from the electrochemical measurements are similar to each other, despite the different potentials. The results imply that the same

mechanism occurs in the electrolyte, independent of change in the potential gradient. This compliance with the theory means that the jumping mechanism is not affected by a potential gradient.

The capacitances from both the positive and negative bias measurements obtained similar values as the OCV measurements, of ~10^{-9} Fcm^{-2}. This suggests that the same process occurs in the electrolyte during all the measurement with different working electrodes and different biases.

6.4.2 Positrode Behaviour at Negativ Bias

When the electrochemical cell is exposed to a negative bias under impedance measurements, the positrode reaction moves towards the cathodic reaction. The positrodes then become cathodes, and the positrode reaction becomes:

$$O_2(g) + 4e^- + 4H^+ \rightarrow H_2O\ (g) \qquad (6.4)$$

Capacitances for the two electrode polarization resistances are seen in Table A.3.2 in the Appendix. The obtained values were in a range of ~10^{-8}-10^{-6} Fcm^{-2} for $R_{p,2}$, and ~10^{-6}-10^{-4} Fcm^{-2} for $R_{p,3}$. The capacitances for $R_{p,2}$ and $R_{p,3}$ indicate that the same positrode process takes place when measuring at OCV and negative bias.

The activation energies of $R_{p,2}$ average around 1.3 eV ± 0.1 for all the electrodes, and are similar to the obtained values of the OCV measurements, as seen in the previous section. For the $R_{p,3}$, the activation energies of BGLC82: Ti and Zn are similar and average around 1.52 eV ± 0.07. For the BGLC82: Zr SSR electrode, the activation energy was 1.84 eV ± 0.09.

The activation energies of $R_{p,3}$ for BGLC82: Ti and Zn at negative bias are similar to the OCV measurements. However, BGLC82: Zr SSR exhibits higher activation energy than the OCV measurements. This change in activation energy proposes that a different process occurs for the BGLC82: Zr SSR electrode.

The obtained values for capacitances and activation energies imply that the same process is measured for $R_{p,2}$ at negative bias as for OCV. The $R_{p,3}$ values were similar to what was observed at OCV for BGLC82: Ti and Zn. As mention above, BGLC82: Zr SSR exhibits a higher activation energy than at OCV and proposes that a different process occurs. However, pH_2O dependencies, from Table 5.7, implies that the rate-limiting step is the same.

Table 6.6 Polarisation resistances for the different electrodes at negative bias.

	T (°C)	$R_{p,2}$ at negative bias ($k\Omega cm^2$)	$R_{p,3}$ at negative bias ($k\Omega cm^2$)
BGLC82: Ti	500	0.21	1.3
	400	6.3	44
BGLC82: Zn	500	0.18	1.2
	400	2.6	23
BGLC82: Zr SSR	500	0.31	1.9
	400	2.1[III]	41[IV]

The $R_{p,2}$ and $R_{p,3}$ values in Table 6.6 show that BGLC82: Zn exhibits the lowest resistance of all the electrodes under negative bias. The pre-exponential of BGLC82: Zn is also similar to what is observed at OCV. BGLC82: Ti and BGLC82: Zr SSR electrodes exhibit similar values, as seen in Table 6.6. However, BGLC82: Zr SSR obtained a higher pre-exponential factor than at OCV. The increase implies that there are more active sites for the reaction, but the electrode obtained higher resistance than BGLC82: Zn, as shown in Table A.3.3. This suggests that there is a change in the rate-limiting step that defines $R_{p,3}$ for BGLC82: Zr SSR. The lack of pO_2 dependency with negative bias measurements makes it difficult to propose a different rate-limiting step for the electrode. The resistances obtained by the negative bias measurement indicate that BGLC82: Zn is the best performing positrode as a cathode.

6.4.3 Positrode Behaviour at Positive Bias

When the electrochemical cell is exposed to a positive bias, the positrode reaction moves towards the anodic reaction. The positrodes then become an anode, and the positrode reaction becomes:

$$O_2(g) + 4e^- + 4H^+ \leftarrow H_2O\ (g) \qquad (6.5)$$

[III] The value is an estimate from the linear regression in Figure 5.19 b)
[IV] The value is an estimate from the linear regression inFigure 5.19 c).

The measured capacitances for the $R_{p,2}$ were observed to be in a range of ~10^{-8}-10^{-6} Fcm^{-2}, as seen in Table A.4.2 and Figure 5.24. The $R_{p,2}$ capacitances are similar to what was detected for both OCV and negative bias measurements. Capacitances observed for $R_{p,3}$ were in a range of ~10^{-5}-10^{-4} Fcm^{-2}, as seen in Table A.4.2 and Figure 5.24. These capacitances are higher than for OCV, and negative bias measurements and therefore might indicate a process change for the $R_{p,3}$ contribution at positive bias.

The activation energies of BGLC82: Ti and Zn for $R_{p,2}$ are similar, as seen in Table A.4.3. The $R_{p,2}$ activation energy for BGLC82: Ti exhibits an uncertainty of ± 0.5. The activation energy of BGLC82: Zr SSR is significantly higher than for BGLC82: Ti and Zn for $R_{p,2}$ (1.9 eV ± 0.4). These values have to be viewed with care as the uncertainties of them are significant. The BGLC:82 Ti and Zn exhibit close to the same activation energies as for OCV and negative bias. The activation energy for $R_{p,3}$ was similar for BGLC82: Ti and Zn, with an average of 1.52 eV ± 0.07. BGLC82: Zr SSR exhibit activation energy of 1.8 eV ± 0.1 and are similar to what was observed at negative bias. As for the negative bias measurements, the activation energy for BGLC82: Zr SSR suggest that another rate-limiting step is observed. However, the lack of pO_2 dependency with positive bias measurement makes it difficult to propose a rate-limiting step.

Table 6.7 Polarisation resistances for the different electrodes at positive bias.

	T (°C)	$R_{p,2}$ at positive bias ($k\Omega cm^2$)	$R_{p,3}$ at positive bias ($k\Omega cm^2$)
BGLC82: Ti	500	0.048	0.2
	400	0.62	7.9
BGLC82: Zn	500	0.052	2.9
	400	0.34	66
BGLC82: Zr SSR	500	0.046	0.3
	400	0.75[V]	11[VI]

The $R_{p,2}$ and $R_{p,3}$ values in Table 6.7, show that all the electrodes obtain a similar resistance for the $R_{p,2}$. The resistances obtained are also lower than from the negative bias measurements at the same temperature. For the $R_{p,3}$ resistances, the BGLC82: Ti electrode exhibits the lowest

[V] Calculated value from linear regression of the 400 °C measurements in Figure A.4.1 c.2
[VI] Calculated value from linear regression of the 400 °C measurements in Figure A.4.1 c.3

resistance of all the electrodes. For the pre-exponential factor, BGLC82: Ti obtain a higher value than BGLC82: Zn, and it implies that BGLC82: Ti has more active sites than BGLC82: Zn. For the BGLC82: Zr SSR, the pre-exponential is higher than BGLC82: Ti and Zn. However, the higher activation energy and high $R_{p,3}$ implies that another rate-limiting step causes the electrode to perform worse than BGLC82: Ti. This implies that BGLC82: Ti is the best performing positrode as an anode.

6.4.4 Performance under Bias

BGLC82: Ti exhibit the lowest resistance at the positive bias of all the electrode. As mention above, this implies that BGLC82: Ti is the best positrode used as an anode. When a positrode is used as an anode, the PCEC are in electrolyser mode (Reaction 6.5). In Figure 6.3, the total polarization resistance ($R_{p,T} = R_{p,2} + R_{p,3}$) at OCV and for bias measurements are presented.

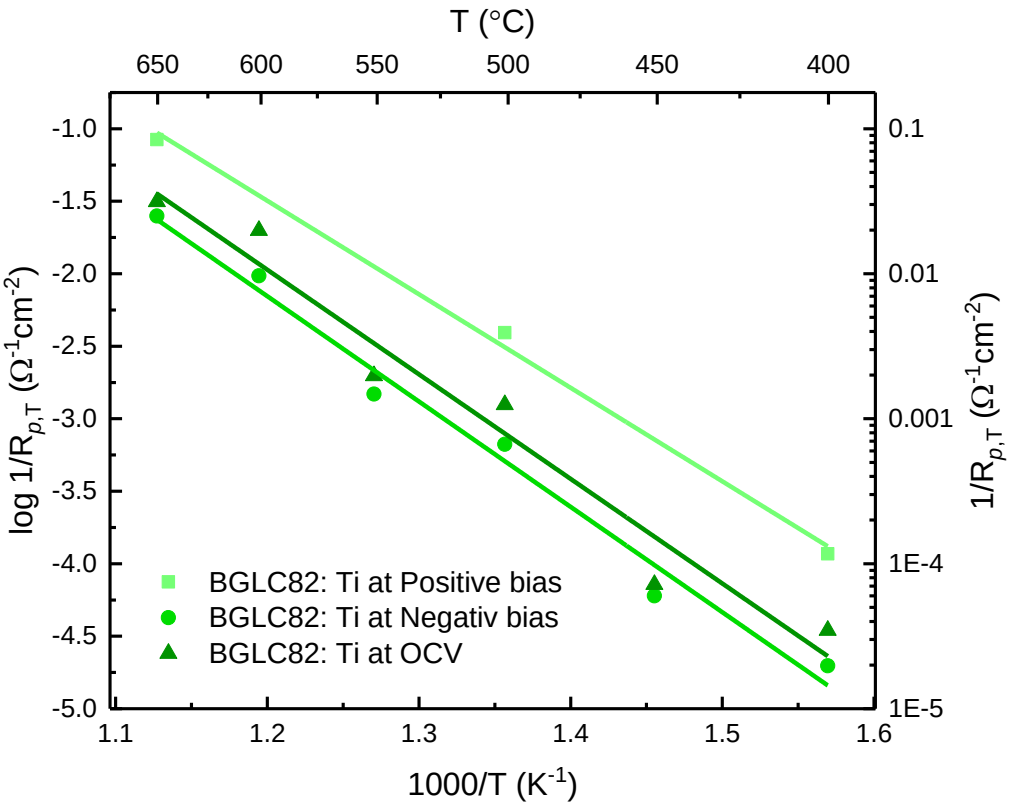

Figure 6.3 Total polarization resistance ($R_{p,T}$) of BGLC82: Ti at OVC and bias.

The $R_{p,T}$ of positive bias measurements is seen lower than the OCV and negative bias measurement. This implies that the electrode performs better at positive bias. However, for an ideal electrode, the $R_{p,T}$ should be the same for negative and positive bias, as seen in Figure 2.7.

BGLC82: Zn was the electrode that exhibited the best performance at negative bias, thus as a cathode. In Figure 6.4 the similar behaviour as for BGLC82: Ti is observed only reversed. The $R_{p,T}$ for negative bias is lower than for the positive bias.

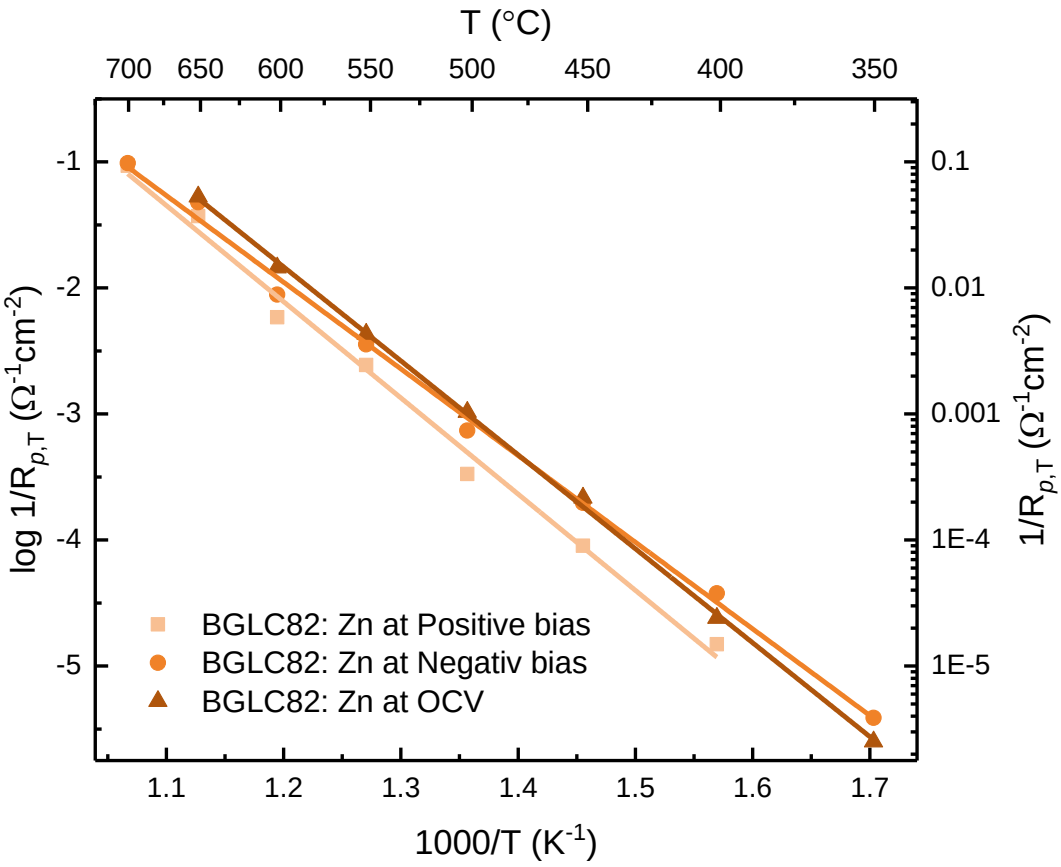

Figure 6.4 Total polarization resistance ($R_{p,T}$) for BGLC82: Zn at OVC and bias.

In Figure 6.5, the $R_{p,T}$ exhibit the same behaviour as for BGLC82: Ti, with $R_{p,T}$ of the positive measurement lower than OCV and negative bias, for BGLC82: Zr SSR.

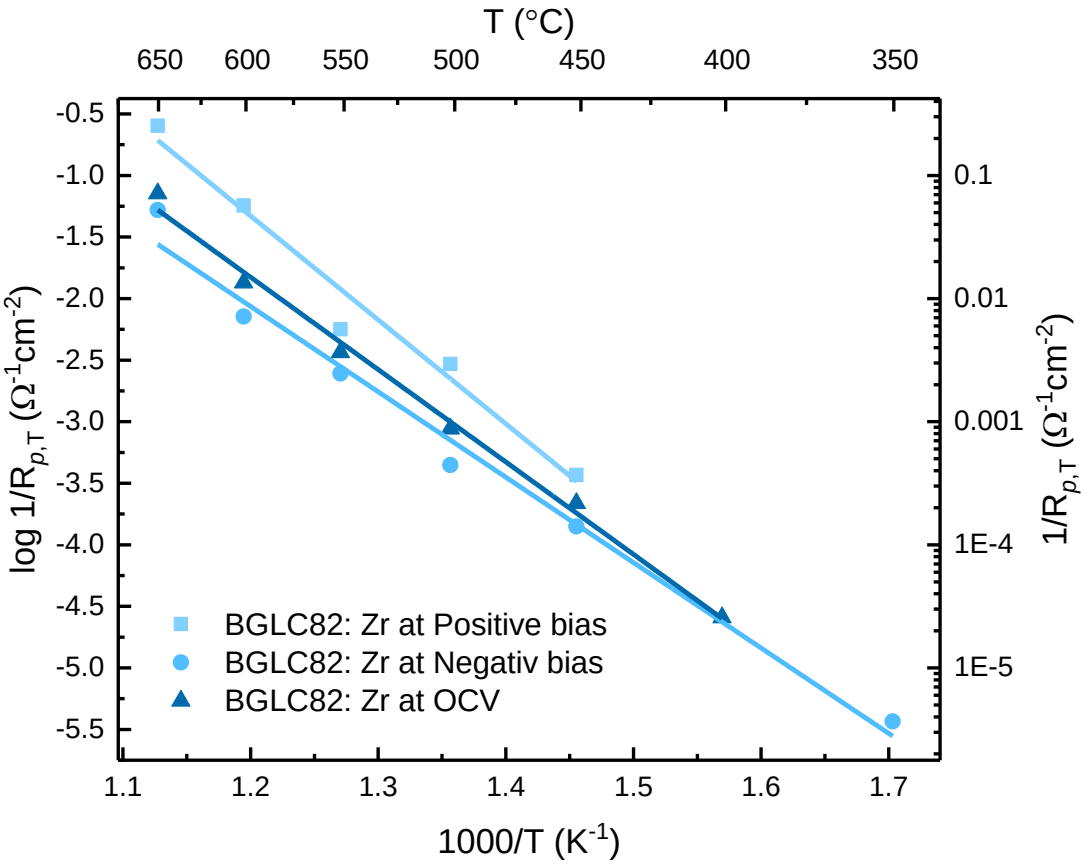

Figure 6.5 Total polarization resistance ($R_{p,T}$) of BGLC82: Zr SSR at OVC and bias.

One explanation for this behaviour is that α in the Butler-Volmer equation is not equal to ½. By suggesting that α ≠ ½ the I-V curve becomes asymmetrical and yield slow kinetic for either anodic or cathodic direction depending α is higher or lower than ½.

A second explanation is that the p-type conductivity increases in the electrolyte when the electrochemical cell is exposed to a positive bias [4]. The electron-hole conductivity can be described as:

$$\sigma_{\mathrm{p}} = \sigma_p^0 \cdot \frac{a_{H^+} p\mathrm{O}_2^{1/4}}{p\mathrm{H}_2\mathrm{O}^{\frac{1}{2}}} \tag{6.6}$$

where σ_p^0 is the p-type conductivity under standard conditions (pO$_2$ = 1 atm and pH$_2$O = 1 atm). The partial pressures dependencies from Equation 6.**6** can be rewritten in terms of the Nernst potential for the oxygen reduction reaction:

$$\mathrm{E} = \mathrm{E}^0 + \frac{RT}{2F}\ln\left(\frac{a_{H^+} pO_2^{\frac{1}{2}}}{pH_2O}\right) \quad (6.7)$$

By combining Equation 6.6 and 6.**7**, gives the p-type conductivity in terms of potential changes:

$$\sigma_\mathrm{p} = \sigma_\mathrm{p}^0 \cdot \exp\left(\frac{F(E - E^0)}{RT}\right) \quad (6.8)$$

From the equation above, the p-type conductivity increases with the increasing potential *E* for the electrolyte. This implies that the increase of the potential increases the pO_2. From Figure 2.3 and Figure 2.5, the hole concentration for both BZY and BGLC82 increases with increasing *p*O2. This increase the p-type conductivity in the materials and results in lower measured resistances by electronic leakage through the electrolyte [4, 7]. From Equation 6.6, the p-type conductivity is decreasing by an increase of the pH_2O. This can also be an explanation for the negative water dependencies for the polarization resistances.

The third explanation is that the rate-limiting step changed for the electrode when it is exposed to different bias. By changing the rate-limiting step for the different bias measurement, the exchange current density (j_0) changes. From the theory in Section 2.5.2, the exchange current density includes the rate of both the anodic and cathodic direction of a process. The anodic and cathodic rate of a process includes concentrations of the involved species and partial pressures of oxygen and water vapour. When the electrode rate-limiting step changes as a consequence of the potential direction. The exchange current density is different for the different potential and yield a different resistance for the polarization resistances.

6.5 Further Work

A natural continuation of this work is to investigate the electrodes more thoroughly at temperatures between 300 – 500 ℃. This will give a better understanding of whether the electrodes experience proton conductivity through bulk or surface.

Furthermore, the oxygen nonstoichiometry for the different BGLC82 compositions should be investigated. This will give a broader understanding of doping in BGLC82 related to proton uptake. Different quantities of the dopants in BGLC82 should be investigated to get a greater understanding of the effect of doping.

The study of the size differences of the same working electrode would give insight into the change in R_p. This might result in a novel way to compare different electrodes R_p.

The sol-gel synthesis of BGLC82: Zr revealed that the solubility limit of zirconia in BGLC82 might have been reached. The synthesis of a single phase of BGLC82: Zr and the subsequent testing of the material in the same manner as in this work would reveal whether BGLC82: Zr performs better than the tested electrode in this work or not.

As mentioned in the introduction, a PEMFC is struggling with slow electrode kinetics. From recent work, double-perovskites like BGLC82 have shown to obtain close to similar performances as noble metals [79]. Testing BGLC82 with and without different dopants at room temperature will clarify whether BGLC82 exhibits the same behaviour with the dopants as in the high-temperature measurement. Additionally, it would provide more research into the development of electrodes with multi-usage.

7 Summarising conclusions

In the presented work, functional properties and performances of $BaGd_{0.8}La_{0.2}Co_{1.8}X_{0.2}O_{6-\delta}$ (X = Zn, Ti and Zr) as PCECs positrodes were investigated. The Ti and Zn compositions were successfully synthesized with solid-state reaction. The Zr composition was synthesized with both solid-state reaction and sol-gel methods but was not obtained as a single phase of BGLC82: Zr. The sol-gel method implies that solubility of Zr in BGLC82 was reached. The materials were pressed to pellets and sintered to a density of around 80 %.

Powders of the Ti and Zn compositions were tested for proton uptake with TGA at 300-500 ℃. BGLC82: Ti exhibits a higher proton concentration than BGLC82: Zn and for BGLC82. The proton uptake indicated that hydrogenation occurs for the Ti composition at all the tested temperatures. The high proton uptake related to what has been reported on materials doped with more basic cations [69].

The experimental setup was obtained by placing the different electrodes on a BZCY72 electrolyte pellet. The electrode surface that were in contact with the electrolyte and the electrolyte surface were polished to obtain an acceptable contact. The reference and counter electrode were made of platinum, placed on the opposite side of the working electrodes. Electrochemical impedance spectroscopy was measured at OCV and negative and positive bias. The measurements were carried out under controlled atmospheres and varying temperatures. All of the measurements were successfully carried out for all the electrodes.

The electrolyte contribution exhibit similar activation energy for all the measurements from the different electrodes. The obtained activation energies averaged around 0.7 eV ± 0.4 for all the measurements and electrodes. This result justifies the experimental setup as the activation energy for the electrolyte contribution should be the same independent of the working electrode.

From the OCV measurement, the polarization resistances were compared with literature values for BGLC82. The BGLC82: Zr SG was the electrode that exhibited close to the same performance as reported for BGLC82 for both $R_{p,2}$ and $R_{p,3}$. For the two electrodes that exhibit a single-phase (BGLC82: Ti and Zn), it was the Ti composition that obtained the best performance. This indicates that doping BGLC82 with a more basic cation increases the performance of the electrode.

For the oxygen and water vapour pressure dependencies, $R_{p,2}$ and $R_{p,3}$ Exhibited for all the electrodes dependencies on both pO_2 and pH_2O. From the dependencies, the rate-limiting step was determined to be red-ox of absorbed oxygen for $R_{p,2}$, and the dissociative exchange of oxygen for $R_{p,3}$. The higher resistances obtained for all the measurements for $R_{p,3}$ indicate that the RDS for the electrodes is the dissociative exchange of oxygen.

For BGLC82: Zn, the lowest total polarization resistance was seen under negative bias measurement. The $R_{p,2}$ exhibits similar pre-exponential factors for both positive and negative bias. For $R_{p,3,}$ the highest factor value was obtained at the negative bias measurement. This implies that the electrode has more active sites when it is operating as a cathode.

BGLC82: Ti obtained the lowest total polarization resistance of all the electrodes at positive bias. The electrode exhibits also more active sites during positive bias measurement than at negative bias. This implies that the electrode is a better anode than cathode for a PCEC.

Zinc and titanium are acceptor and donor dopant for BGLC82, respectively. BGLC82: Ti and Zn exhibit lower resistances at different biases, which indicates that the electrodes performed better in the different directions of the positrode reaction. This implies more proton uptake for the oxide, resulting in a better positrode for proton ceramic electrolyser. Less stability of protons in the positrode results in a positrode more suited for proton ceramic fuel cell.

The three suggested explanations for the different obtained values for the polarization resistances at positive and negative bias can all occur at the same time with high or low contributions on the resistance. However, some of the results from the measurement can imply to what extent they influence the results. Assuming that the second explanation has a high impact on the polarisation residences, all of the electrodes should exhibit lower resistances under positive bias measurements, as all the electrode is on the same electrolyte. BGLC82: Ti was the electrode with the largest difference between the total polarisation resistance obtained from negative and positive bias. This implies that the increase in p-type conductivity under positive bias did not affect the polarization resistances significantly for the electrodes.

Concerning the first and third explanation, when the electrode exhibits the same RDS at both positive and negative bias, the exchange current density should be the same. This implies that the difference in the anodic and cathodic resistance is obtained by $\alpha \neq ½$. When the RDS is observed to be different for the electrode at negative and positive bias, the difference in

resistance can come from the exchange current density. This implies that there are different exchange current densities at negative and positive bias, due to the change in rate-limiting step for the same electrode. From the observed capacitances, capacitances, activation energies, and water dependencies indicate that there is a change of the RDS for negative and positive bias. This indicates that the exchange current density leads to the difference in polarization resistance.

Bibliography

1. Agency, I.E., *The Future of Hydrogen*. 2019.
2. Bellows, R.J., E.P. Marucchi-Soos, and D.T. Buckley, *Analysis of Reaction Kinetics for Carbon Monoxide and Carbon Dioxide on Polycrystalline Platinum Relative to Fuel Cell Operation.* Industrial & Engineering Chemistry Research, 1996. **35**(4): p. 1235-1242.
3. Adams, T.A., et al., *Energy Conversion with Solid Oxide Fuel Cell Systems: A Review of Concepts and Outlooks for the Short- and Long-Term.* Industrial & Engineering Chemistry Research, 2013. **52**(9): p. 3089-3111.
4. Vøllestad, E., et al., *Mixed proton and electron conducting double perovskite anodes for stable and efficient tubular proton ceramic electrolysers.* Nature Materials, 2019. **18**(7): p. 752-759.
5. Shim, J.H., *Ceramics breakthrough.* Nature Energy, 2018. **3**(3): p. 168-169.
6. Fabbri, E., D. Pergolesi, and E. Traversa, *Materials challenges toward proton-conducting oxide fuel cells: a critical review.* Chemical Society Reviews, 2010. **39**(11): p. 4355-4369.
7. Strandbakke, R., et al., *Gd- and Pr-based double perovskite cobaltites as oxygen electrodes for proton ceramic fuel cells and electrolyser cells.* Solid State Ionics, 2015. **278**: p. 120-132.
8. Norby, T., *Defects and Transport in Crystalline Materials*. 2015: University of Oslo. 195.
9. Karen, P., *Nonstoichiometry in oxides and its control.* Journal of Solid State Chemistry, 2006. **179**(10): p. 3167-3183.
10. Megaw, H.D., *Crystal structure of double oxides of the perovskite type.* Proceedings of the Physical Society, 1946. **58**(2): p. 133-152.
11. Kuz'min, A.V., et al., *Total and hole conductivity in the BaZr1 − xYxO3 − α system (x = 0.02−0.20) in oxidizing atmosphere.* Russian Journal of Electrochemistry, 2009. **45**(12): p. 1351-1357.
12. Yamazaki, Y., P. Babilo, and S.M. Haile, *Defect Chemistry of Yttrium-Doped Barium Zirconate: A Thermodynamic Analysis of Water Uptake.* Chemistry of Materials, 2008. **20**(20): p. 6352-6357.
13. Vøllestad, E., et al., *Relating defect chemistry and electronic transport in the double perovskite Ba1−xGd0.8La0.2+xCo2O6−δ (BGLC).* Journal of Materials Chemistry A, 2017. **5**(30): p. 15743-15751.
14. Poetzsch, D., R. Merkle, and J. Maier, *Proton uptake in the H+-SOFC cathode material Ba0.5Sr0.5Fe0.8Zn0.2O3−δ: transition from hydration to hydrogenation with increasing oxygen partial pressure.* Faraday Discussions, 2015. **182**(0): p. 129-143.
15. Poetzsch, D., R. Merkle, and J. Maier, *Stoichiometry Variation in Materials with Three Mobile Carriers—Thermodynamics and Transport Kinetics Exemplified for Protons, Oxygen Vacancies, and Holes.* Advanced Functional Materials, 2015. **25**(10): p. 1542-1557.
16. Oldham, K.B., et al., *Electrochemical science and technology : fundamentals and applications*. 2013, John Wiley & Sons, Ltd., Publication: Chichester, West Sussex, England.

17. Adler, S.B., *Factors Governing Oxygen Reduction in Solid Oxide Fuel Cell Cathodes.* Chemical Reviews, 2004. **104**(10): p. 4791-4844.
18. Poetzsch, D., R. Merkle, and J. Maier, *Oxygen Reduction at Dense Thin-Film Microelectrodes on a Proton-Conducting Electrolyte.* Journal of The Electrochemical Society, 2015. **162**(9): p. F939-F950.
19. Bard, A.J. and L.R. Faulkner, *Electrochemical methods : fundamentals and applications*. 2nd ed. ed. 2001, New York: Wiley.
20. Lvovich, V.F., *Impedance Spectroscopy: Applications to Electrochemical and Dielectric Phenomena*. 2012.
21. Orazem, M.E. and B. Tribollet, *Front Matter*. 2017, Hoboken, NJ, USA: John Wiley & Sons, Inc.: Hoboken, NJ, USA. p. i-xlvii.
22. Murray, E.P., T. Tsai, and S.A. Barnett, *A direct-methane fuel cell with a ceria-based anode.* Nature, 1999. **400**(6745): p. 649-651.
23. Park, S., J.M. Vohs, and R.J. Gorte, *Direct oxidation of hydrocarbons in a solid-oxide fuel cell.* Nature, 2000. **404**(6775): p. 265-267.
24. Lo Faro, M., et al., *Fuel flexibility: A key challenge for SOFC technology.* Fuel, 2012. **102**: p. 554-559.
25. Stambouli, A.B. and E. Traversa, *Solid oxide fuel cells (SOFCs): a review of an environmentally clean and efficient source of energy.* Renewable and Sustainable Energy Reviews, 2002. **6**(5): p. 433-455.
26. Minh, N.Q., *Ceramic Fuel Cells.* Journal of the American Ceramic Society, 1993. **76**(3): p. 563-588.
27. Jacobson, A.J., *Materials for Solid Oxide Fuel Cells.* Chemistry of Materials, 2010. **22**(3): p. 660-674.
28. Chen, D., et al., *Intermediate-temperature electrochemical performance of a polycrystalline PrBaCo2O5+δ cathode on samarium-doped ceria electrolyte.* Journal of Power Sources, 2009. **188**(1): p. 96-105.
29. Norby, T. and Y. Larring, *Concentration and transport of protons in oxides.* Current Opinion in Solid State and Materials Science, 1997. **2**(5): p. 593-599.
30. Kreuer, K.D., *On the development of proton conducting materials for technological applications.* Solid State Ionics, 1997. **97**(1): p. 1-15.
31. Fabbri, E., D. Pergolesi, and E. Traversa, *Electrode materials: a challenge for the exploitation of protonic solid oxide fuel cells.* Science and Technology of Advanced Materials, 2010. **11**(4): p. 044301.
32. Cowin, P.I., et al., *Recent Progress in the Development of Anode Materials for Solid Oxide Fuel Cells.* Advanced Energy Materials, 2011. **1**(3): p. 314-332.
33. Dubois, A., S. Ricote, and R.J. Braun, *Benchmarking the expected stack manufacturing cost of next generation, intermediate-temperature protonic ceramic fuel cells with solid oxide fuel cell technology.* Journal of Power Sources, 2017. **369**: p. 65-77.
34. Matsuzaki, Y., et al., *Effect of proton-conduction in electrolyte on electric efficiency of multi-stage solid oxide fuel cells.* Scientific Reports, 2015. **5**(1): p. 12640.
35. Iwahara, H., et al., *Proton conduction in sintered oxides and its application to steam electrolysis for hydrogen production.* Solid State Ionics, 1981. **3-4**: p. 359-363.
36. Iwahara, H., et al., *Protonic conduction in calcium, strontium and barium zirconates.* Solid State Ionics, 1993. **61**(1): p. 65-69.
37. Bonanos, N., K.S. Knight, and B. Ellis, *Perovskite solid electrolytes: Structure, transport properties and fuel cell applications.* Solid State Ionics, 1995. **79**: p. 161-170.
38. Kreuer, K.D., et al., *Proton conducting alkaline earth zirconates and titanates for high drain electrochemical applications.* Solid State Ionics, 2001. **145**(1): p. 295-306.

39. Iwahara, H., *Technological challenges in the application of proton conducting ceramics.* Solid State Ionics, 1995. **77**: p. 289-298.
40. Iwahara, H., *High temperature proton conducting oxides and their applications to solid electrolyte fuel cells and steam electrolyzer for hydrogen production.* Solid State Ionics, 1988. **28-30**: p. 573-578.
41. Iwahara, H., *Proton Conduction in Sintered Oxides Based on BaCeO[sub 3]*. Journal of The Electrochemical Society, 1988. **135**(2): p. 529.
42. Yamazaki, Y., R. Hernandez-Sanchez, and S.M. Haile, *High Total Proton Conductivity in Large-Grained Yttrium-Doped Barium Zirconate.* Chemistry of Materials, 2009. **21**(13): p. 2755-2762.
43. Pergolesi, D., et al., *High proton conduction in grain-boundary-free yttrium-doped barium zirconate films grown by pulsed laser deposition.* Nature Materials, 2010. **9**(10): p. 846-852.
44. Iwahara, H., *Oxide-ionic and protonic conductors based on perovskite-type oxides and their possible applications.* Solid State Ionics, 1992. **52**(1): p. 99-104.
45. Kreuer, K.D., *Proton-Conducting Oxides.* Annual Review of Materials Research, 2003. **33**(1): p. 333-359.
46. Iwahara, H., T. Yajima, and H. Ushida, *Effect of ionic radii of dopants on mixed ionic conduction (H++O2−) in BaCeO3-based electrolytes.* Solid State Ionics, 1994. **70-71**: p. 267-271.
47. Kreuer, K.D., *Aspects of the formation and mobility of protonic charge carriers and the stability of perovskite-type oxides.* Solid State Ionics, 1999. **125**(1): p. 285-302.
48. Kreuer, K.D., et al., *Defect interactions in proton conducting perovskite-type oxides.* Berichte der Bunsengesellschaft/Physical Chemistry Chemical Physics, 1997. **101**(9): p. 1344-1350.
49. Bhide, S.V. and A.V. Virkar, *Stability of BaCeO3-Based Proton Conductors in Water-Containing Atmospheres.* Journal of The Electrochemical Society, 1999. **146**(6): p. 2038-2044.
50. Zakowsky, N., S. Williamson, and J.T.S. Irvine, *Elaboration of CO2 tolerance limits of BaCe0.9Y0.1O3–δ electrolytes for fuel cells and other applications.* Solid State Ionics, 2005. **176**(39): p. 3019-3026.
51. Babilo, P. and S.M. Haile, *Enhanced Sintering of Yttrium-Doped Barium Zirconate by Addition of ZnO.* Journal of the American Ceramic Society, 2005. **88**(9): p. 2362-2368.
52. Bohn, H.G. and T. Schober, *Electrical Conductivity of the High-Temperature Proton Conductor BaZr0.9Y0.1O2.95.* Journal of the American Ceramic Society, 2000. **83**(4): p. 768-772.
53. Katahira, K., et al., *Protonic conduction in Zr-substituted BaCeO3.* Solid State Ionics, 2000. **138**(1): p. 91-98.
54. Zuo, C., et al., *Effect of Zr-Doping on the Chemical Stability and Hydrogen Permeation of the Ni−BaCe0.8Y0.2O3-α Mixed Protonic−Electronic Conductor.* Chemistry of Materials, 2006. **18**(19): p. 4647-4650.
55. Dubal, S.U., et al., *Proton conducting BaCe0.7Zr0.1Y0.2O2.9 thin films by spray deposition for solid oxide fuel cell.* Applied Surface Science, 2015. **324**: p. 871-876.
56. Yoo, Y. and N. Lim, *Performance and stability of proton conducting solid oxide fuel cells based on yttrium-doped barium cerate-zirconate thin-film electrolyte.* Journal of Power Sources, 2013. **229**: p. 48-57.
57. Fabbri, E., et al., *Tailoring the chemical stability of Ba(Ce0.8−xZrx)Y0.2O3−δ protonic conductors for Intermediate Temperature Solid Oxide Fuel Cells (IT-SOFCs).* Solid State Ionics, 2008. **179**(15): p. 558-564.

58. Uchida, H., S. Tanaka, and H. Iwahara, *Polarization at Pt electrodes of a fuel cell with a high temperature-type proton conductive solid electrolyte.* Journal of Applied Electrochemistry, 1985. **15**(1): p. 93-97.
59. Iwahara, H., *Performance of Solid Oxide Fuel Cell Using Proton and Oxide Ion Mixed Conductors Based on BaCe[sub 1−x]Sm[sub x]O[sub 3−α].* Journal of The Electrochemical Society, 1993. **140**(6): p. 1687.
60. Tao, S.W., et al., *Electrode materials for intermediate temperature proton-conducting fuel cells.* Journal of Applied Electrochemistry, 2000. **30**(2): p. 153-157.
61. Kim, J., et al., *Triple-Conducting Layered Perovskites as Cathode Materials for Proton-Conducting Solid Oxide Fuel Cells.* ChemSusChem, 2014. **7**(10): p. 2811-2815.
62. Duan, C., et al., *Zr and Y co-doped perovskite as a stable, high performance cathode for solid oxide fuel cells operating below 500 °C.* Energy & Environmental Science, 2017. **10**(1): p. 176-182.
63. Duan, C., et al., *Readily processed protonic ceramic fuel cells with high performance at low temperatures.* Science, 2015. **349**(6254): p. 1321.
64. Téllez Lozano, H., et al., *Double perovskite cathodes for proton-conducting ceramic fuel cells: are they triple mixed ionic electronic conductors?* Science and Technology of Advanced Materials, 2017. **18**(1): p. 977-986.
65. Lin, Y., et al., *Performance of PrBaCo2O5+δ as a Proton-Conducting Solid-Oxide Fuel Cell Cathode.* The Journal of Physical Chemistry A, 2010. **114**(11): p. 3764-3772.
66. Zhang, K., et al., *Synthesis, characterization and evaluation of cation-ordered LnBaCo2O5+δ as materials of oxygen permeation membranes and cathodes of SOFCs.* Acta Materialia, 2008. **56**(17): p. 4876-4889.
67. Tarancón, A., et al., *GdBaCo2O5+x layered perovskite as an intermediate temperature solid oxide fuel cell cathode.* Journal of Power Sources, 2007. **174**(1): p. 255-263.
68. Zhu, C., et al., *Electrochemical performance of PrBaCo2O5+δ layered perovskite as an intermediate-temperature solid oxide fuel cell cathode.* Journal of Power Sources, 2008. **185**(1): p. 193-196.
69. Zohourian, R., et al., *Mixed-Conducting Perovskites as Cathode Materials for Protonic Ceramic Fuel Cells: Understanding the Trends in Proton Uptake.* Advanced Functional Materials, 2018. **28**(35): p. 1801241.
70. Strandbakke, R., et al., *Ba0.5Gd0.8La0.7Co2O6-δInfiltrated in Porous BaZr0.7Ce0.2Y0.1O3Backbones as Electrode Material for Proton Ceramic Electrolytes.* Journal of The Electrochemical Society, 2017. **164**(4): p. F196-F202.
71. Pedersen, M.K., *Fundamentals of Positrodes for Proton Ceramic Electrochemical Cells*. 2019.
72. *ProboStat, overview*. [cited 2020 02.06]; Available from: www.norecs.com/index.php?page=Overview.
73. NORBY, T. and P. KOFSTAD, *Electrical Conductivity and Defect Structure of Y2O3 as a Function of Water Vapor Pressure.* Journal of the American Ceramic Society, 1984. **67**(12): p. 786-792.
74. Winkler, J., *Geometric Requirements of Solid Electrolyte Cells with a Reference Electrode.* Journal of The Electrochemical Society, 1998. **145**(4): p. 1184.
75. Schubert, U. and N. Hüsing, *Synthesis of inorganic materials*. 3rd compl. rev. and enl. ed. 2012, Weinheim: Wiley.
76. Kochetova, N., et al., *Recent activity in the development of proton-conducting oxides for high-temperature applications.* RSC Advances, 2016. **6**(77): p. 73222-73268.
77. Bae, K., et al., *High-Performance Protonic Ceramic Fuel Cells with 1 μm Thick Y:Ba(Ce, Zr)O3 Electrolytes.* Advanced Energy Materials, 2018. **8**(25): p. 1801315.

78. An, H., et al., *A 5 × 5 cm2 protonic ceramic fuel cell with a power density of 1.3 W cm–2 at 600 °C.* Nature Energy, 2018. **3**(10): p. 870-875.
79. Andersen, H., et al., *A highly efficient electrocatalyst based on double perovskite cobaltites with immense intrinsic catalytic activity for water oxidation.* Chemical Communications, 2020. **56**(7): p. 1030-1033.

Appendix

A.1-Proton Uptake

Calculation of mol % H^+ for BGLC82: Ti at 300 ℃ can be calculated from the mass change at D_2O shift. The amount of deuterium in the change is double than the observed change due to deuterium is double the weight of protons.

The amount of mol of deuterium becomes:

$$n_{\mathrm{D}} = \frac{2(m_{\mathrm{D}}/1000)}{M_{\mathrm{D}}} = \frac{2(0.043\ \mathrm{mg}/1000)}{2.016\ \mathrm{g/mol}} = 4.3 \cdot 10^{-5}\ \mathrm{mol} \tag{A.1.1}$$

The mol % of H^+ is then given by:

$$\text{mol \% } \mathrm{H^+} = \frac{n_D}{n_{\mathrm{D}} + n_{BGLC82:Ti}} \cdot 100 = \frac{4.5 \cdot 10^{-5}\ \mathrm{mol}}{4.5 \cdot 10^{-5}\ \mathrm{mol} + 0.048\ \mathrm{mol}} \cdot 100 = 0.89 \tag{A.1.2}$$

For the ratio of hydration and hydrogenation, the mass difference between the obtained mass at H_2O atmosphere and the obtained mass at D_2O atmosphere is the mass of oxygen. The amount of oxygen is assumed to come from hydration. The mol of protons from hydration is then two times the mol of oxygen. The mol of protons from hydration becomes:

$$n_{\mathrm{H}} = 2 \cdot n_{\mathrm{O}} = 2 \cdot \frac{\left(\frac{m_{\mathrm{H_2O}} - m_{\mathrm{D}}}{1000}\right)}{M_{\mathrm{O}}} = 2 \cdot \frac{\left(\frac{0.063\ \mathrm{mg} - 0.043\ \mathrm{mg}}{1000}\right)}{16\ \mathrm{g/mol}} = 2.5 \cdot 10^{-6}\ \mathrm{mol} \tag{A.1.3}$$

The ratio between hydration and hydrogenation becomes:

$$\%\ \text{hydration} = \frac{n_{\mathrm{H}}}{n_{\mathrm{D}}} \cdot 100 = \frac{2.5 \cdot 10^{-6}\ \mathrm{mol}}{4.3 \cdot 10^{-5}\ \mathrm{mol}} \cdot 100 = 6\ \% \tag{A.1.4}$$

$$\%\ \text{hydrogenation} = \frac{n_{\mathrm{D}} - n_{\mathrm{H}}}{n_{\mathrm{D}}} \cdot 100 = \frac{(4.3 \cdot 10^{-5}\ -\ 2.5 \cdot 10^{-6}\ )\ \mathrm{mol}}{4.3 \cdot 10^{-5}\ \mathrm{mol}} \cdot 100 = 94\ \% \tag{A.1.5}$$

A.2 – OCV measurements

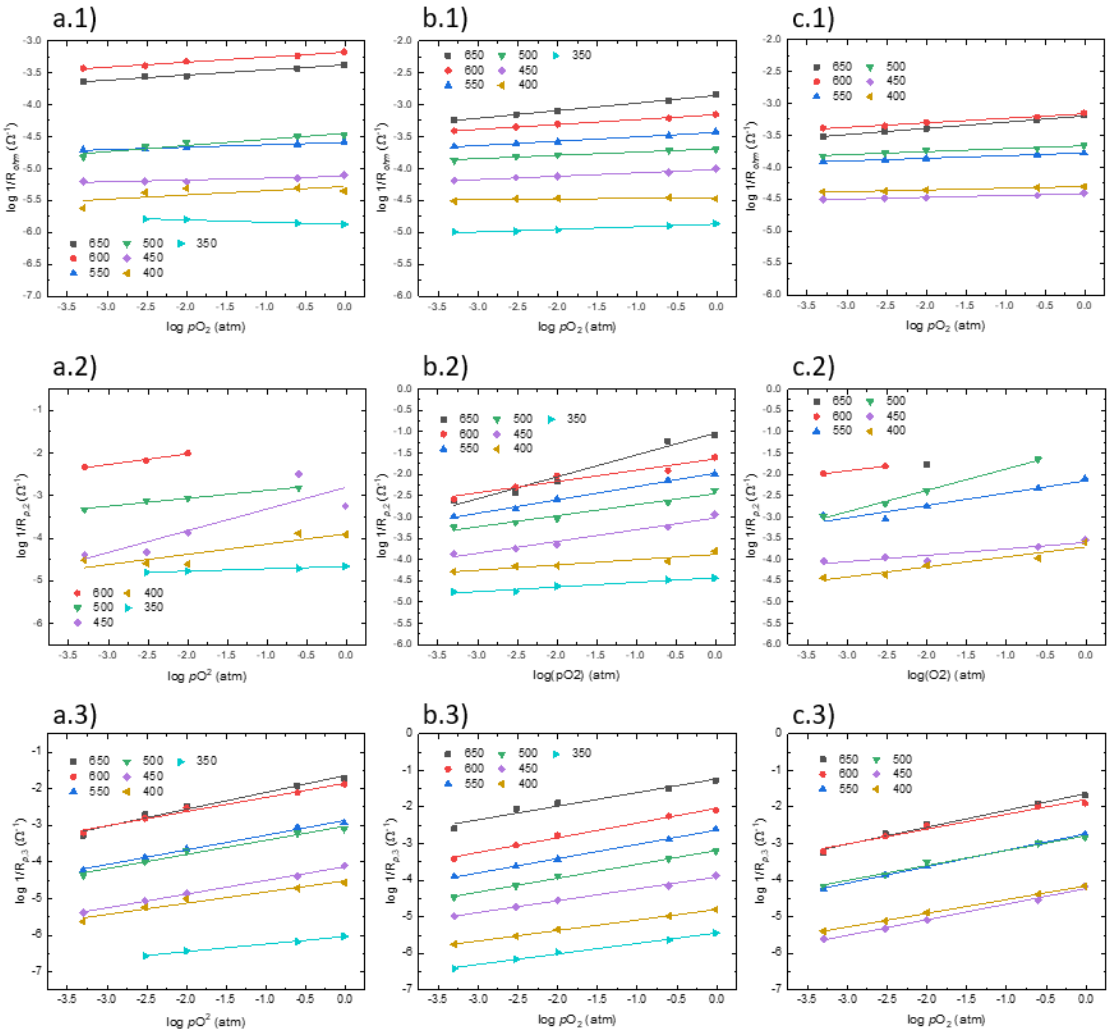

Figure A.2.1 pO_2 dependencies for a) BGLC82: Ti, b) BGLC82: Zr SSR and c) BGLC82: Zr SG, where the number represents the different contributions, 1) ohmic, 2) $R_{p,2}$ and 3) $R_{p,3}$. All measurements were carried out with pH_2O = 0.025 atm.

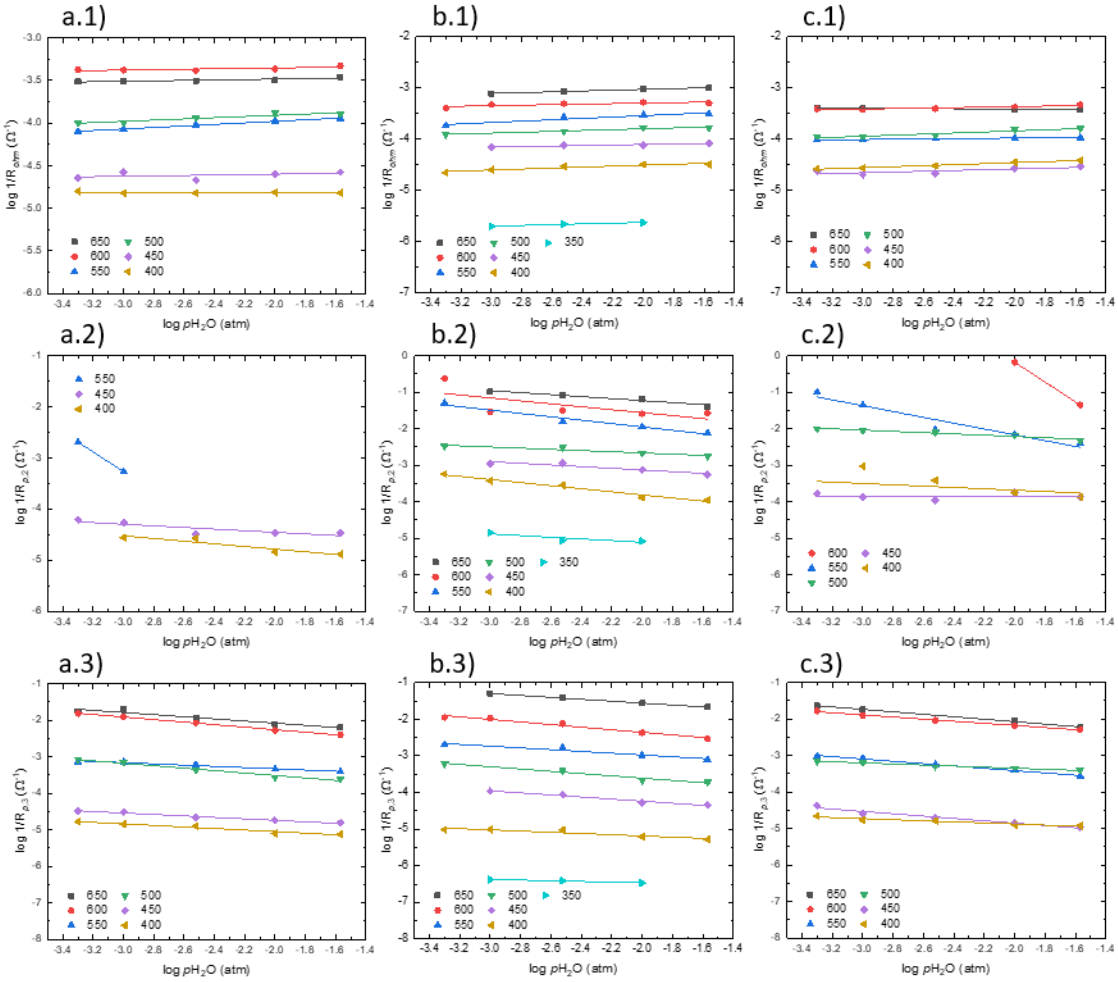

Figure A.2.2 pH_2O dependencies for a) BGLC82: Ti, b) BGLC82: Zr SSR and c) BGLC82: Zr SG, where the number represents the different contributions, 1) ohmic, 2) $R_{p,2}$ and 3) $R_{p,3}$. All measurements were carried out with pH_2O = 0.025 atm.

A.3 – Negativ Bias Measurements

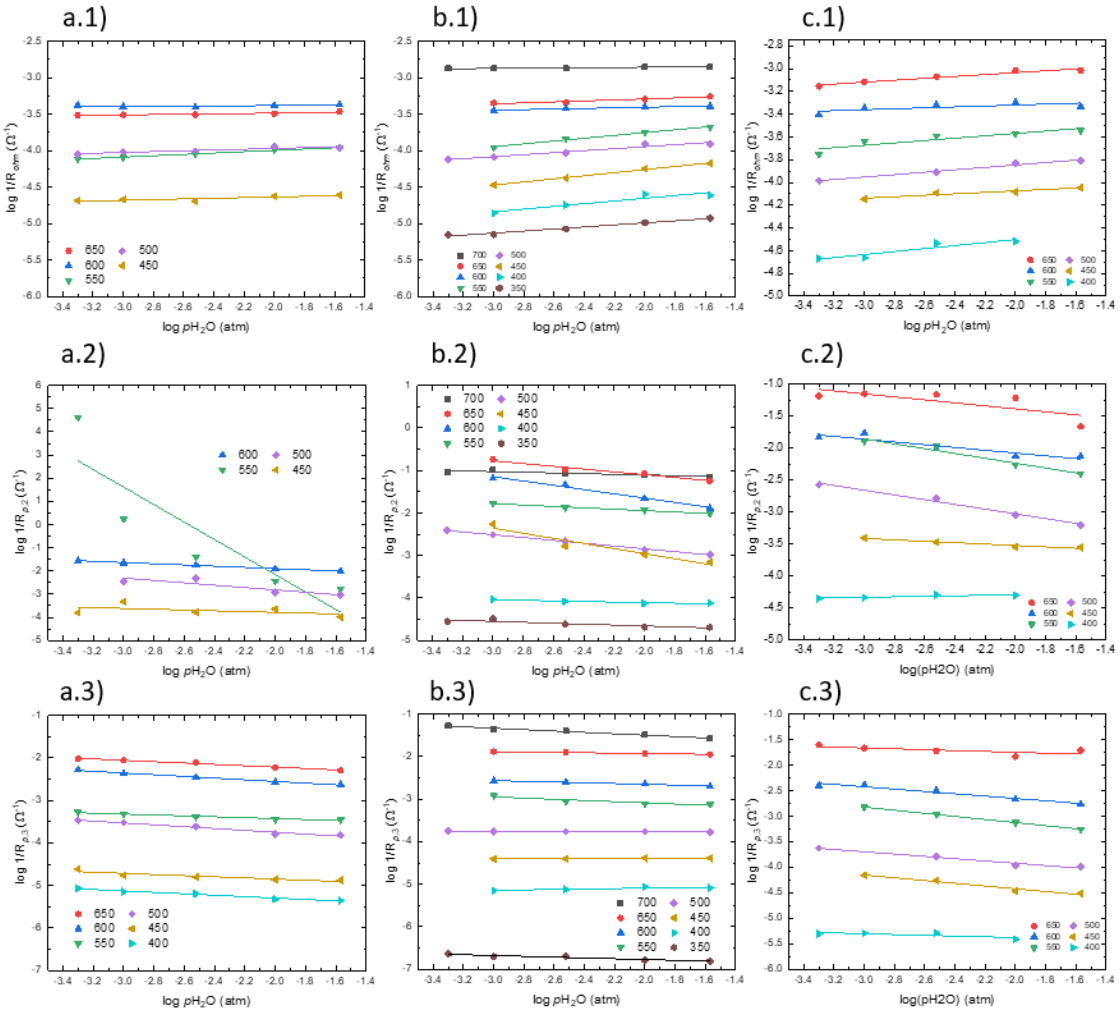

Figure A.3.1 pH_2O dependencies for a) BGLC82: Ti, b) BGLC82: Zn and c) BGLC82: Zr SSR, where the number represents the different contributions, 1) ohmic, 2) $R_{p,2}$ and 3) $R_{p,3}$. All measurements were carried out with pO_2 = 0.20 atm with a negative bias of 100 mV.

Table A.3.1 The ohmic and polarisation resistances for the different electrodes on a BZCY72 electrolyte at high, intermediate and low temperatures. The measurements were carried out in pO_2 = 0.20 atm, pH_2O = 0.025 atm and negative bias of 100 mV.

	T (°C)	R_{ohm} (kΩcm^2)	$R_{p,2}$ (kΩcm^2)	$R_{p,3}$ (kΩcm^2)
	650	0.57	--	0.039
BGLC82: Ti	500	1.8	0.21	1.3
	400	14	6.3	44
	650	0.35	0.0035	0.017
BGLC82: Zn	500	1.6	0.19	1.2
	400	8.1	2.6	24
	650	0.20	0.090	0.010
BGLC82: Zr SSR	500	1.3	0.31	1.9
	350	15	7.6	26

Table A.3.2 Capacitance values for the ohmic (C_{ohm}) and polarization resistances ($C_{p,2}$ and $C_{p,3}$), at high, intermediate and low temperatures. The measurements were carried out in pO_2 = 0.20 atm, pH_2O = 0.025 atm and a negative bias of 100 mV.

	T (°C)	C_{ohm} (Fcm^{-2})	$C_{p,2}$ (Fcm^{-2})	$C_{p,3}$ (Fcm^{-2})
	650	$1.5 \cdot 10^{-9}$	--	$6.1 \cdot 10^{-6}$
BGLC82: Ti	500	$1.2 \cdot 10^{-9}$	$1.7 \cdot 10^{-7}$	$1.6 \cdot 10^{-6}$
	400	$1.7 \cdot 10^{-9}$	$5.6 \cdot 10^{-8}$	$7.3 \cdot 10^{-7}$
	650	$1.4 \cdot 10^{-9}$	$2.1 \cdot 10^{-6}$	$7.9 \cdot 10^{-5}$
BGLC82: Zn	500	$1.7 \cdot 10^{-9}$	$1.9 \cdot 10^{-6}$	$1.6 \cdot 10^{-4}$
	400	$1.6 \cdot 10^{-9}$	$3.9 \cdot 10^{-6}$	$5.2 \cdot 10^{-4}$
	650	$1.4 \cdot 10^{-9}$	$4.6 \cdot 10^{-6}$	$2.1 \cdot 10^{-5}$
BGLC82: Zr SSR	500	$1.2 \cdot 10^{-9}$	$8.6 \cdot 10^{-8}$	$1.3 \cdot 10^{-6}$
	350	$1.6 \cdot 10^{-9}$	$2.5 \cdot 10^{-7}$	$2.7 \cdot 10^{-6}$

Table A.3.3 Activation energies and pre-exponentials from negative bias measurements for the three contributions and each electrode, with pO_2 = 0.20 atm, pH_2O = 0.025 atm and a negative bias of 100 mV.

	Contribution	T (°C)	E_a (eV)	Pre-exponential factor ($\Omega^{-1}cm^{-2}$)
BGLC82: Ti	Ohmic	650 – 350	$0.8 \pm 0.1_0$	$1.5 \cdot 10^4$
	$R_{p,2}$	600 – 350	$1.4 \pm 0.1_2$	$1.6 \cdot 10^6$
	$R_{p,3}$	650 – 350	$1.5 \pm 0.1_0$	$2.3 \cdot 10^6$
BGLC82: Zn	Ohmic	650 – 350	$0.74 \pm 0.03_4$	$7.6 \cdot 10^3$
	$R_{p,2}$	600 – 350	$1.27 \pm 0.06_6$	$3.7 \cdot 10^5$
	$R_{p,3}$	650 – 350	$1.53 \pm 0.03_6$	$2.0 \cdot 10^6$
BGLC82: Zr SSR	Ohmic	650 – 350	$0.74 \pm 0.02_2$	$9.3 \cdot 10^3$
	$R_{p,2}$	600 – 350	$1.37 \pm 0.06_0$	$7.2 \cdot 10^5$
	$R_{p,3}$	650 – 350	$1.84 \pm 0.09_9$	$1.3 \cdot 10^8$

A.4 – Positiv Bias Measurements

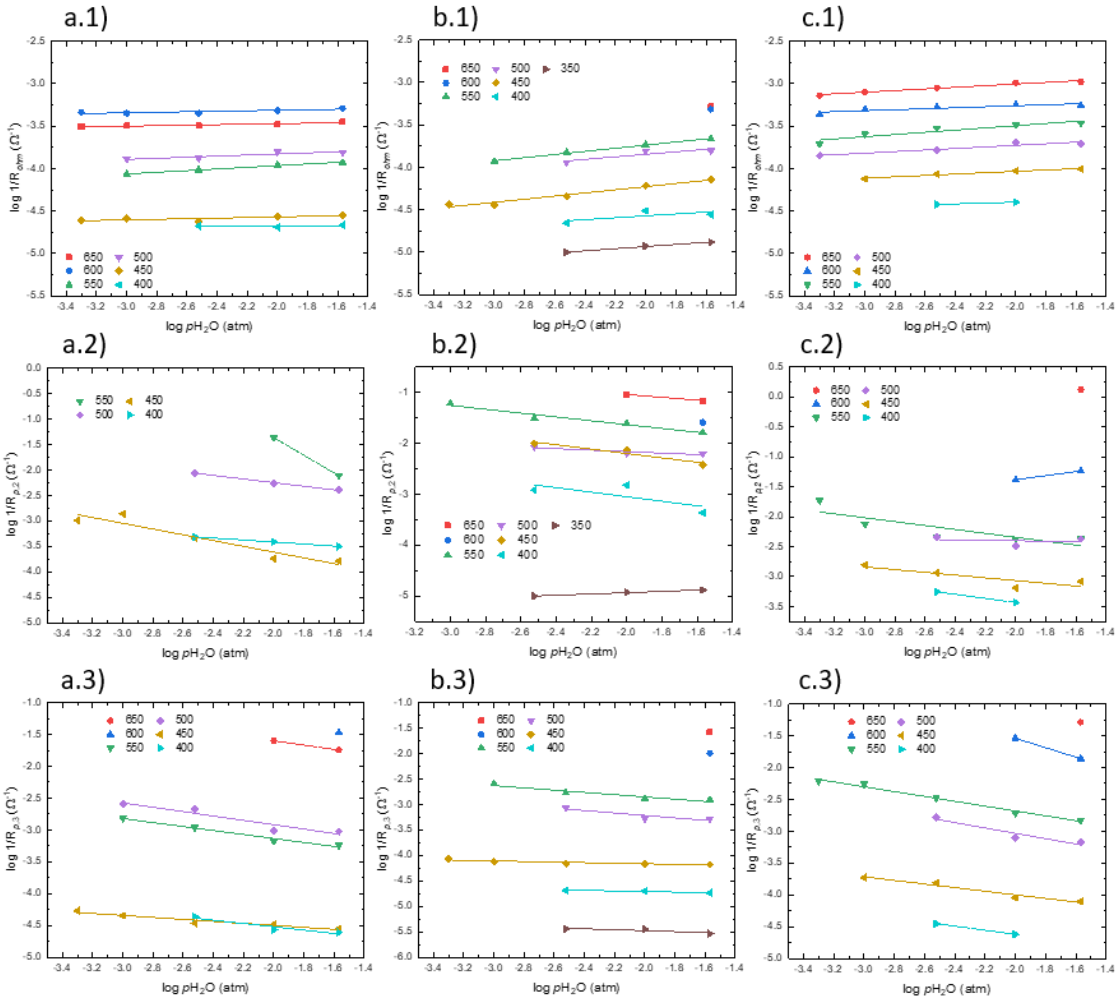

Figure A.4.1 pH_2O dependencies for a) BGLC82: Ti, b) BGLC82: Zn and c) BGLC82: Zr SSR, where the number represents the different contributions, 1) ohmic, 2) $R_{p,2}$ and 3) $R_{p,3}$. All measurements were carried out with pO_2 = 0.20 atm with a positive bias of 50-100 mV.

Table A.4.1 The ohmic and polarisation resistances for the different electrodes on a BZCY72 electrolyte at high, intermediate and low temperatures. The measurements were carried out in pO_2 = 0.20 atm, pH_2O = 0.025 atm and a positive bias of 50-100 mV.

	T (°C)	R_{ohm} (kΩcm^2)	$R_{p,2}$ (kΩcm^2)	$R_{p,3}$ (kΩcm^2)
	650	0.55	--	0.011
BGLC82: Ti	500	1.3	0.049	0.21
	400	9.1	0.62	7.9

	650	0.35	0.0029	0.0079
BGLC82: Zn	500	1.3	0.032	0.038
	400	7.1	0.46	11
	650	0.019	0.00015	0.0038
BGLC82: Zr SSR	500	1.0	0.046	0.29
	450	2.0	0.24	2.5

Table A.4.2 Capacitance values for the ohmic (C_{ohm}) and polarization resistances ($C_{p,2}$ and $C_{p,3}$), at high, intermediate and low temperatures. The measurements were carried out in pO_2 = 0.20 atm, pH_2O = 0.025 atm and a positive bias of 50-100 mV.

	T (°C)	C_{ohm} (Fcm^{-2})	$C_{p,2}$ (Fcm^{-2})	$C_{p,3}$ (Fcm^{-2})
	650	$1.5 \cdot 10^{-9}$	--	$2.4 \cdot 10^{-5}$
BGLC82: Ti	500	$1.2 \cdot 10^{-9}$	$7.6 \cdot 10^{-7}$	$1.6 \cdot 10^{-5}$
	400	$1.4 \cdot 10^{-9}$	$3.5 \cdot 10^{-7}$	$7.7 \cdot 10^{-6}$
	650	$1.4 \cdot 10^{-9}$	$3.8 \cdot 10^{-6}$	$4.2 \cdot 10^{-5}$
BGLC82: Zn	500	$1.7 \cdot 10^{-9}$	$9.4 \cdot 10^{-7}$	$1.9 \cdot 10^{-5}$
	400	$1.8 \cdot 10^{-9}$	$5.8 \cdot 10^{-7}$	$1.2 \cdot 10^{-5}$
	650	$1.5 \cdot 10^{-9}$	$7.9 \cdot 10^{-7}$	$2.1 \cdot 10^{-4}$
BGLC82: Zr SSR	500	$1.2 \cdot 10^{-9}$	$4.2 \cdot 10^{-7}$	$1.3 \cdot 10^{-5}$
	450	$1.6 \cdot 10^{-9}$	$9.7 \cdot 10^{-8}$	$8.5 \cdot 10^{-6}$

Table A.4.3 Activation energies and pre-exponential from positive bias measurement for the three contributions and each electrode, with pO_2 = 0.20 atm, pH_2O = 0.025 atm with a positive bias of 50-100 mV.

	Contribution	T (°C)	E_a (eV)	Pre-exponential factor ($\Omega^{-1}cm^{-2}$)
BGLC82: Ti	Ohmic	650 – 350	$0.7 \pm 0.1_2$	$6.4 \cdot 10^3$
	$R_{p,2}$	600 – 350	$1.1 \pm 0.5_0$	$1.5 \cdot 10^5$
	$R_{p,3}$	650 – 350	$1.6 \pm 0.3_1$	$2.4 \cdot 10^7$
BGLC82: Zn	Ohmic	650 – 350	$0.70 \pm 0.02_9$	$4.1 \cdot 10^5$
	$R_{p,2}$	600 – 350	$0.8 \pm 0.1_0$	$3.5 \cdot 10^5$
	$R_{p,3}$	650 – 350	$1.51 \pm 0.07_4$	$4.0 \cdot 10^5$
BGLC82: Zr SSR	Ohmic	650 – 350	$0.73 \pm 0.02_6$	$9.0 \cdot 10^3$
	$R_{p,2}$	600 – 350	$1.9 \pm 0.4_4$	$1.8 \cdot 10^{10}$
	$R_{p,3}$	650 – 350	$1.8 \pm 0.1_4$	$4.7 \cdot 10^8$